

Structural Features of Air-Processible Methyl Ammonium Lead Triiodide (MAPbI₃) Perovskite Thin Films Grown on Al-doped ZnO Nanowire Arrays

by

Mpho Phakoe

A thesis submitted in fulfilment of the requirements for the degree of Magister Scientiae in the Department of Physics, University of the Western Cape

Supervisor: Prof FR Cummings, University of the Western Cape (UWC)

November 2023

ACKNOWLEDGMENTS

I am extremely grateful to the following people and organisations for the assistance, guidance and support given. Without whom, this thesis would not have been completed.

The National Research Foundation (NRF) and University of the Western Cape for the financial support during this study.

First and foremost, I would like to thank my Supervisor Prof Franscious Cummings, for his invaluable guidance, unwavering support, and insightful feedback throughout the research process. Without his patience and dedication this thesis would not have been possible.

I would also like to extend my sincere gratitude to the faculty and staff of University of the Western Cape Physics Department, whose expertise and knowledge have been instrumental in shaping my academic and research pursuits.

My thanks also go to my dad, Charles Mohlomi, my siblings Neo Mohlomi, Thato Mohlomi, my life partner Themba Msiza and my friends (Nthabiseng Makae, Portia Radebe, Sumeera Gopal and Nonhlanhla Baloyi) who provided me with constant love, encouragement, motivation, and support. Their unwavering belief in me and my abilities has been a driving force behind my success.

Finally, I would like to thank GOD, Guardian Angels, my Ancestors, my late mother (Maria Hadio Phakoe) and late grandparents for guidance and protection. My mom would have been so proud!!

Once again, I would like to thank everyone who has contributed to the successful completion of my master's thesis. Your help and support have been invaluable, and I am deeply grateful.

DECLARATION

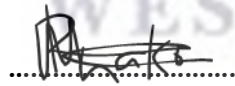
I declare that

“Structural Features of Air-Processible Methyl Ammonium Lead Triiodide (MAPbI₃) Perovskite Thin Films Grown on Al-doped ZnO Nanowire Arrays” is my own work, has not been submitted for any degree or examination in another university, and that all sources I have used or quoted have been indicated and acknowledged by means of complete references

Mpho Phakoe

November 2023

Signature:



KEYWORDS

*Structural Features of Air-Processible Methyl Ammonium Lead Triiodide (MAPbI₃) Perovskite
Thin Films Grown on Al-doped ZnO Nanowire Arrays*

Fossil Fuel

Crude Oil

Renewable Energy

Photovoltaics

Nanotechnology

One-dimensional Nanostructures

Zinc Oxide

Perovskites

Halides

Methylammonium Lead Tri-iodide

Hydrothermal Synthesis

Spin-coating

Electron Microscopy

X-ray Diffraction

X-ray Photoelectron Spectroscopy

UV-Vis Spectroscopy

Crystallinity



ABSTRACT

Structural Features of Air-Processible Methyl Ammonium Lead Triiodide (MAPbI₃) Perovskite

Thin Films Grown on Al-doped ZnO Nanowire Arrays

The performance of air stable, mixed halide (MAPbI_{3-x}Cl_x) perovskite based solar cells is highly dependent on the quality and stability of the perovskite thin film, which in turn, is dependent on the substrate on which it is deposited. ZnO presents excellent optoelectronic properties such as high electron mobility and diffusion length, direct band gap with high exciton binding energy. An array of ZnO nanowires (NWs) grown vertically on a conducting substrate, benefits from a large surface area, direct electron transport pathway and reduced recombination rate of carriers when used in a solar cell. These arrays of ZnO NWs may be synthesised by a wide range of methods, with the chemical bath deposition (CBD) method considered to be the most simple and cost-effective.

In this study, the CBD method was employed to investigate the growth of ZnO NWs on an aluminium doped ZnO substrate. The structural and optical properties of the nanowires were studied using electron microscopy, energy dispersive x-ray spectroscopy, X-ray diffraction and UV-Vis spectroscopy. An optimised NW morphology was achieved by non-pressured chemical bath method using an aqueous solution comprising of 70 mM concentration of zinc acetate, hexamethylenetetramine and polyethylenimine, synthesised at 90 °C for 3hrs. The resultant nanowires showed light transmission above 80% in the visible to IR region, which is beneficial for photovoltaic application. The optimisation of the MAPbI_{3-x}Cl perovskite layers was also investigated to study the morphology and surface coverage of the ink on nanowires. The best perovskites coverage and morphology were observed at a temperature of 120 °C, an annealing time of 3hrs using a dynamic, one-step spin coating at 2000 rpm for 60s. These results are promising for solar cell application, as it allows for fast deposition and conversion of perovskite layers on a ZnO NW array; which has not been reported in literature to date.

TABLE OF FIGURES

Fig. 1. 1:	Pie-chart showing the South African energy mix in 2019 [1.1]	2
Fig. 1. 2:	Eskom power generation and distribution network [1.1]	3
Fig. 1. 3:	Schematic of the photovoltaic effect [1.7]	5
Fig. 1. 4:	Direct and indirect band gaps [1.10].....	6
Fig. 1. 5:	First generation solar cell [1.11]	7
Fig. 1. 6:	Basic structure of a CIGS solar cell [1.12]	8
Fig. 1. 7:	Basic structure of a CdTe solar cell [1.12].....	9
Fig. 1. 8:	Diagram that shows the mechanism of an organic solar cell [1.17].....	10
Fig. 1. 9:	(a) Perovskite crystal structure, (b) BX_6 octa-hydra, (c) cubic, tetragonal and orthorhombic phases of $MAPbI_3$ perovskite [1.21]	13
Fig. 1. 10:	(a) Cross-sectional view of of ZnO-based perovskite solar cells; (b) schematic of the solar cell design [1.24]	15
Fig. 1. 11:	Degradation of $MAPbI_3$ thin films, demonstrated by a change in colour from dark brown to yellow, with progressive decrease in the halide concentration [1.39].....	17
Fig. 1. 12:	Synthesis strategies followed during one-step and two-step spin-coating to form $MAPbI_{3-x}Cl_x$ mixed halide perovskite thin films on a substrate [1.46].....	20
Fig. 1. 13:	Scanning electron microscope images of (a) $MAPbI_3$ ($Cl = 0$); (b) $MAPbI_{3-x}Cl_x$ and (c) $MAPbCl_3$ ($I = 0$) deposited on a TiO_2/FTO substrate [1.40].....	21
Fig. 1. 14:	SEM images of (a) $CH_3NH_3PbI_3$ and (b) $CH_3NH_3PbI_{3-x}Cl_x$ [1.47].....	21
Fig. 1. 15:	Scanning electron microscope images of $MAPbI_{3-x}Cl_x$ thin films grown on compact TiO_2 layer containing (a) no TiO_2 , (b) 3 nm TiO_2 , (c) 16 nm and (d) 23 nm mesoporous TiO_2 nanoparticles [1.48]	22
Fig. 1. 16:	SEM micrographs of $MAPbI_{3-x}Cl_x$ thin films on ZnO nanoparticles with diameters of (a) 70 nm, (b) 50 nm and (c) 20 nm Scale bar: 10 μm [1.49]	23
Fig. 2.1:	A schematic showing the three ZnO crystals, adopted from [2.1]	34

Fig. 2.2:	Wurtzite unit cell [2.1]	35
Fig. 2.3:	(a) PTFE-lined autoclave and (b) PPL-lined autoclave reactor [https://shilpent.com]	37
Fig. 2.4:	Growth of ZnO nanorod/wires during hydrothermal synthesis [2.8].....	40
Fig. 2.5:	(a) Glass cutter (b) substrate rack and Hellmanex III solution used for sample cleaning	43
Fig. 2.6:	Schematic of the methodology followed during ZnO NW synthesis using the autoclave	44
Fig. 2.7:	Schematic of the methodology followed during ZnO NW synthesis using the autoclave	45
Fig. 3.1:	Schematic illustration of a typical spin-coating apparatus [3.1]	52
Fig. 3.2:	One-step spin-coating process for perovskite thin film deposition [3.5]	53
Fig. 3.3:	SEM micrographs demonstrating the formation of pin-holes (outlined in yellow) during one-step spin-coating [3.7].....	54
Fig. 3.4:	(Top) Lar Mer model for nucleation and growth, (Bottom) Nucleation and growth of the perovskite film at each stage [3.7]	56
Fig. 3.5:	(a) Low-magnification and (b) high-magnification SEM micrograph of MAPbI ₃ film spin-coated onto a 70 nm thin layer of ZnO [3.12].....	57
Fig. 3.6:	SEM micrographs of the MAPbI ₃ films grown on (a) 25, (b) 40 and (c) 50 nm ZnO nanoparticle films [3.13]	58
Fig. 3.7:	SEM micrographs of MAPbI _{3-x} Cl _x thin films on ZnO nanoparticles with diameters of (a) 70 nm, (b) 50 nm and (c) 20 nm Scale bar: 10 μm [3.14]	59
Fig. 3.8:	SEM micrographs of (a) ZnO nanowire array and (b) MAPbI ₃ thin films grown on ZnO nanowire array via sequential spin-coating [3.16]	60
Fig. 3.9:	SEM micrographs of MAPbI _{3-x} Cl _x on various lengths of ZnO NWs [3.15]	61
Fig. 3.10:	Schematic representation of: (a) (left) MAPbI ₃ and (right) MAPbI _{3-x} Cl _x thin films during operation in a solar cell; (b) three major issues facing MAPbI _{3-x} Cl _x thin films, namely	

ion radius mismatch, phase segregation and sublimation issues during annealing [3.18]	63
Fig. 3.11: Chloride–iodide perovskite film formation and morphology: (a) nucleation during deposition, (b) phase evolution and (c) growth during annealing; (d - f) SEM micrographs of the three major morphological constituents (scale bars = 2 μm) [3.24]	65
Fig. 3.12: Ossila I101 perovskite [https://www.ossila.com/products/perovskite-ink-air].....	67
Fig. 3.13: Ossila spin coater used during this study for the deposition of $\text{MAPb}_{1-x}\text{Cl}_x$ thin films.	68
Fig. 4. 1: A schematic diagram showing the main components of a scanning electron microscope [4.1]	78
Fig. 4.2: (a) Zeiss Auriga FE-SEM, (b) Evactron 25 Plasma Cleaner	80
Fig. 4.3: Schematic diagram showing the main components of a TEM [4.3]	81
Fig. 4.4: Geometry of electron diffraction [4.1]	82
Fig. 4.5: Schematic representation of different electron diffraction patterns: (a) spot pattern from a perfect, single-crystalline material; (b) scattered spot pattern from a small number of crystalline grains and (c) a ring pattern emerging from a large number of randomly orientated grains [4.1]	83
Fig. 4.6: FEI Tecnai G ² 20 FE-TEM (EMU, UWC).....	86
Fig. 4.7: The 14 Bravais Lattices [4.9]	88
Fig. 4.8: Directions [100], [110] and [111] with a unit cell [4.10].....	89
Fig. 4.9: A schematic diagram of a powder diffractometer [4.10]	91
Fig. 4.10: Schematic representation of X-ray diffraction by a set of parallel planes and the derivation of Bragg’s Law [4.10]	92
Fig. 4.11: PANalytical Empyrean diffractometer used in this work (NMISA, Pretoria)	93
Fig. 4.12: A schematic showing the visible spectrum (390 – 780 nm) represented by only a small portion of the whole electromagnetic spectrum [4.11]	94
Fig. 4.13: Schematic showing the main components of UV-Vis spectrophotometer [4.13].....	96

Fig. 4.14:	Semiconsoft MProbe®20 spectrometer, hosted in the Department of Physics and Astronomy, UWC.....	98
Fig. 4.15:	Schematic representation of XPS instrumentation [4.15].....	99
Fig. 4.16:	Schematic representation of Auger process [4.17]	102
Fig. 5.1:	(a) Top-view and (b) Side-view SEM micrographs of the as-bought AZO substrate; (c) histogram showing the diameter distribution of the AZO crystal grains	107
Fig. 5.2:	(a) EDS data and (b) UV-Vis transmission spectra of the commercial AZO substrate... ..	108
Fig. 5.3:	XRD pattern of commercial AZO substrate.....	110
Fig. 5.4:	SEM micrographs of (a) NW-AC 1h, (b) NW-AC 3h and (c) NW-AC 8h	111
Fig. 5.5:	SEM micrographs of (a) NW-AC 90, (b) NW-AC 100 and (c) NW-AC 110	112
Fig. 5.6:	SEM micrographs of (a) NW-AC 25M, (b) NW-AC 50M and (c) NW-AC 70M	113
Fig. 5.7:	SEM micrographs of (a) NW-CB 1h, (b) NW-CB 2h and (c) NW-CB 3h	114
Fig. 5.8:	SEM micrographs of (a) NW-CB 90, (b) NW-CB 100 and (c) NW-CB 110.....	115
Fig. 5.9:	SEM micrographs of (a) NW-CB 1-25, (b) NW-CB 2-50 and (c) NW-CB 3-70.....	116
Fig. 5.10:	(a) XPS survey scan, (b) high resolution scan of (b) Zn 2p and (c) O 1s line profiles, and (c) summary of the chemical identification and quantification	117
Fig. 5.11:	(b) Bright-field and (b) high-resolution micrographs of a single NW; (c) corresponding SAED pattern; (d) STEM spectral image, with extracted EDS maps of (e) Zn, (f) O and (g) Al	118
Fig. 5.12:	UV-Vis transmission spectra comparison between AZO substrate and AZO/ZnO NWs layer.....	119
Fig. 5.13:	<i>Top Row:</i> SEM micrographs showing the effect of spin-rate; <i>Bottom Row:</i> effect of spin-coating time on MAPb _{3-x} Cl _x thin film formation on a ZnO NW layer	120
Fig. 5.14:	Effect of annealing temperature and time on MAPb _{3-x} Cl _x conversion on NW array substrate	121
Fig. 5.15:	EDS analyses of the Pb:Cl:I ratios for a perovskite layer deposited and converted at the optimised spin-coating and annealing conditions.....	123

Fig. 5.16: MAPbI_{3-x}Cl_x thin film morphology after conversion on substrates with different NW morphology 124

Fig. 5.17: Unit cells of (a) cubic and (b) tetragonal MAPbI₃ [5.20] 124

Fig. 5.18: XRD pattern of cubic (red) and tetragonal (blue) MAPbI₃ [5.21] 125

Fig. 5.19: XRD patterns ZnO NWs and MAPbI_{3-x}Cl_x thin films deposited on a ZnO NW array grown for 1hr and 3 hrs..... 126

Fig. 5.20: Schematic showing the relation between porosity, surface area [5.23]..... 128

Fig. 5.21: XRD patterns ZnO NWs and MAPbI_{3-x}Cl_x thin films deposited on a ZnO NW array synthesised with the chemical bath method at 90 and 110 °C 129

Fig. 5.22: XRD patterns ZnO NWs and MAPbI_{3-x}Cl_x thin films deposited on a ZnO NW array synthesised with the chemical bath method using an equimolar ratio of zinc acetate, HMTA and PEI of 25 mM and 70 mM 130



TABLE OF CONTENTS

<i>CHAPTER ONE: Background</i>	<i>1</i>
1.1 The South African Energy Mix	<i>1</i>
1.2 Photovoltaics and Their Role in Diversifying South Africa’s Energy Mix	<i>4</i>
1.2.1 First Generation Silicon Solar Cells	<i>6</i>
1.2.2 Second Generation Thin Film Solar Cells	<i>7</i>
1.2.3 Third Generation Solar Cells.....	<i>9</i>
1.2.4 Modern Nanostructure-Based Solar Cells.....	<i>11</i>
1.3 The Role of One-Dimensional Nanostructures in Perovskite Solar Cells.....	<i>12</i>
1.4 Challenges Facing MAPbI ₃ Perovskite Thin Films.....	<i>14</i>
1.4.1 MAPbI ₃ Instability Caused by Humidity.....	<i>15</i>
1.4.2 MAPbI ₃ Instability Caused by Light and Oxygen Exposure.....	<i>16</i>
1.4.3 MAPbI ₃ Instability Caused by Heat.....	<i>17</i>
1.5 Strategies to Improve MAPbI ₃ Morphology and Stability: Mixed-Halide Perovskites	<i>18</i>
1.6 Growth of MAPbI _{3-x} Cl _x Thin Films: Importance of Substrate Morphology during Perovskite Conversion.....	<i>19</i>
1.6.1 Deposition of MAPbI _{3-x} Cl _x Thin Films on TiO ₂ and ZnO Surfaces via Spin-Coating.....	<i>20</i>
1.6.2 Spin-Coating of MAPbI _{3-x} Cl _x Thin Films onto ZnO Nanowire Surfaces.....	<i>23</i>
1.7 Research Gaps.....	<i>24</i>
1.8 Aims and Objectives, Thesis Outline	<i>24</i>
References	<i>27</i>

CHAPTER TWO Experimental Techniques – Synthesis of ZnO Nanowire Arrays for Perovskite Thin Film Deposition..... 34

2.1	Crystal Structure of ZnO	34
2.2	Historical Background of the Hydrothermal Synthesis Technique	36
2.3	Chemistry Involved during Hydrothermal Synthesis of ZnO Nanostructures	36
2.4	ZnO Nanowire Array Growth on Substrates	39
2.5	ZnO Nanowire Synthesis Procedure	42
	2.5.1 AZO Substrate Preparation and Cleaning.....	42
	2.5.2 Zinc Nitrate Nutrient Solution Preparation.....	42
	2.5.3 ZnO Nanowire Synthesis using Autoclave Hydrothermal Reactor	43
2.6	Summary of Experimental Parameters	46
	References	49

CHAPTER THREE: Experimental Techniques: Mixed Halide MAPbI_{3-x}Cl_x Perovskite Film Synthesis on ZnO Nanowire Arrays..... 51

3.1	Introduction.....	51
3.2	The Spin-Coating Technique	51
3.3	MAPbI ₃ Thin Film Formation during One-Step Spin-Coating	53
3.4	Fundamentals of Nucleation and Crystal Growth	55
3.5	Morphology of MAPbI ₃ and MAPbI _{3-x} Cl _x Thin Films Spin-Coated on ZnO Surfaces	57
	3.5.1 Morphology of MAPbI ₃ Spin-Coated on ZnO Thin Films.....	57
	3.5.2 Morphology of MAPbI _{3-x} Cl _x Spin-Coated on ZnO Thin Films.....	58
	3.5.3 Morphology of MAPbI ₃ and MAPbI _{3-x} Cl _x Thin Films Spin-Coated on ZnO Nanowires	59
3.6	Ion Migration and the Role of Chlorine Ions in Improving the Quality of MAPbI _{3-x} Cl _x Layers.....	61
3.7	Phase Segregation and Cl Sublimation during Annealing.....	64
3.8	Deposition of Ossila Mixed-Halide Perovskite Precursor Ink on ZnO NW Arrays.....	66
	References.....	70

<i>CHAPTER FOUR: Analytical Techniques</i>	<i>74</i>
4.1 Introduction.....	<i>74</i>
4.2 Electron Microscopy.....	<i>74</i>
4.2.1 Scanning Electron Microscopy (SEM).....	<i>75</i>
4.2.2 Transmission Electron Microscopy (TEM)	<i>80</i>
4.3 X-Ray Diffraction (XRD).....	<i>87</i>
4.3.1 Crystal Structure and Bravais Lattice.....	<i>87</i>
4.3.2 Crystallographic Directions.....	<i>89</i>
4.3.3 Crystallographic Planes.....	<i>90</i>
4.3.4 The X-ray Diffractometer	<i>91</i>
4.3.5 Bragg's Law of Diffraction.....	<i>92</i>
4.3.6 Instrumentation and Data Acquisition.....	<i>93</i>
4.4 Ultraviolet-Visible Spectroscopy (UV-Vis Spectroscopy).....	<i>94</i>
4.4.1 Operating Principle of UV-Vis Spectroscopy.....	<i>95</i>
4.4.2 UV-Vis Spectra of Thin Films.....	<i>96</i>
4.4.3 Instrumentation and Data Acquisition.....	<i>97</i>
4.5 X-ray Photoelectron Spectroscopy (XPS).....	<i>98</i>
4.5.1 Operating Principle of XPS.....	<i>99</i>
4.5.2 Physics of Photoelectron Emission.....	<i>100</i>
4.5.3 Peak Identification.....	<i>102</i>
4.5.4 Instrumentation and Data Collection.....	<i>102</i>
References.....	<i>104</i>

CHAPTER FIVE: Results and Discussion	106
5.1 Introduction.....	106
5.2 Characterisation of the Aluminium-doped Zinc Oxide Substrate	106
5.3 High-Pressure Autoclave Synthesis of ZnO NW Arrays on AZO Substrates.....	110
5.4 Chemical Bath Synthesis of ZnO NW Arrays on AZO Substrates.....	113
5.5 Structural and Optical Characterisation of Chemical Bath Synthesised ZnO NWs	116
5.6 Optimisation of Perovskite Spin-Coating Conditions	120
5.7 Spin-coating and Conversion of Perovskite Layers on Different Nanowire Morphologies	123
References	131
CHAPTER SIX: Summary and Future Work	134



CHAPTER ONE

Background

1.1 The South African Energy Mix

Fossil fuels are formed by buried remains of plants and animals, which fossilised over millions of years; the most common of which are coal, crude oil and natural gasses [1.1]. As shown in Fig. 1.1, the South African energy mix is dominated by coal, which is a solid, carbon-heavy rock containing four different large carbon contents namely, bituminous, sub-bituminous, anthracite and lignite [1.1, 1.2]. Most of the coal reserves are located in the interior, north-eastern provinces of the country, namely Gauteng, Northwest and Mpumalanga and are extracted via underground or surface mining. Underground mining employs heavy machinery to remove coal from deep underground deposits, whereas surface mining detaches whole layers of soil and rock to access coal deposits [1.2].

Crude oil (better known as petroleum) makes up around 14% of the energy mix and can be considered a liquid comprising of hydrocarbons, found in underground crevices and cracks deep in the earth's surface. Owing to the low natural reserves, the country imports over 90% of its crude oil from Saudi Arabia, Nigeria and Angola [1.2], but has the second largest petroleum refining capacity in Africa, producing more than 500 000 barrels of crude and 200 000 barrels of synthetic fuel daily. Two important refineries companies are Sasol and the Petroleum Oil and Gas Corporation of South Africa (PetroSA) - Sasol uses both Coal-To-Liquids (CTL) and Gas-To-Liquids (GTL) technologies during refinery, whereas PetroSA produce synthetic products using GTL technology. Major refineries include Sapref and Enref in Durban, Chevron in Cape Town and Natref at Sasolburg.

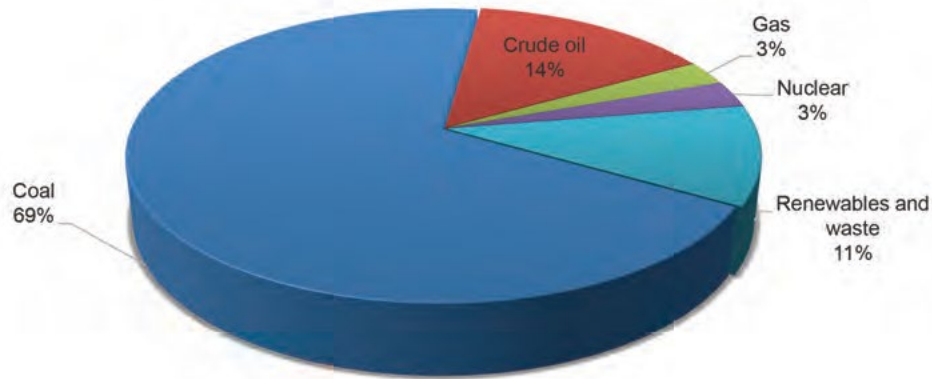


Fig. 1. 1: Pie-chart showing the South African energy mix in 2019 [1.1]

A much smaller contributor to the energy mix is natural gas, which in general, is a mixture of different non-hydrocarbon gases (e.g. carbon dioxide, nitrogen, helium etc.) and hydrocarbon gases such as methane. Coal-fired power plants dominate South Africa's electricity generation, with the State-Owned Enterprise (SOE), Eskom, responsible for over 90% of the country's electricity generation and distribution. In total, Eskom operates 15 coal-fired power plants, as shown in Fig. 1.2, totalling around 47 000 MW or 85% of the installed capacity. Because of this coal dependency, South Africa ranks as one of the largest CO₂ emitters per capita in the world [1.1, 1.2].

The extraction of fossils and subsequent manufacturing of fuels and products cause more harm to the planet than expected. Unearthing, processing, underground water piping systems and coal deposits require vast spaces of land, which threaten the natural habitats of large classes of animals. In extreme cases, complete animal extinction results due to drilling, transportation and burning of coal and oil spills during extraction and transportation. Not only is animal life threatened by these practices, but coal-fired power plants also produce excessive, poisonous mercury emissions, whereas petroleum powered trucks, cars and boats emit carbon monoxide and sulphur dioxide, which cause harmful respiratory illnesses among large sections of population [1.4, 1.5].

Eskom power stations

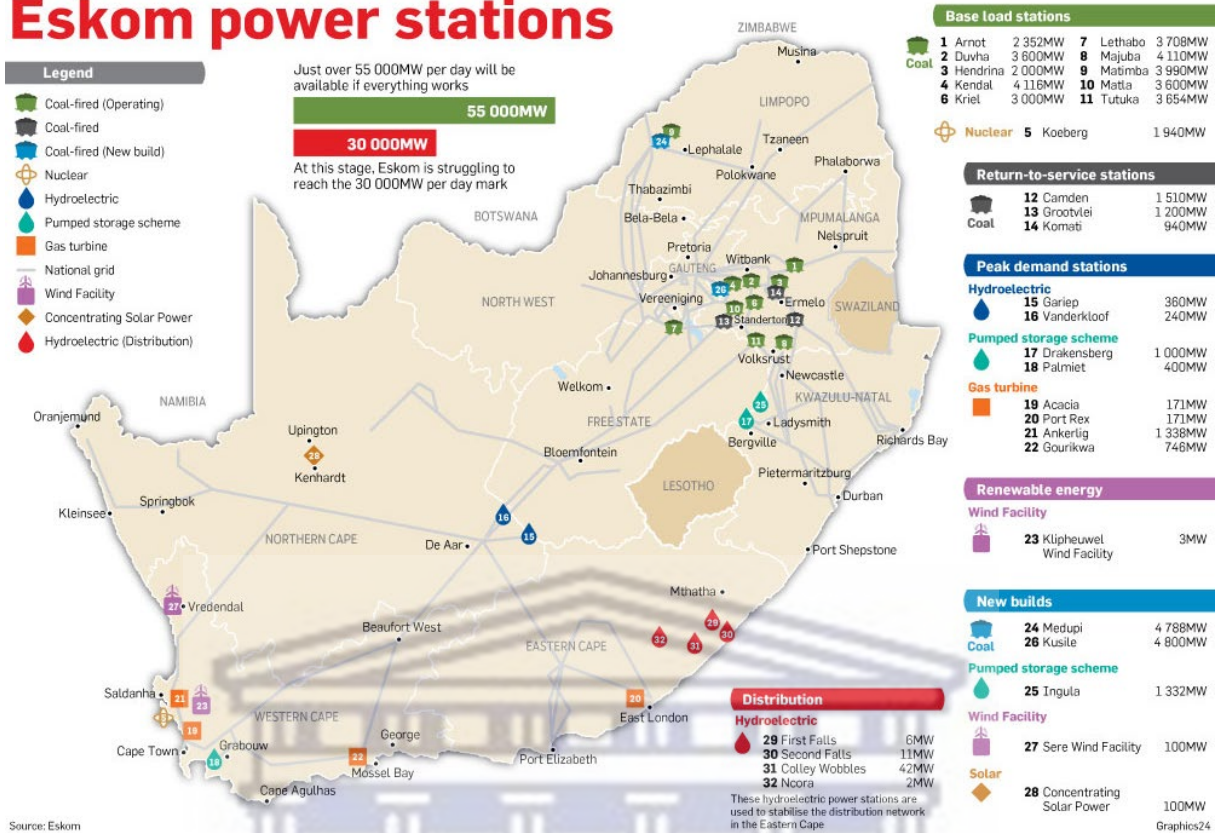


Fig. 1. 2: Eskom power generation and distribution network [1.1]

From an economic viewpoint, fossil fuels, considered non-renewable because of the finite amount of fossil sources available, need expensive operations, becoming more expensive as the energy demand increases with the increase in global population and industrialisation. As such, it is understood that humans are in urgent need of environmentally friendly, cost-effective renewable energy sources to sustain all life in present and future generations. Renewable energy, often referred to as the clean energy, as it comes from natural resources that constantly recharges itself in less than a human lifetime without exhausting the planet's resources. The most common renewable sources are sunlight, wind, biomass, rain, tides, thermal energy and waves, which are relatively easily accessible and converted into an energy form for daily human consumption. However, in South Africa, the renewable energy sector is relatively new compared to established economies in the USA, Europe, and Asia [1.1 - 1.3].

1.2 Photovoltaics and Their Role in Diversifying South Africa's Energy Mix

Solar energy is the most attractive renewable option for diversifying the South African energy mix and systematically decreasing the reliance on coal for electricity generation. To that end, photovoltaics (PVs) provides the only direct means of converting the country's abundant annual sunlight into electrical energy. The South African government has implemented several initiatives to promote the use of photovoltaics, including financial incentives for households and businesses to install solar panels and the development of large-scale solar projects. Despite these efforts, the growth of the photovoltaic industry in South Africa has been hindered by a lack of consistent policy and regulatory support, as well as high upfront costs for solar installations. Nevertheless, the potential for photovoltaics to contribute to the country's energy mix and reduce dependence on fossil fuels remains significant [1.3].

Direct conversion of solar energy (or light) into electrical energy by means of a material is known as the photovoltaic effect, and was first discovered by French physicist, Edmond Becquerel in 1839. Albert Einstein continued work in this field, but was not satisfied with the description of energy in the 1800s, as he believed that light contains packets of energy, which he called light "*quanta*", now known as photons. He postulated that the amount of power that these quanta carried changes according to the wavelength of light; the shorter the wavelength the more power and vice versa. Einstein's description of light combined with the discovery of the electron paved the way to explaining the photovoltaic effect. During the conversion, photons with enough energy to overcome the energy bandgap of the semiconductor are absorbed and their energy transferred to the electrons, resulting in electron promotion to higher energy states within the material. However, the electrons may instantly de-excite back to their original (or ground) state, which is undesirable for current generation [1.6].

As such, semiconductors are "*doped*" with an impurity element, which introduces energy states within the bandgap of the material [1.6]. These doped states afford a semiconductor to have either an abundance (n-type) or scarcity (p-type) of electrons. When combining an n-type and p-

type semiconductor, a so-called p-n junction arises, which is the central idea when constructing a PV device. The extra energy arising because of photon absorption generates a potential difference or electron motive force (emf) that drives the electrons through a load in the external circuit. A schematic of the PV effect is shown in Fig. 1.3 [1.7].

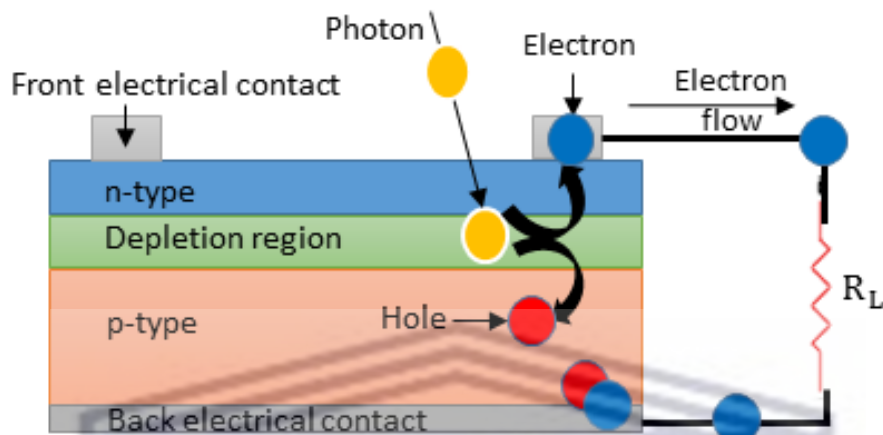


Fig. 1. 3: Schematic of the photovoltaic effect [1.7]

American physicists, Daryl M. Chapin and Gerald L. Pearson, along with American chemist Calvin S. Fuller, invented the first working PV cell in the early 1950s. Their collaboration emanated from the work done by Chapin, who initially did research on magnetic materials at Bells Laboratories. His quest was to develop power sources for telephone systems in damped areas, where dry cell batteries decayed rapidly. Chapin eventually found that solar power is a promising source and worked on selenium (Se) based solar cells. However, he discontinued his work due to Se's inefficiency. At the same time, Pearson and Fuller worked on altering the properties of semiconductors by doping the material with impurities. Fuller synthesised silicon (Si) chips doped with gallium (Ga) impurities, with the aim of converting the Si into a n-type semiconductor; this means that the Si structure has an abundance of electrons compared to intrinsic (in other words, undoped) Si. Fuller supplied the n-type Si (n:Si) to Pearson, who worked on p-type semiconductors by doping silicon with lithium (Li). Pearson sandwiched the p- and n-type wafers together to form a p-n junction, or more commonly called, diode. Initial solar illumination and testing were remarkably good, which led to the collaboration with Chapin and the development

of the modern silicon solar cell. Subsequent work aimed at improving the electrical contacts of the device and the doping efficiency by using different dopants, with Ga eventually replaced by boron (B) and arsenic (As) replacing Li. After perfecting the design, a series connected combination of solar cells was created and called a “*solar battery*”; the first solar cells converted solar energy in electrical energy at 6 % conversion efficiency [1.8, 1.9]

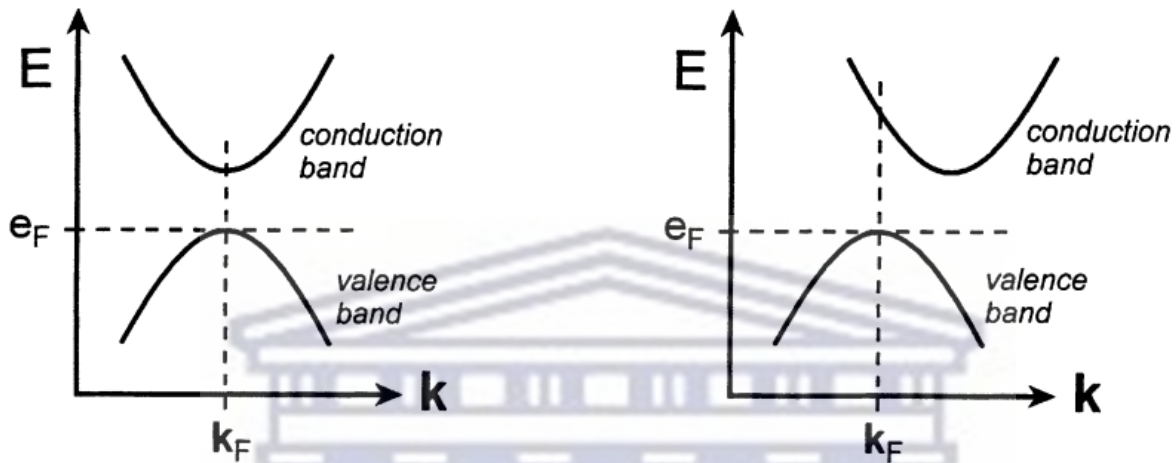


Fig. 1. 4: Direct and indirect band gaps [1.10]

1.2.1 First Generation Silicon Solar Cells

Silicon, the most abundant raw element on earth, was used to make the first solar cell in 1954 [1.9] and remains the most widely used semiconductor for PV manufacturing. Pure silicon has an indirect band gap of 1.12 eV, which allows the material to absorb photons in the visible region of the electromagnetic spectrum. As shown in Fig.1.4 an indirect bandgap occurs when the valence and conduction band edges are not aligned in k space [1.10]. K space is a coordinate system, which is used for counting quantum states and describing band gaps. There are three types of silicon used in the first-generation solar cells namely, single crystalline silicon, multicrystalline silicon and amorphous silicon. Multi- (or poly-) crystalline silicon is the most widely used commercially due to its efficiency and lower cost. These devices typically have an efficiency of

about 21% and are slightly less expensive to produce than single-crystalline cells. Amorphous silicon has a much lower efficiency at 16% but it is much cheaper to manufacture compared to both single and poly-crystalline silicon. Single crystalline silicon PVs have an efficiency of 28% and is the most expensive to produce. An example of a first generation crystalline silicon PV is shown in Fig. 1.5 [1.11].

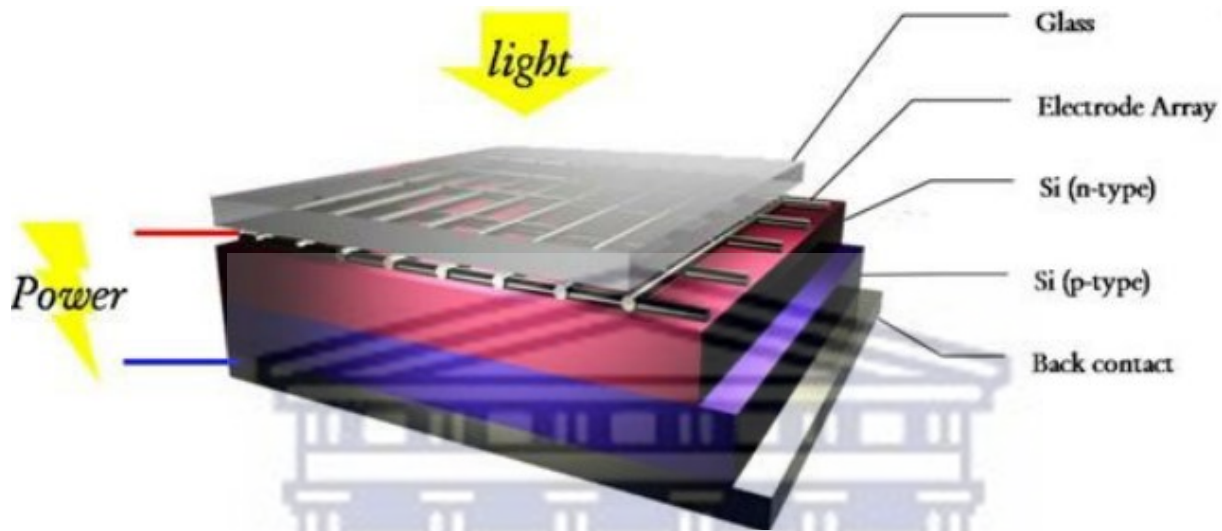


Fig. 1. 5: First generation solar cell [1.11]

1.2.2 Second Generation Thin Film Solar Cells

The second generation of photovoltaics was based on thin film technology that allowed for minimal material consumption and ultimately lower production costs. There are three types of thin film cells: amorphous silicon, copper indium gallium diselenide ($CuIn_xGa_{1-x}Se_2$, CIGS) and cadmium telluride (CdTe). Amorphous silicon is the most commercially used of these because they can use existing silicon solar cell technology for manufacturing, but these cells have a couple of disadvantages. There are a few fundamental differences between second generation solar cells and first generation solar cells. The most notable difference is the semiconductor material used in the cell has a direct band gap as opposed to the indirect band gap of silicon, but these cells still rely on a p-n junction design. Thin film cells have a top layer called the window layer

made of a large band gap material that absorbs the higher energy photons and a bottom layer called the absorber layer made of a smaller band gap material that absorbs the lower energy photons, which are not absorbed by the window layer. The literature shows that amorphous silicon has less efficiency of 16%, CdTe has efficiency of 17% and CIGS cells have the highest efficiencies of 20% [1.11].

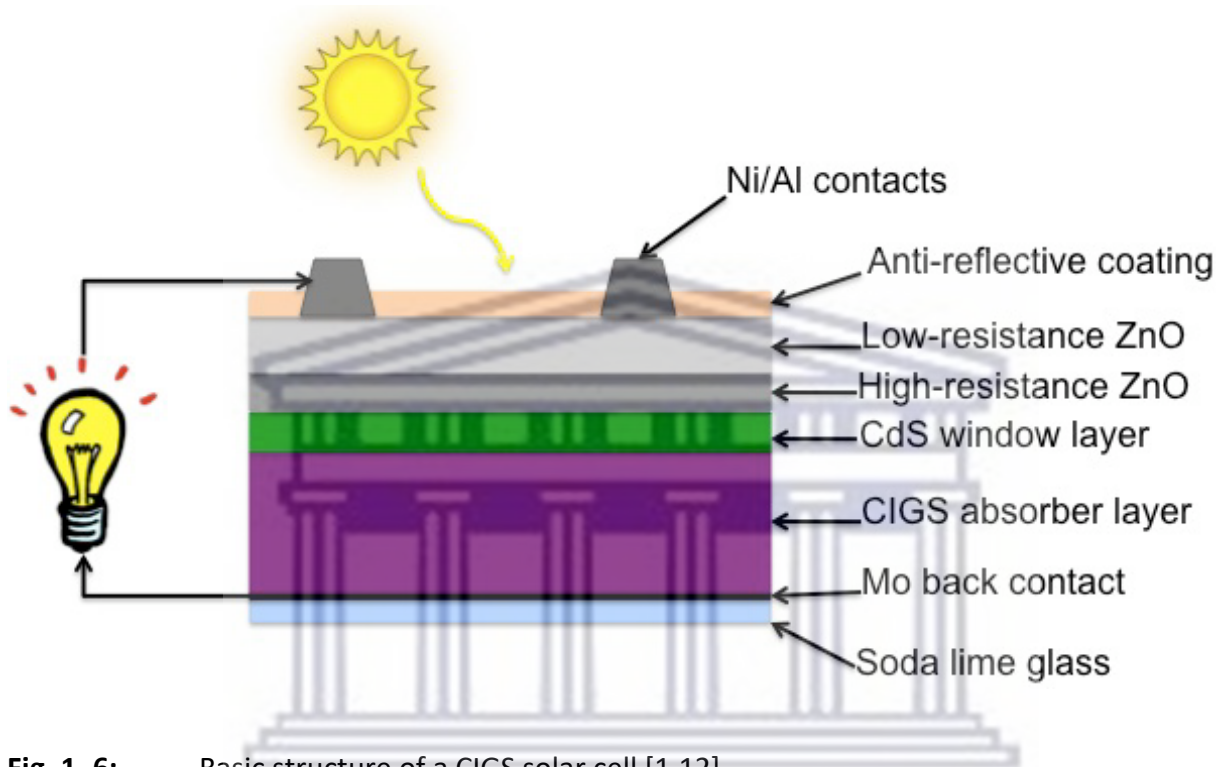


Fig. 1. 6: Basic structure of a CIGS solar cell [1.12]

The typical structure of CIGS thin film solar cell is shown in Fig. 1.6. The glass substrate is typically soda lime glass due to the fact that the sodium diffuses into the CIGS layer and increases conductivity and reduces the formation of lattice defects. Molybdenum (Mo) is used as a back contact for energy flow. CdTe is also used an absorber layer as shown in Fig. 1.7. Similar to CIGS devices, a CdTe solar cell also employs a CdS window layer, however fewer additional layers are used, making these devices slightly cheaper to manufacture compared to CIGS cells. Although 2nd generation PVs are less expensive to manufacture compared to 1st generation silicon technologies, they do have disadvantages. Most of the material used to make these solar cells are either becoming extinct or more expensive or are highly toxic. In order to have mass

production of these solar cells new facilities are required which would tremendously increase the cost of production [1.12].

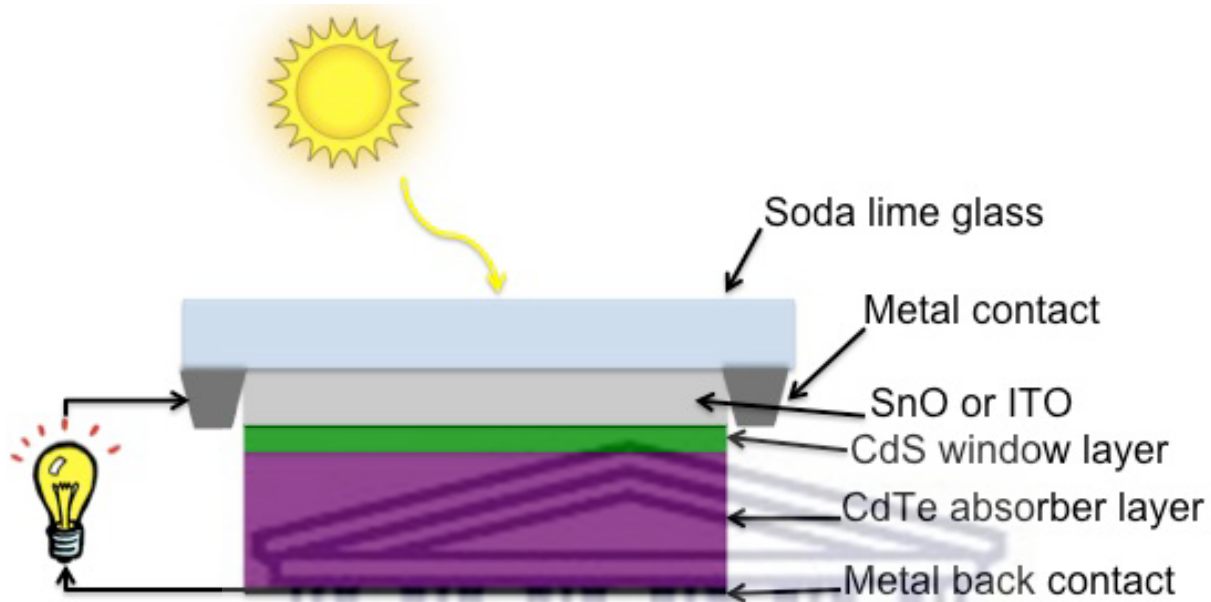


Fig. 1. 7: Basic structure of a CdTe solar cell [1.12]

1.2.3 Third Generation Solar Cells

Third generation of solar cells became evident due to the high costs associated to 1st generation PVs, as well as the toxicity and limited availability of materials for 2nd generation solar cells. These cells do not depend on the p-n junction design of the others but rather make use of nanomaterials and photo-sensitisers. Different models of third generation cells exist, which include dye-sensitised solar cells (DSSC) [1.13], organic or polymer solar cells [1.14] as well as inorganic solar cells [1.15]. DSSCs, also known as Gratzel cells after its developer, Prof Michael Gratzel, separate the absorption of photons from charge generation within the cell. This is unlike traditional 1st and 2nd generation PVs, where light absorption and dissociation of electron-hole pairs to generate charge carrier occur at the same physical position within the cell. In a DSSC, an organometallic dye absorbs photons in the visible range, direct injects the electrons generated from absorption into the band gap of a wide band gap semiconductor, and charge separation occurs at the

interface of the dye and the semiconductor. The cell also contains electrolyte to assist in hole transport. The highest efficiency for DSSCs reported is 15.2% [1.16]. These cells are very inexpensive to make but photodegrade in a short period of time and the electrolytes tend to leak very easily. Elsewhere, polymer solar cells can be made to be flexible, allowing new application avenues, such as wearable technologies, role-to-role printing for building window applications and so forth [1.17]. They consist of the active layers are completely made of organic materials. These cells can either have a bilayer structure or a bulk-heterojunction structure but the mechanism of the design remains the same. The active layer of the cells is made up of donor and acceptor polymer materials for charge separation and transportation, respectively [1.14].

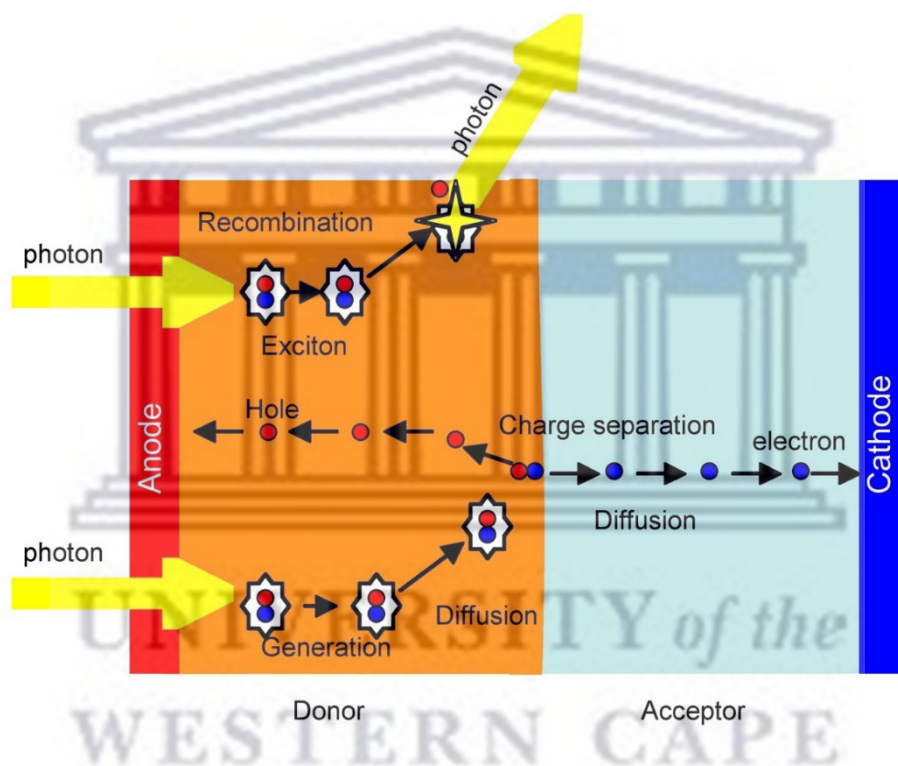


Fig. 1. 8: Diagram that shows the mechanism of an organic solar cell [1.17]

In bilayer cells, electron-hole recombination is much less prevalent due to the fact that the electron and hole are separated at the interface of the material. The design has flaws, however, because the bilayer only has one active zone, which is the interface. Because the excitons have

to diffuse to the interface few of them go the distance, energy conversion is low. In order to avoid this issue the bulk-heterojunction cells are made up of donor and acceptor materials mixed throughout the active layer. Because the acceptor and donor materials are so well mixed, the active zone for this cell is much larger hence, the energy conversion is much higher [1.14, 1.17]

1.2.4 Modern Nanostructure-Based Solar Cells

Nanostructured solar cells, also called 4th generation, modern or emerging PVs in some literature, enhance light harvesting by making use of different forms of nanostructures. From a commercial view, nanostructures allow for less material to be used during device fabrication without additional costs [1.18], whereas from a scientific point-of-view, nanomaterials are very interesting as the physical and chemical properties change drastically as the dimensions are reduced from bulk to nanosized [1.19]. For instance, the melting point is lowest for nanomaterials compared to its bulk material, which is caused by a decrease in the atomic cohesive energy at the nanoscale; this decrease is directly related to an increase in the volume of surface atoms compared to the core atoms of a nanomaterial [1.19]. To further benefit out of these interesting properties, a vast number of different nanostructures are researched daily, including nanowires, quantum dots, nanopillars, nanocones, to name a few.

Of particular interest to this study is modern perovskite solar cells (PSCs) employing nanostructured ZnO [1.20]. These emerging PVs are attracting a lot of research interest and already has demonstrated efficiencies comparable to that of 1st generation single-crystalline silicon PVs [1.20 - 1.22]. In general, halide perovskites (HPs) have the same crystalline structure as mineral perovskites, i.e. ABX_3 , where A and B are cations, and X an anion, as shown in Fig. 1.9 (a) and (b) [1.21]. A special halide perovskite, methylammonium lead iodide ($CH_3NH_3PbI_3$ or $MAPbI_3$), have been successfully applied as a light-absorbing layer in solar cells. In $MAPbI_3$ the A site in the unit cell is occupied by a methylammonium (MA) cation, the B site contains a Pb ion and the X anion sites are occupied by iodine halides. This is shown in shown in Fig. 1.9 (c). Newer large anions, such as formamidinium (FA) have also been researched extensively, in place of MA,

which has already seen a record of 25.8% realised [1.22]. Simple solution-based techniques can be used to deposit perovskites, which are far more cost-effective and easier to scale up than the complicated, vacuum systems used to make silicon-based PVs [1.20 – 1.22]. The crystalline and physical properties of MAPbI₃ will be discussed in depth in Chapter 3, as this is still the most promising perovskite material for large-scale commercialisation of the technology, and will be the core focus of this study.

1.3 The Role of One-Dimensional Nanostructures in Perovskite Solar Cells

One-dimensional (1D) nanostructures play a crucial role in perovskite photovoltaics by improving their efficiency and stability. In some cases, they are used as light-absorbing materials, however in most cases they are employed to increase light absorption by reducing reflection, while also acting as an electron transport layer (ETL) in the device. Additionally, these 1D nanostructures can be engineered with specific optical and electrical properties, which further enhances their performance in solar cells [1.23, 1.24]. One-dimensional ZnO nanowires, in particular, has shown great potential as an effective electron transport medium in MAPbI₃ PSCs [1.24]. A schematic of a PSC employing a layer of vertically aligned ZnO NWs (a so-called NW array) is shown in Fig. 1.10.



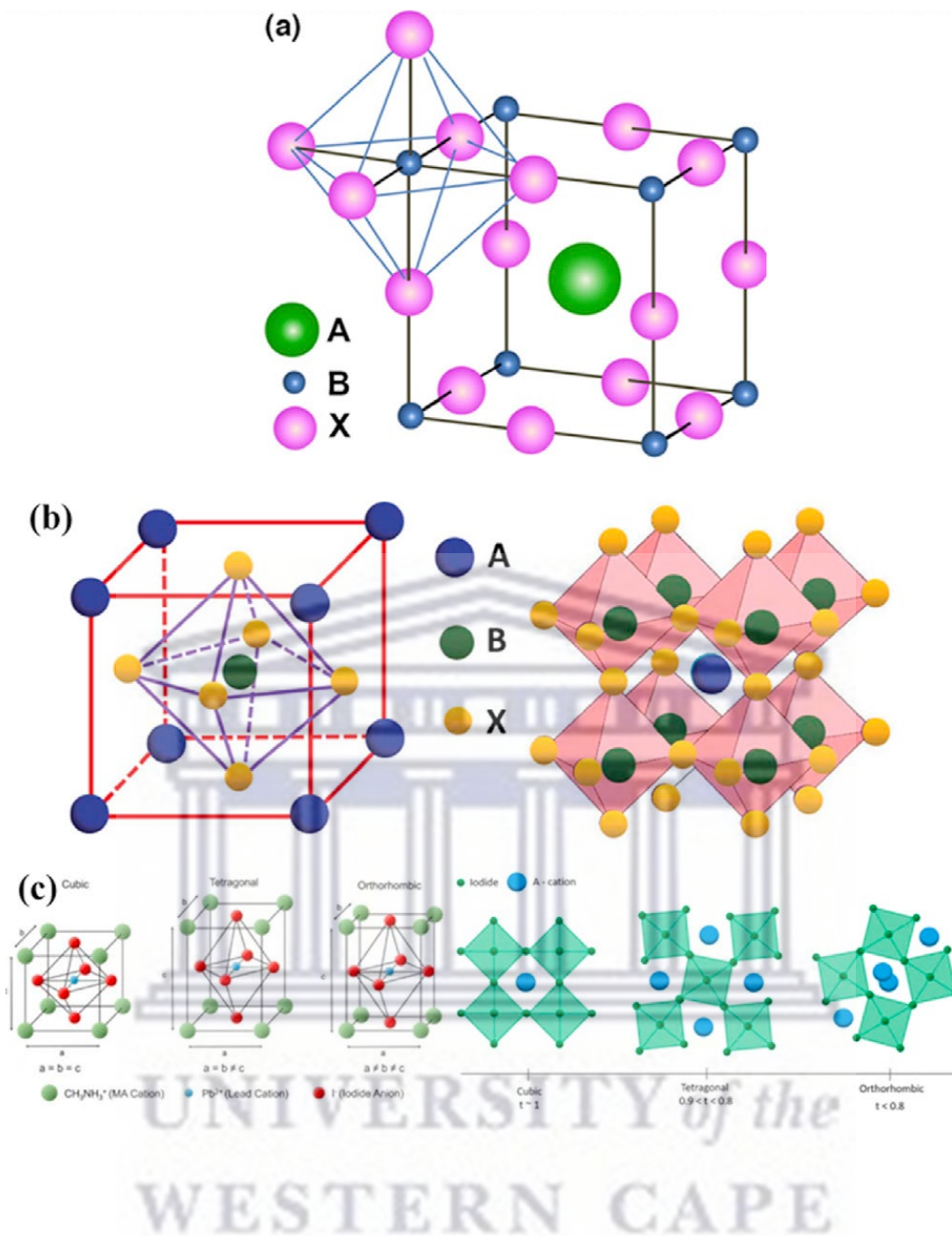


Fig. 1. 9: (a) Perovskite crystal structure, (b) BX₆ octa-hydra, (c) cubic, tetragonal and orthorhombic phases of MAPbI₃ perovskite [1.21]

The success of ZnO nanowires in PSCs stems from the materials' natural n-type nature (i.e. has an abundance of conduction electrons in the lattice), direct wide bandgap of 3.36 eV and a relatively high exciton binding energy of 60 meV at room temperature. These properties allow ZnO to be an excellent electron transport material, with a charge carrier mobility up to $1 \text{ cm}^2 \text{V}^{-1} \text{s}^{-1}$ at room temperature [1.25]. In addition, the various forms of ZnO are also relatively easy to fabricate, including the sol-gel method [1.26], chemical [1.27] and physical vapour deposition [1.28], electrochemical deposition technique [1.29] and hydrothermal technique [1.30], which makes these materials highly popular and widespread in literature.

Of the above methods, hydrothermal synthesis poses as the simplest means to fabricate ZnO nanowire arrays and will be used in this study. Although the technique is well researched, there are still outstanding research questions pertaining to their use in PSCs. In particular, widespread interest remains in understanding the effect of the nanowire structure (diameter, length, areal density) on the morphology of the ensuing MAPbI₃ thin film. There is also much work to be done in understanding the mechanism of electron transport through the array, given nanosized effects such as quantum confinement, oxygen deficiencies and surface states [1.31].

1.4 Challenges Facing MAPbI₃ Perovskite Thin Films

MAPbI₃ thin films face several challenges prior to their application in solar cells. These include stability, toxicity, scalability, reproducibility, efficiency and cost. From a research perspective, the most important factors to address are the structural instability, reproducibility and toxicity. The instability is caused by exposure to heat, light [1.32] and moisture [1.33], which may cause degradation of the MAPbI₃ crystal structure.

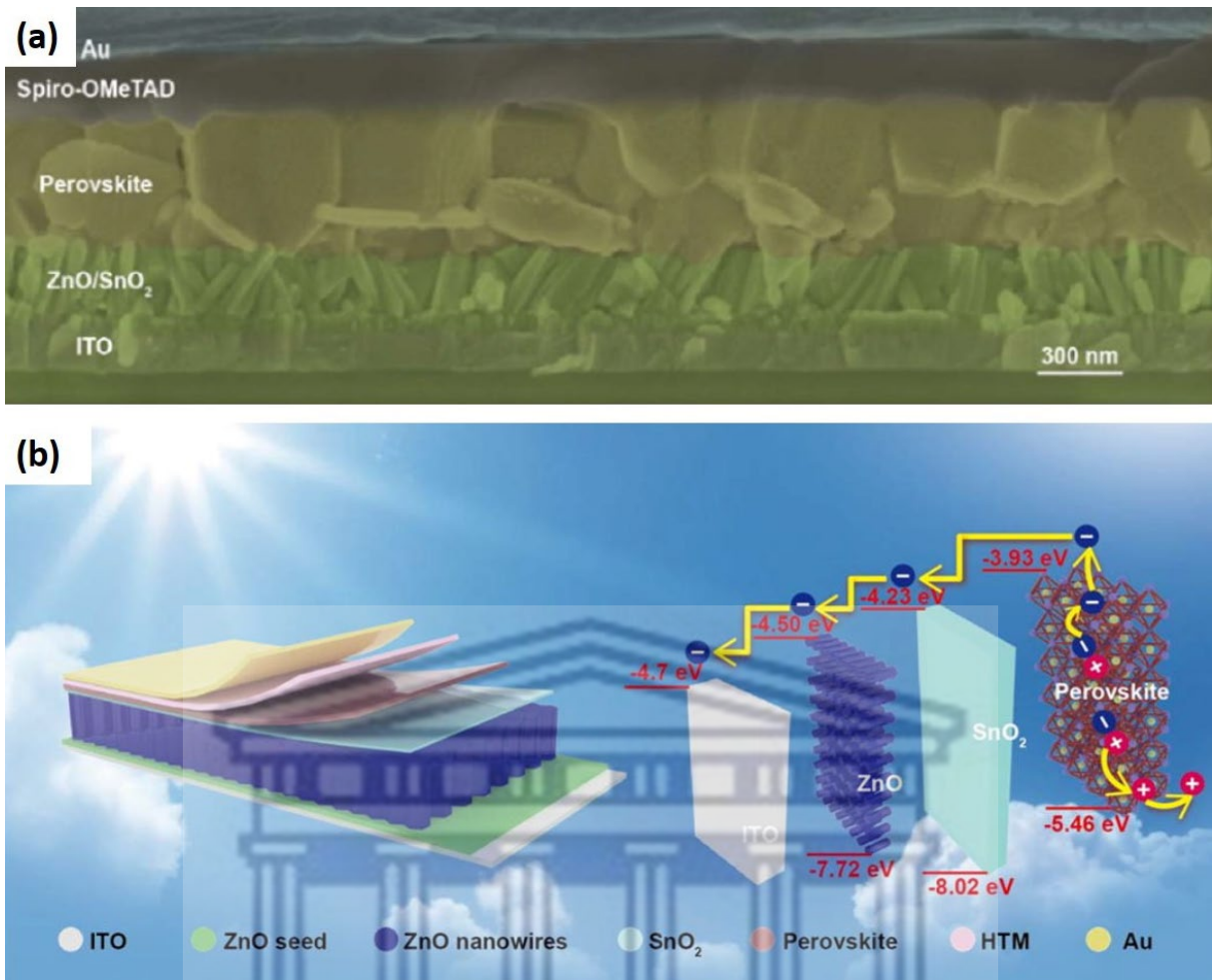


Fig. 1. 10: (a) Cross-sectional view of of ZnO-based perovskite solar cells; (b) schematic of the solar cell design [1.24]

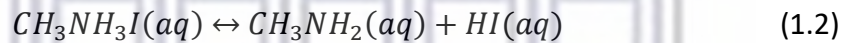
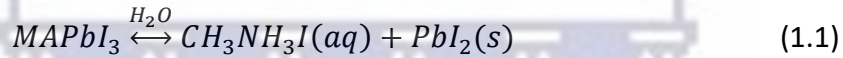
1.4.1 MAPbI_3 Instability Caused by Humidity

Studies on the instability caused by moisture/humidity are well reported in literature. Initial reports suggested that the absorption of moisture by the MAPbI_3 layer results in its decomposition into CH_3NH_2 , PbI_2 and hydrogen iodide (HI) [1.33]. However, subsequent studies suggest a more complicated degradation model of the ABX_3 crystal. Yang *et al.* [1.35] found that the absorption of H_2O by MAPbI_3 resulted in a reversible hydrate form, $\text{MA}_4\text{PbI}_6 \cdot 2\text{H}_2\text{O}$, containing PbI_6^{4-} octahedra. These findings were further investigated by Leguy *et al.* [1.36] who found that the films convert into a monohydrate form ($\text{MAPbI}_3 \cdot \text{H}_2\text{O}$) throughout the film depth, indicating

that H₂O easily diffuses to the bottom of the perovskite layer along the grain boundaries. The model further explains that the corner-sharing PbI₆ octahedra is broken into one-dimensional double chains consisting of two neighbouring octahedra (so called MAPbI₃·H₂O, monohydrate form) and subsequently into zero-dimensional, isolated octahedra (MA₄PbI₆·2H₂O, dihydrate form) due to the H₂O intercalation. It was further found that these hydrate forms are fully reversible back into MAPbI₃ when exposed to N₂ gas for 5 to 6 hours at room temperature [1.36].

1.4.2 MAPbI₃ Instability Caused by Light and Oxygen Exposure

The degradation studies summarised in 1.4.1 were performed in the dark. Similar studies performed under light found that moisture coupled with light decomposes the MAPbI₃ structure into irreversible PbI₂ and other products. This degradation mechanism can be summarised as follows [1.37]:



Firstly, due to the high sensitivity of CH₃NH₃PbI₃ to water, it hydrolyses in the presence of moisture to form PbI₂ and CH₃NH₃I, as shown in reaction (1.1). The equilibrium of reaction (1.2) leads to the co-existence of CH₃NH₃I, CH₃NH₂ and HI in the layer. Hydrogen iodide (HI) in liquid form is unstable and quickly degrades in two ways: the first is the redox reaction in the presence of oxygen (1.3) and the second the photochemical reaction, whereby HI decomposes into H₂ and I₂ under UV illumination (1.4).

As the degradation of the perovskite layer is highly sensitive to moisture, oxygen and light, most of the thin film deposition is performed in a glove box under an inert environment, such as N₂ or Ar [1.38]. However, this is undesirable as real-life PV devices are measured under ambient

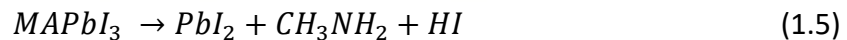
conditions. As such, significant degradation of the MAPbI₃ perovskite is usually observed when incorporated in solar cells. This is observed by a colour change from dark brown to yellow, as shown in Fig. 1.11 [1.39]. This degradation leads to unwanted efficiency decreases, which restricts the outdoor applications of PSCs.



Fig. 1. 11: Degradation of MAPbI₃ thin films, demonstrated by a change in colour from dark brown to yellow, with progressive decrease in the halide concentration [1.39]

1.4.3 MAPbI₃ Instability Caused by Heat

Photovoltaics must be stable at temperatures up to 85 °C, according to International Electrotechnical Commission (IEC) 61646 climatic chamber test [1.33]. Philipe *et al.* [1.40] found that MAPbI₃ partially decomposes to PbI₂ in vacuum when increasing temperature from 27 to 100 °C. They measured a ratio of 85:15 at 27 °C and 70:30 at 100 °C. When increasing the temperature to 200 °C, they found a MAPbI₃:PbI₂ ratio of 0:100, i.e. the MAPbI₃ film completed converted into PbI₂. The proposed mechanism of degradation under heat is similar to that discussed for heat and light degradation and can be summarised as follows:



One addition to the model for light degradation (reactions 1.1 to 1.4), is the further degradation of PbI₂ into Pb and I₂, caused by heat as shown by reaction (1.6). A study by Misra *et al.* [1.41] further shows that much slower perovskite degradation occurs at ambient pressure compared to

high vacuum, even at the same temperature [1.40]. However, these results show that the exposure of the perovskite to concentrated sunlight, corresponding to 100 suns, show significant thermal and photo instability of the MAPbI₃ thin films and the associated risks of lead emission into the environment.

1.5 Strategies to Improve MAPbI₃ Morphology and Stability: Mixed-Halide Perovskites

Research investigating the improvement of MAPbI₃ stability predominantly focuses on chemical engineering of the perovskite structure. In particular, the partial substitution of the iodine ions with different halides, such as Br and Cl, is well researched and thus called *mixed-halide perovskites*. Noh *et al.* [1.39] studied MAPbI_{3-x}Br_x mixed-halide films and found that they remain relatively stable after 20 days of exposure to 55% room humidity. Elsewhere, Ruess *et al.* [1.42] investigated the effect of both humidity and light on MAPbI_{3-x}Br_x with partially substituted Br and found suppression of the irreversible PbI₂ phase upon increased Br substitution and an increase in the monohydrate phase [1.35]. The superior stability of MAPbI_{3-x}Br_x is attributed to improved hydrogen bonding between NH³⁺ and the halide ions, which in turn stabilises the framework containing corner-sharing (PbI₆) octahedral [1.43]. However, under illumination, it was found that the light exposure results in halide segregation in the MAPbI_{3-x}Br_x structure, which effectively suppressed the effect of partial substitution and thus inevitably formed PbI₂.

The most common mixed-halide perovskite is the MAPbI_{3-x}Cl_x structure, with I atoms partially substituted by Cl. Stranks *et al.* [1.44] showed that the diffusion length of electrons and holes in the MAPbI_{3-x}Cl_x layer was greater than 1 μm and that Cl doping markedly improves both stability and conductivity of the perovskite. Docampo *et al.* [1.45] prepared MAPbI_{3-x}Cl_x films using a two-step dip-coating method and achieved a light current density of 22 mA.cm⁻² and a conversion efficiency of 15.41% when applied in a solar cell. Furthermore, they found that the lifetime for photo-induced electrons reached 300 ns and the initial absorption edge for light absorption was improved. Following these interesting findings, the PV application of MAPbI_{3-x}Cl_x increased

rapidly and to date is the most studied mixed-halide structure for PV applications. To understand the improved performance during PV application, Mosconi *et al.* [1.43] used first principle modelling and reported that the aggregation of Cl ions at the perovskite/ETL interface enhanced the binding energy between the $\text{MAPbI}_{3-x}\text{Cl}_x$ and the (110) crystal surface and a TiO_2 ETL layer. In addition, it they also showed that the interaction between the $\text{MAPbI}_{3-x}\text{Cl}_x$ and TiO_2 layer adjusted the electronic structure of the interface and an electron tunnelling effect resulted, thereby improving the air stability and conductivity of the perovskite layer. Given these results, mixed-halide $\text{MAPbI}_{3-x}\text{Cl}_x$ will also be used as the perovskite material of choice in this study.

1.6 Growth of $\text{MAPbI}_{3-x}\text{Cl}_x$ Thin Films: Importance of Substrate Morphology during Perovskite Conversion

Mixed-halide $\text{MAPbI}_{3-x}\text{Cl}_x$ is commonly synthesised by wet-chemical routes, during which a mixture of methyl ammonium iodide ($\text{CH}_3\text{NH}_3\text{I}$) and lead chloride (PbCl_2) are dissolved in dimethyl formamide (DMF) in a 3:1 ratio. The perovskite ink is then spin-coated onto a substrate and heated on a hot surface, resulting in the conversion to a mixed-halide with trace amounts of chlorine, given by the formula $\text{CH}_3\text{NH}_3\text{PbI}_{3-x}\text{Cl}_x$. This method is known as the *one-step spin-coating* method. A two-step spin-coating method is also commonly used, which involves dissolving PbCl_2 in DMF and MAI in isopropanol (IPA) followed by a sequential spin-coating process. In the first step, the MAI+DMF solution is spin-coated onto the substrate to form a base layer. This is followed by drop-coating the PbCl_2 +IPA solution onto the base layer at a different spin-rate, followed by heating on a hot-plate, as shown in Fig. 1.12 [1.46]. The spin-coating technique, both one- and two-step, has proven to be the most cost-effective and simple route for high-quality perovskite deposition and thus will be the deposition technique of choice throughout in this study.

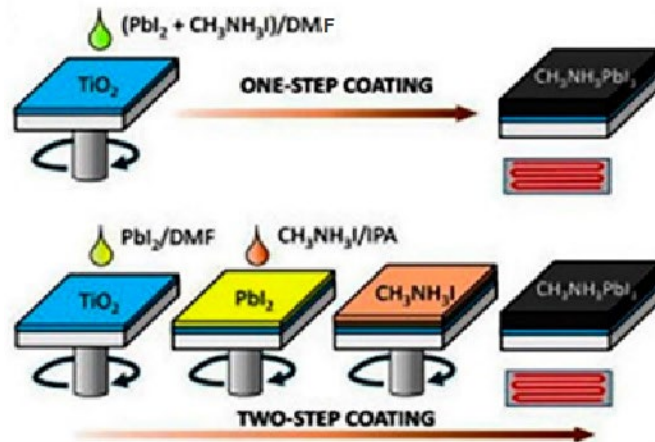


Fig. 1. 12: Synthesis strategies followed during one-step and two-step spin-coating to form MAPbI_{3-x}Cl_x mixed halide perovskite thin films on a substrate [1.46]

1.6.1 Deposition of MAPbI_{3-x}Cl_x Thin Films on TiO₂ and ZnO Surfaces via Spin-Coating

Metal-oxide TiO₂ and ZnO thin films are the most common ETLs used in perovskite-based PVs. The deposition of MAPbI_{3-x}Cl_x on these surfaces is widely studied and it is readily shown that the morphology of the perovskite highly depends on the topography of the underlying metal-oxide layer. As will be shown by the literature below, it is crucial to have complete control of the metal-oxide layer in order to control the morphology of the MAPbI_{3-x}Cl_x film.

Philippe *et al.* [1.40] used the one-step spin-coating method to deposit MAPbI_{3-x}Cl_x with different I:Cl ratios on a 650 nm thick layer of TiO₂, which in turn, was spin-coated onto an FTO/glass substrate. As shown in Fig. 1.13, the I:Cl ratio highly influences both the coverage, grain formation and overall morphology of the perovskite on the TiO₂ surface. It can also be observed that the perovskite coverage on the TiO₂ layer was not uniform; this is a common result of the one-step method.

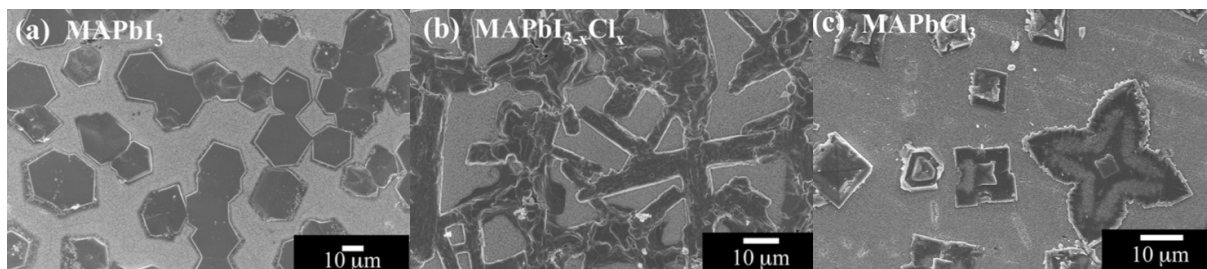


Fig. 1. 13: Scanning electron microscope images of (a) MAPbI_3 ($\text{Cl} = 0$); (b) $\text{MAPbI}_{3-x}\text{Cl}_x$ and (c) MAPbCl_3 ($\text{I} = 0$) deposited on a TiO_2/FTO substrate [1.40]

In contrast, Xu *et al.* [1.47] used the two-step method to deposit MAPbI_3 (Fig. 1.14 (a)) and $\text{MAPbI}_{3-x}\text{Cl}_x$ (Fig. 1.14 (b)) perovskites onto 500 nm thick TiO_2 layers. As shown in the images, the MAPbI_3 layer contained small crystal grains and a significant number of *pinholes*, while the $\text{MAPbI}_{3-x}\text{Cl}_x$ films contained micron-sized grains with very high coverage of the TiO_2 surface. In addition, the group showed that an increase in the Cl decreases the pinholes while simultaneously improving the crystallinity by increasing the grain sizes.

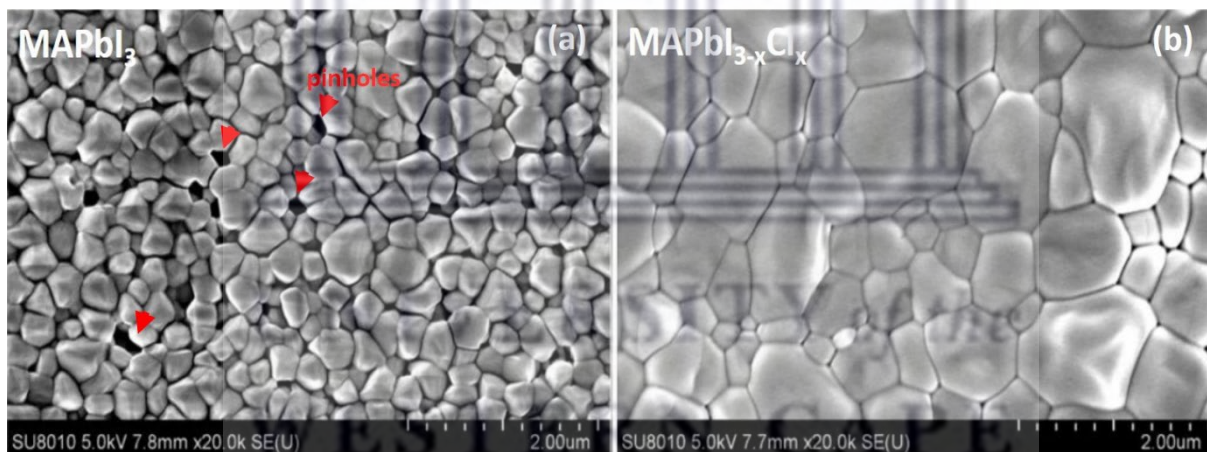


Fig. 1. 14: SEM images of (a) $\text{CH}_3\text{NH}_3\text{PbI}_3$ and (b) $\text{CH}_3\text{NH}_3\text{PbI}_{3-x}\text{Cl}_x$ [1.47]

To demonstrate the direct impact different TiO₂ morphologies have on the mixed-halide perovskite structure, Ueoka *et al.* [1.48] used one-step spin-coating to deposit MAPbI_{3-x}Cl_x thin films on TiO₂ layers with different nanoparticle sizes. The different TiO₂ nanoparticle sizes yielded visibly different perovskite layers, as shown in Fig. 1.15.

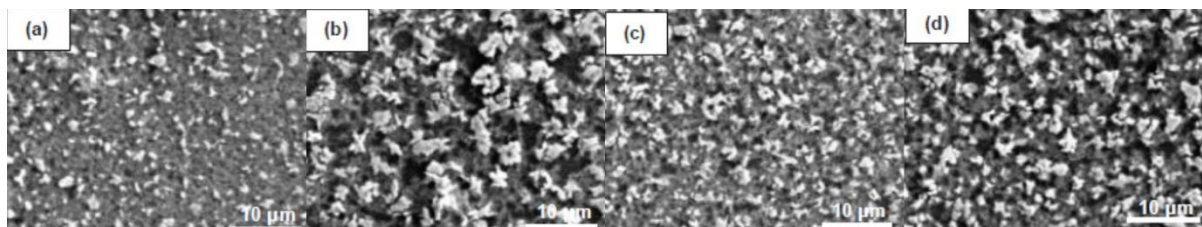


Fig. 1. 15: Scanning electron microscope images of MAPbI_{3-x}Cl_x thin films grown on compact TiO₂ layer containing (a) no TiO₂, (b) 3 nm TiO₂, (c) 16 nm and (d) 23 nm mesoporous TiO₂ nanoparticles [1.48]

The effect of different ZnO morphology on MAPbI_{3-x}Cl_x film characteristics is much more pronounced, compared to TiO₂. Bastiani *et al.* [1.49] spin-coated (one-step) MAPbI_{3-x}Cl_x films on a 1 μm thick ZnO thin film containing nanoparticle sizes ranging between 20 and 70 nm, as shown in Fig. 1.16. The different ZnO porosities lead to the formation of perovskite microstructures with vastly different morphologies. In particular, nucleation on 70 nm ZnO NPs gives rise to bridge-connected, condensed domains a few micrometers in diameter, whereas deposition on 50 nm particles yields clusters without the bridge connections and lower coverage of the ZnO film. Fig. 1.16 (c) shows that a completely different morphology is obtained when the ZnO size is further reduced to 20 nm, with a fibrous, elongated perovskite structure produced.

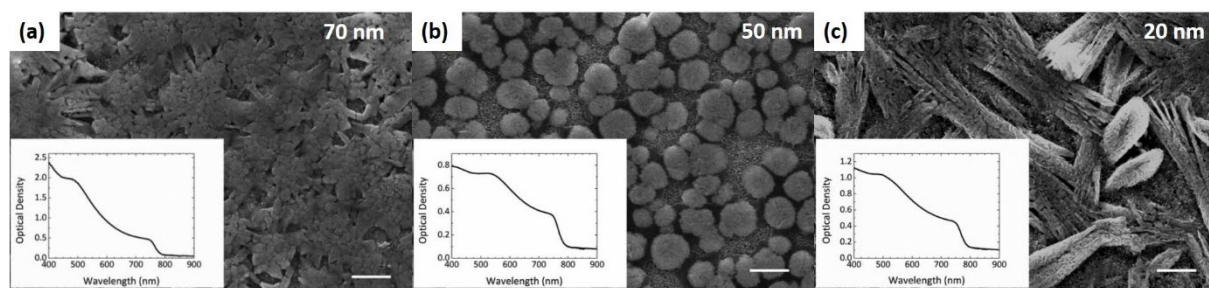


Fig. 1. 16: SEM micrographs of $\text{MAPbI}_{3-x}\text{Cl}_x$ thin films on ZnO nanoparticles with diameters of (a) 70 nm, (b) 50 nm and (c) 20 nm Scale bar: 10 μm [1.49]

1.6.2 Spin-Coating of $\text{MAPbI}_{3-x}\text{Cl}_x$ Thin Films onto ZnO Nanowire Surfaces

Numerous publications are available on two-step spin-coating of traditional, single-halide MAPbI_3 perovskites onto ZnO nanowire or nanorod substrates. For example, Bi *et al.* [1.50] deposited MAPbI_3 via two-step spin-coating onto ZnO nanorods arrays and achieved solar cell efficiencies of up to 5%. This research was improved on by Dong *et al.* [1.51], who incorporated another aluminium-doped ZnO layer on top of the ZnO NW array, prior to MAPbI_3 deposition; an overall PV efficiency of 10.07% was achieved. The efficiency of ZnO based MAPbI_3 solar cells was further increased to 11.13% by Son *et al.* [1.52], whereas in 2015, Mahmood *et al.* [1.53] developed ZnO NW-based devices with 16.19% efficiency. This was achieved by coating the nanowire arrays with a thin polymer layer prior to perovskite deposition. Although promising device efficiencies were obtained, these studies did not address the stability issue experienced by traditional MAPbI_3 perovskites and subsequently, the devices reported did not maintain their efficiencies beyond one week. As already stated, partial substitution of the iodine halide in MAPbI_3 with Cl leads to a more air-stable perovskite. However, research aiming to further solve the instability issue, also make use of surface passivation of the ZnO layer [1.54] and capping of the perovskite by introducing a triple-cation perovskite structure [1.55]; solar cell efficiencies of 21.1% and 18.9%, respectively. Although these approaches have only been applied to ZnO nanoparticle-based thin films, these findings do show promising stabilised ZnO/perovskite interfaces are possible.

1.7 Research Gaps

Yang *et al.* [1.56] found that the ZnO surface allows for proton transfer at the ZnO/CH₃NH₃PbI₃ interface that leads to degradation of the perovskite structure [1.56]. It is also found that the low temperature used during spin-coating of the ZnO nanoparticle films causes the attachment of hydroxide and acetate surface groups, which causes reaction between the methyl ammonium iodide (MAI) and ZnO which accelerates under moisture in ambient air, also causing poor stability of perovskite [1.57].

Based on these findings and the strategies used to improve the perovskite layer when using ZnO as the electron transport layer in photovoltaics (as discussed in Chapter 1.6.2), the following research areas require further investigation, with no publications found on this topic in literature:

- The use of doped ZnO nanowire arrays as substrates for mixed-halide MAPbI_{3-x}Cl_x deposition.
- One-step spin-coating of air-stable MAPbI_{3-x}Cl_x thin films onto ZnO NW arrays, doped or undoped, and investigating the mixed-halide conversion and stability on the ZnO NW array surface.

1.8 Aims and Objectives, Thesis Outline

The following aims and objectives will allow the study to address the research gaps as identified in Chapter 1.7:

Aim 1: Development of a ZnO NW array synthesis strategy that yields repeatable, consistent nanowire structures with controllable dimensions and known doping concentration.

Objectives:

- ZnO NW arrays grown on aluminium (Al) doped ZnO (AZO) substrates offer the most direct pathway for ready-made Al doped ZnO nanowires. Various publications are

available on the hydrothermal synthesis of these structures [1.58 – 1.60]. The first objective, as such, will be to find a hydrothermal synthesis procedure that is simple and cost-effective, yet delivers repeatable results. The specific experimental designs and procedures will be discussed in Chapter 2.

- Relate the physical properties (e.g. diameter, length and packing density) of the hydrothermally synthesised nanowire structures to the experimental parameters used. High-resolution electron microscopy imaging, as discussed in Chapter 4, will be used during this phase of the study.
- Investigate the presence of Al in the ZnO nanowire structure; a combination of energy dispersive x-ray spectroscopy (EDS) and x-ray photoelectron spectroscopy (XPS) will be used to probe the doping.

Aim 2: Understanding the perovskite conversion dynamics using spin-coating deposition of $\text{MAPbI}_{3-x}\text{Cl}_x$ precursors onto Al-doped ZnO NW arrays

Objectives:

- Grow $\text{MAPbI}_{3-x}\text{Cl}_x$ perovskites by spin-coating air stable precursor ink onto AZO and ZnO NW arrays to compare the resultant perovskite morphology.
- Investigate the perovskite conversion process on ZnO NWs by changing the spin-coating conditions: spin-rate, spin-coating duration, substrate temperature and calcination temperature.
- Study the resultant perovskite morphology, I:Cl ratio and crystal structure of the perovskite using electron microscopy and x-ray diffraction

The thesis outline will be as follows:

Chapter One – A summary was presented on the South African energy mix and the role modern perovskite photovoltaics may play in alleviating the energy crisis experienced by the country. Although promising, the lack of long-term stability of the perovskite material was highlighted in

the chapter, and introduced the idea of using one-dimensional ZnO nanowires for the growth of stable perovskites. This is an area of research not reported in literature.

Chapter Two will discuss the ZnO crystal structure and formation during hydrothermal synthesis. The chapter will also present the growth model of ZnO nanowires when synthesised on a substrate with matching crystal structure and will conclude by summarising the methodology and experimental procedure followed to synthesise the nanowire arrays on AZO substrates.

In **Chapter Three**, the basics of the MAPbX₃ perovskite derivatives will be discussed along with the thin film formation during spin-coating onto a substrate. Focus will be given to the growth models during spin-coating and the role that Cl ions play in improving the air stability of the MAPbX₃ perovskite structure. The chapter will conclude by summarising the spin-coating procedure followed to deposit the MAPbI_{3-x}Cl_x thin films onto the ZnO NW arrays.

Chapter Four will summarise the characterisation techniques used to analyse the samples produced throughout this study. These include scanning (SEM) and transmission electron microscopy (TEM), x-ray diffraction (XRD), ultraviolet-visible (UV-Vis) spectroscopy and x-ray photoelectron emission spectroscopy (XPS).

Chapter Five will present the results obtained from the experimental procedures and characterisation techniques as well as the discussions thereof, whereas **Chapter Six** will summarise the major findings and future research.

References

- [1.1] K. Ratshomo and R. Nembahe, "The South African Energy Sector Report 2019", Department of Energy, South African Government. Accessed on 11 Nov 2021, available from <http://www.energy.gov.za> ISBN: 978-1-920435-17-2
- [1.2] H.R. Bohlmann, J. M. Horridge, R. Inglesi-Lotz, E. L. Roos and L. Stander, "Regional Employment and Economic Growth Effects of South Africa's Transition to Low-Carbon Energy Supply Mix", *Energy Policy* 128 (2019) 830–837, doi: <https://doi.org/10.1016/j.enpol.2019.01.065>
- [1.3] O. M. Akinbami, S. R. Oke and M. O. Bodunrin, "The State of Renewable Energy Development in South Africa: An Overview", *Alexandria Engineering Journal* 60 (2021) 5077 – 5093, doi: <https://doi.org/10.1016/j.aej.2021.03.065>
- [1.4] I. M. Mintzer, "Energy, Greenhouse Gases and Climate Change", *Annual Review of Energy* 15 (1990) 513 – 550, doi: <https://doi.org/10.1146/annurev.eg.15.110190.002501>
- [1.5] K. Handayani, Y. Krozer and T. Filatova, "From Fossil Fuels to Renewables: An Analysis of Long-Term Scenarios Considering Technological Learning", *Energy Policy* 127 (2019) 134 – 146, doi: <https://doi.org/10.1016/j.enpol.2018.11.045>
- [1.6] W. G. J. H. M. van Sark and V. Fthenakis, "Introduction to Photovoltaic Technology", *Comprehensive Renewable Energy* 2nd Ed, 1 (2022) Pages 1-7, doi: <https://doi.org/10.1016/B978-0-12-819727-1.00134-5>
- [1.7] C. D. Rodríguez Gallegos and M. S. Alvarez-Alvarado, "Analysis of the Stationary and Transient Behavior of a Photovoltaic Solar Array: Modeling and Simulation", *International Journal of Computer Applications* (0975 – 8887) 127 (2015) 26 – 33, doi: <https://doi.org/10.5120/ijca2015906374>
- [1.8] E. Inshakova, A. Inshakova and A. Goncharov, "Engineered Nanomaterials for Energy Sector: Market Trends, Modern Applications and Future Prospects", *IOP Conf. Ser.: Mater. Sci. Eng.* 971 (2021) 032031, doi: <https://doi.org/10.1088/1757-899X/971/3/032031>
- [1.9] R. A. Messenger and J. Ventre, (2003) "Photovoltaic Systems Engineering 2nd Ed", CRC Press Taylor and Francis, Boca Raton, Florida USA

- [1.10] Minhaz Abedin, (2015) *"A Self-Adjusting Lin-Log Active Pixel for Wide Dynamic Range CMOS Image Sensor"*, BSc (Engineering) Thesis, Department of Electrical and Electronic Engineering, Chittagong University of Engineering and Technology, Chittagong Bangladesh, doi: <https://doi.org/10.13140/RG.2.1.3871.8965>
- [1.11] T. Isik, (2015) *"Solar Cells Review"*, MSC (Physics) Thesis, Department of Physics, Usik University, Istanbul Turkey, doi: <https://doi.org/10.13140/RG.2.1.4298.6404>
- [1.12] D. Velauthapillai, (2017) *"New Generation of Solar Cell Technologies"*, Seminar Presentation: Emerging Technologies and their Impact on the Society, 9th March 2017, Bergen Energy Labs, University of Bergen Norway: https://www.uib.no/sites/w3.uib.no/files/attachments/emerging_solar_cell_technologies_09_03_short.pdf
- [1.13] B. O'Regan and M. Grätzel, *"A Low Cost, High Efficiency Solar Cell based on Dye Sensitized Colloidal TiO₂ Films"*, Nature 353 (1991) pp 737 – 740, doi: <https://doi.org/10.1038/353737a>
- [1.14] J. C. Bernede, *"Organic Photovoltaic Cells: History, Principle and Techniques"*, J. Chil. Chem. Soc. 53 (2008) 53 1549 – 1564, doi: <http://dx.doi.org/10.4067/S0717-97072008000300001>
- [1.15] A. Kojima, K. Teshima, R. Yaegashi, T. Miyasaka and Y. Shirai, *"Novel Photovoltaic Solar Cell Sensitized by Lead-Halide Compounds(II)"*, J. Soc. Photogr. Imaging Jpn. 69 (2006) 28 – 29, doi: <https://doi.org/10.1149/ma2007-02/8/352>
- [1.16] Y. Ren, D. Zhang, J. Suo, Y. Cao, F. T. Eickemeyer, N. Vlachopoulos, S. M. Zakeeruddin, A. Hagfeldt and M. Grätzel, *"Hydroxamic Acid Pre-adsorption Raises the Efficiency of Co-sensitized Solar Cells"*, Nature 613 (2023) 60 – 65; doi: <https://doi.org/10.1038/s41586-022-05460-z>
- [1.17] T. Kietzke, *"Recent Advances in Organic Solar Cells"*, Advances in Opto-Electronics (2007), 040285, doi: <https://doi.org/10.1155/2007/40285>
- [1.18] Y. G. Bi, J. Feng, J. H. Ji, Y. S. Yi, Y. F. Li, Y. F. Liu, *et al.* *"Nanostructures Induced Light Harvesting Enhancement in Organic Photovoltaics"*, Nanophotonics 7 (2017) 371 – 391, doi: <https://doi.org/10.1515/nanoph-2017-0060>

- [1.19] W. Qi, "Nanoscopic Thermodynamics", *Acc. Chem. Res.* 49 (2016) 1587 – 1595, doi: <https://doi.org/10.1021/acs.accounts.6b00205>
- [1.20] M. L. Petrus, J. Schlipf, C. Li, T. P. Gujar, N. Giesbrecht, P. Müller-Buschbaum, M. Thelakkat, T. Bein, S. Hüttner and P. Docampo, "Capturing the Sun: A Review of the Challenges and Perspectives of Perovskite Solar Cells", *Adv. Energy Mater.* 7 (2017) 1700264, doi: <https://doi.org/10.1002/aenm.201700264>
- [1.21] M. Younas, T. A. Kandiel, A. Rinaldi, Q. Peng, A. A. Al-Saadi, "Ambient-Environment Processed Perovskite Solar Cells: A Review", *Materials Today Physics* 21 (2021) 100557, doi: <https://doi.org/10.1016/j.mtphys.2021.100557>
- [1.22] H. Min, D. Y. Lee, J. Kim, *et al.*. "Perovskite Solar Cells with Atomically Coherent Interlayers on SnO₂ Electrodes", *Nature* 598 (2021) 444 – 450, doi: <https://doi.org/10.1038/s41586-021-03964-8>
- [1.23] V. La Ferrara *et al.*, "ZnO Nanorods/AZO Photoanode for Perovskite Solar Cells Fabricated in Ambient Air", *Mater. Res. Express* 4 (2017) 085025, doi: <https://doi.org/10.1088/2053-1591/aa7fcd>
- [1.24] J. Sun, N. Li, L. Dong, X. Niu, M. Zhao, Z. Xu, H. Zhou, C. Shan and C. Pan, "Interfacial-Engineering Enhanced Performance and Stability of ZnO Nanowire Based Perovskite Solar Cells", *Nanotechnology* 32 (2021) 475204, doi: <https://doi.org/10.1088/1361-6528/abdbeb>
- [1.25] O. Madelung, (2003) "Semiconductors: Data Handbook", Springer, Berlin Germany, doi: <https://doi.org/10.1007/978-3-642-18865-7>
- [1.26] G. S. Wu, T. Xie, X. Y. Yuan, Y. Li, L. Yang, Y. H. Xiao and L. D. Zhang, "Controlled Synthesis of ZnO Nanowires or Nanotubes via Sol – Gel Template Process", *Solid State Communications* 134 (2005) 485 – 489, doi: <https://doi.org/10.1016/j.ssc.2005.02.015>
- [1.27] Y. Zhao, C. Li, M. Chen, X. Yu, Y. Chang, A. Chen, H. Zhu and Z. Tang, "Growth of Aligned ZnO Nanowires via Modified Atmospheric Pressure Chemical Vapor Deposition", *Physics Letters A* 380 (2016) 3993-3997, doi: <https://doi.org/10.1016/j.physleta.2016.06.030>

- [1.28] S. C. Lyu, Y. Zhang, C. J. Lee, H. Ruh and H. J. Lee, "Low-Temperature Growth of ZnO Nanowire Array by a Simple Physical Vapor-Deposition Method", *Chem. Mater.* 15 (2003) 3294 – 3299, doi: <https://doi.org/10.1021/cm020465j>
- [1.29] T. Marimuthu, N. Anandhan and R. Thangamuthu, "Electrochemical Synthesis of One-Dimensional ZnO Nanostructures on ZnO seed layer for DSSC Applications", *Applied Surface Science* 428 (2018) 385 – 394, doi: <https://doi.org/10.1016/j.apsusc.2017.09.116>
- [1.30] H. Zhitao, L. Sisi, C. Jinkui and C. Yong, "Controlled Growth of Well-Aligned ZnO Nanowire Arrays using the Improved Hydrothermal Method", *Journal of Semiconductors* 34 (2013) 063002, doi: <https://doi.org/10.1088/1674-4926/34/6/063002>
- [1.31] A. Galdámez-Martínez, G. Santana, F. Güell, P. R. Martínez-Alanis and A. Dutt, "Photoluminescence of ZnO Nanowires: A Review", *Nanomaterials* 10 (2020) 857, doi: <https://doi.org/10.3390/nano10050857>
- [1.32] T. Tasnim Ava, A. Al Mamun, S. Marsillac and G. Namkoong, "A Review: Thermal Stability of Methylammonium Lead Halide Based Perovskite Solar Cells", *Appl. Sci.* 9 (2019) 188, doi: <https://doi.org/10.3390/app9010188>
- [1.33] H.-S. Kim, J.-Y. Seo and N.-G. Park, "Material and Device Stability in Perovskite Solar Cells", *ChemSusChem* 9 (2016) 2528 – 2540; doi: <https://dx.doi.org/10.1002/cssc.201600915>
- [1.34] T. Zhu, Y. Yang and X. Gong, "Recent Advancements and Challenges for Low-Toxicity Perovskite Materials", *ACS Appl. Mater. Interfaces* 12 (2020) 26776 – 26811, doi: <https://dx.doi.org/10.1021/acsmi.0c02575>
- [1.35] J. Yang, B. D. Siempelkamp, D. Liu and T. L. Kelly, "Investigation of $\text{CH}_3\text{NH}_3\text{PbI}_3$ Degradation Rates and Mechanisms in Controlled Humidity Environments Using in Situ Techniques", *ACS Nano* 9 (2015) 1955 – 1963, doi: <https://doi.org/10.1021/nn506864k>
- [1.36] A. M. A. Leguy, Y. Hu, M. Campoy-Quiles, M. I. Alonso, L. J. Weber, P. Azarhoosh, *et al.*, "Reversible Hydration of $\text{CH}_3\text{NH}_3\text{PbI}_3$ in Films, Single Crystals, and Solar Cells" *Chem. Mater.* 27 (2015) 3397 – 3407, doi: <https://doi.org/10.1021/acs.chemmater.5b00660>
- [1.37] G. Niu, X. Guo and L. Wang, "Review of Recent Progress in Chemical Stability of Perovskite Solar Cells", *J. Mater. Chem. A* 3 (2015) 8970 – 8980, doi: <https://doi.org/10.1039/C4TA04994B>

- [1.38] M.I. Asghar, J. Zhang, H. Wang and P.D. Lunda, "Device stability of perovskite solar cells – A review", *Renewable and Sustainable Energy Reviews* 77 (2017) 131–146; doi: <http://dx.doi.org/10.1016/j.rser.2017.04.003>
- [1.39] J. H. Noh, S. H. Im, J. H. Heo, T. N. Mandal and S. I. Seok, "Chemical Management for Colorful, Efficient, and Stable Inorganic–Organic Hybrid Nanostructured Solar Cells", *Nano Lett.* 13 (2013) 1764 – 1769; doi: <https://doi.org/10.1021/nl400349b>
- [1.40] B. Philippe, B.-W. Park, R. Lindblad, J. Oscarsson, S. Ahmadi, E. M. J. Johansson and H. Rensmo, "Chemical and Electronic Structure Characterization of Lead Halide Perovskites and Stability Behavior under Different Exposures - Photoelectron Spectroscopy Investigation" *Chem. Mater.* 27 (2015) 1720 – 1731; <http://dx.doi.org/10.1021/acs.chemmater.5b00348>
- [1.41] R. K. Misra, S. Aharon, B. Li, D. Mogilyansky, I. Visoly-Fisher, L. Etgar and E. A. Katz, "Temperature- and Component-Dependent Degradation of Perovskite Photovoltaic Materials under Concentrated Sunlight", *J. Phys. Chem. Lett.* 6 (2015) 326 – 330; doi: <https://doi.org/10.1021/jz502642b>
- [1.42] R. Ruess, F. Benfer, F. Bocher, M. Stumpp and D. Schlettwein, "Stabilization of Organic–Inorganic Perovskite Layers by Partial Substitution of Iodide by Bromide in Methylammonium Lead Iodide", *Chem. Phys. Chem.* 17 (2016) 1505 – 1511; doi: <https://doi.org/10.1002/cphc.201501168>
- [1.43] E. Mosconi, J. M. Azpiroz and F. de Angelis, "Ab Initio Molecular Dynamics Simulations of Methylammonium Lead Iodide Perovskite Degradation by Water", *Chem. Mater.* 27 (2015) 4885 – 4892; doi: <https://doi.org/10.1021/acs.chemmater.5b01991>
- [1.44] S. D. Stranks, G. E. Eperon, G. Grancini et al., "Electron-Hole Diffusion Lengths Exceeding 1 micrometer in an Organometal-trihalide Perovskite Absorber," *Science* 342 (2013) 341 – 344; doi: <https://doi.org/10.1126/science.1243982>
- [1.45] P. Docampo, F. C. Hanusch, S. D. Stranks et al., "Solution Deposition-Conversion for Planar Heterojunction Mixed Halide Perovskite Solar Cells," *Advanced Energy Materials* 4 (2014) 1400355; doi: <https://doi.org/10.1002/aenm.201400355>

- [1.46] S. L. Hamukwaya, H. Hao, Z. Zhao, J. Dong, T. Zhong, J. Xing, L. Hao and M. M. Mashingaidze, "A Review of Recent Developments in Preparation Methods for Large-Area Perovskite Solar Cells", *Coatings* 12 (2022) 252; doi: <https://doi.org/10.3390/coatings12020252>
- [1.47] Y. Xu, L. Zhu, J. Shi, S. Lv, *et al.*, "Efficient Hybrid Mesoscopic Solar Cells with Morphology-Controlled $\text{CH}_3\text{NH}_3\text{PbI}_{3-x}\text{Cl}_x$ Derived from Two-Step Spin Coating Method", *ACS Appl. Mater. Interfaces* 7 (2015) 2242 – 2248; doi: <https://doi.org/10.1021/am5057807>
- [1.48] D. Chen, X. Zou, H. Yang, N. Zhang, W. Jin, X. Bai and Y. Yang, "Effect of Annealing Process on $\text{CH}_3\text{NH}_3\text{PbI}_{3-x}\text{Cl}_x$ Film Morphology of Planar Heterojunction Perovskite Solar Cells with Optimal Compact TiO_2 Layer", *International Journal of Photoenergy* (2017) 7190801; doi: <https://doi.org/10.1155/2017/7190801>
- [1.49] M. De Bastiani, V. D'Innocenzo, S. D. Stranks, H. J. Snaith and A. Petrozza, "Role of the Crystallization Substrate on the Photoluminescence Properties of Organolead Mixed Halides Perovskites", *APL Materials* 2 (2014) 081509; doi: <https://dx.doi.org/10.1063/1.4889845>
- [1.50] D. Bi, G. Boschloo, S. Schwarzmueller, L. Yang, E. M. J. Johansson and A. Hagfeldt, "Efficient and Stable $\text{CH}_3\text{NH}_3\text{PbI}_3$ -sensitized ZnO Nanorod Array Solid-State Solar Cells", *Nanoscale* 5 (2013) 11686; doi: <https://doi.org/10.1039/C3NR01542D>
- [1.51] J. Y. Dong, J. Zhao, J. Shi, H. Wei, J. Xiao, X. Xu, D. Li, Y. Luo and Q. Meng, "Impressive Enhancement on the Cell Performance of ZnO Nanorods-Based Perovskite Solar Cells with Al-doped ZnO Interfacial Modification", *Chem. Commun.*, 50 (2014) 13381; doi: <https://doi.org/10.1039/C4CC04908J>
- [1.52] D.-Y. Son, J.-H. Im, H.-S. Kim and N.-G. Park, "11% Efficient Perovskite Solar Cell Based on ZnO Nanorods: An Effective Charge Collection System", *Phys. Chem. C* 118 (2014) 16567 – 16573; doi: <https://doi.org/10.1021/jp412407j>
- [1.53] K. Mahmood, B. S. Swain and A. Amassian, "16.1% Efficient Hysteresis-Free Mesostructured Perovskite Solar Cells Based on Synergistically Improved ZnO Nanorod Arrays", *Adv. Energy Mater.* 5 (2015) 1500568; doi: <https://doi.org/10.1002/aenm.201500568>

- [1.54] J. Cao, B. H. Wu, R. H. Chen, Y. Y. Q. Wu, Y. Hui, B. W. Mao and N. F. Zheng, "Efficient, Hysteresis-Free, and Stable Perovskite Solar Cells with ZnO as Electron-Transport Layer: Effect of Surface Passivation", *Adv. Mater.* 30 (2018) 1705596; doi: <https://doi.org/10.1002/adma.201705596>
- [1.55] J. X. Song, L. J. Liu, X. F. Wang, G. Chen, W. J. Tian and T. Miyasaka, "Highly Efficient and Stable Low Temperature Processed ZnO Solar Cells with Triple Cation Perovskite Absorber" *J. Mater. Chem. A* 5 (2017) 13439 - 13447; doi: <https://doi.org/10.1039/C7TA03331A>
- [1.56] J. L. Yang, B. D. Siempelkamp, E. Mosconi, F. De Angelis and T. L. Kelly, "Origin of the Thermal Instability in $\text{CH}_3\text{NH}_3\text{PbI}_3$ Thin Films Deposited on ZnO", *Chem. Mater.* 27 (2015) 4229 – 4236; doi: <https://doi.org/10.1021/acs.chemmater.5b01598>
- [1.57] F. Yang, D. W. Kang and Y. S. Kim, "Improved Interface of ZnO/ $\text{CH}_3\text{NH}_3\text{PbI}_3$ by a Dynamic Spin-coating Process for Efficient Perovskite Solar Cells", *RSC Adv.* 7 (2017) 19030 – 19038; doi: <https://doi.org/10.1039/C7RA01869J>
- [1.58] T. F. Chung, L. B. Luo, Z. B. He, Y. H. Leung, I. Shafiq, Z. Q. Yao and S. T. Lee, "Selective Growth of Catalyst-free ZnO Nanowire Arrays on Al:ZnO for Device Application", *Appl. Phys. Lett.* 91 (2007) 233112; doi: <https://doi.org/10.1063/1.2811717>
- [1.59] Z. H. Chen, Y. B. Tang, Y. Liu, G. D. Yuan, W. F. Zhang, J. A. Zapien, I. Bello, W. J. Zhang, C. S. Lee and S. T. Lee, "ZnO Nanowire Arrays Grown on Al:ZnO Buffer Layers and their Enhanced Electron Field Emission", *Journal of Applied Physics* 106 (2009) 064303; doi: <https://doi.org/10.1063/1.3213091>
- [1.60] J. Zhang, W. Que, Q. Jia, X. Ye and Y. Ding, "Controllable Hydrothermal Synthesis of ZnO Nanowires Arrays on Al-doped ZnO Seed Layer and Patterning of ZnO Nanowires Arrays via Surface Modification of Substrate", *Applied Surface Science* 257 (2011) 10134 – 10140; doi: <https://doi.org/10.1016/j.apsusc.2011.06.163>

CHAPTER TWO

Experimental Techniques – Synthesis of ZnO Nanowire Arrays for Perovskite Thin Film Deposition

2.1 Crystal Structure of ZnO

Zinc oxide has been widely studied for its interesting optical and electrical properties, which allows for application in a broad range of devices, as stated in Chapter 1. In this chapter, the physical properties of the ZnO crystal and formation of nanowires will be discussed as these concepts are important to understand prior to their application in any physical device. Three primary crystal systems are found in nature for ZnO, namely cubic rocksalt, cubic zinc blende and the hexagonal Wurtzite structure, as shown in Fig. 2.1. The Wurtzite symmetry is the thermodynamically stable phase at ambient conditions. In this crystal system the oxygen ions are hexagonally closed packed (HCP) and half of the tetrahedral interstices filled with zinc ions, as shown in Fig. 2.1 (c) [2.1].

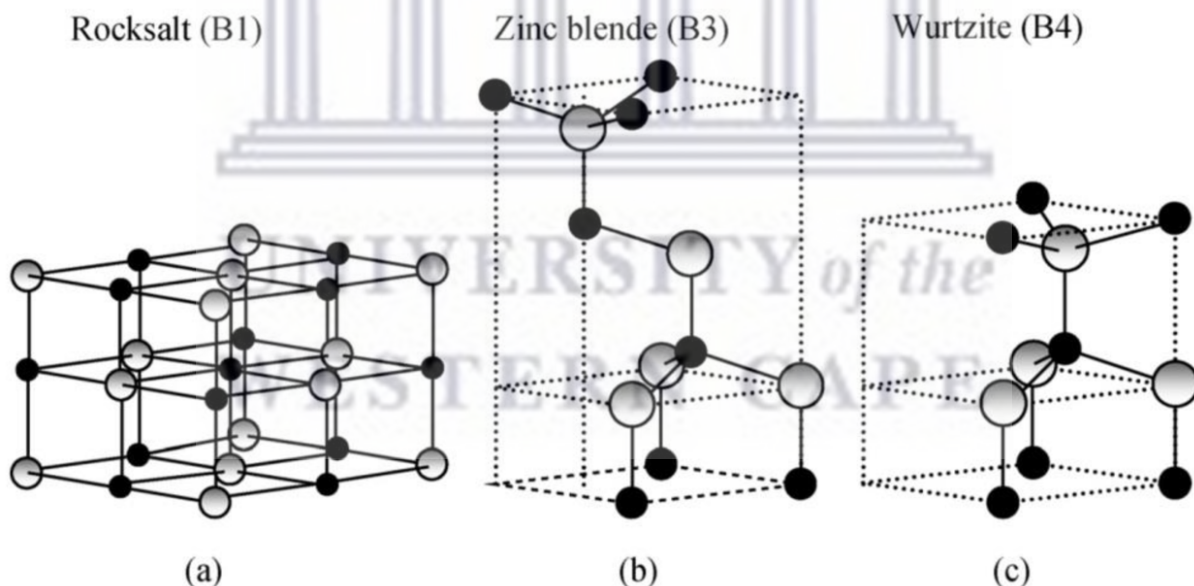


Fig. 2.1: A schematic showing the three ZnO crystals, adopted from [2.1]

The zinc blende structure can be stabilised only by growth on cubic substrates, whereas the rocksalt (NaCl) structure may be produced at very high pressures, as in the case of GaN. In the Wurtzite crystal structure both oxygen and zinc ions are coordinated with four ions of the opposite charge within a hexagonal unit cell with two lattice parameters a and c , where $a = 3.250\text{\AA}$ and $c = 5.206\text{\AA}$. Because ZnO is a two-element compound with different atoms, the c/a ratio for ZnO hcp unit is 1.60, which is slightly less than the ideal value of 1.633. Fig. 2.2 depicts a schematic representation of the Wurtzite unit cell. The structure is made up of two interpenetrating HCP sublattices, each of which is made up of one type of atom that is displaced from the other along the threefold c -axis by $u = \frac{3}{8} = 0.375$ (in an ideal Wurtzite structure) in fractional coordinates. The internal parameter u is defined as the length of the bond parallel to the c -axis (anion-cation bond length or the nearest-neighbour distance) divided by the c lattice parameter. α and β are the bond angles, measured at 109.07° (ideally in Wurtzite crystal) as in shown in Fig. 2.2 [2.1].

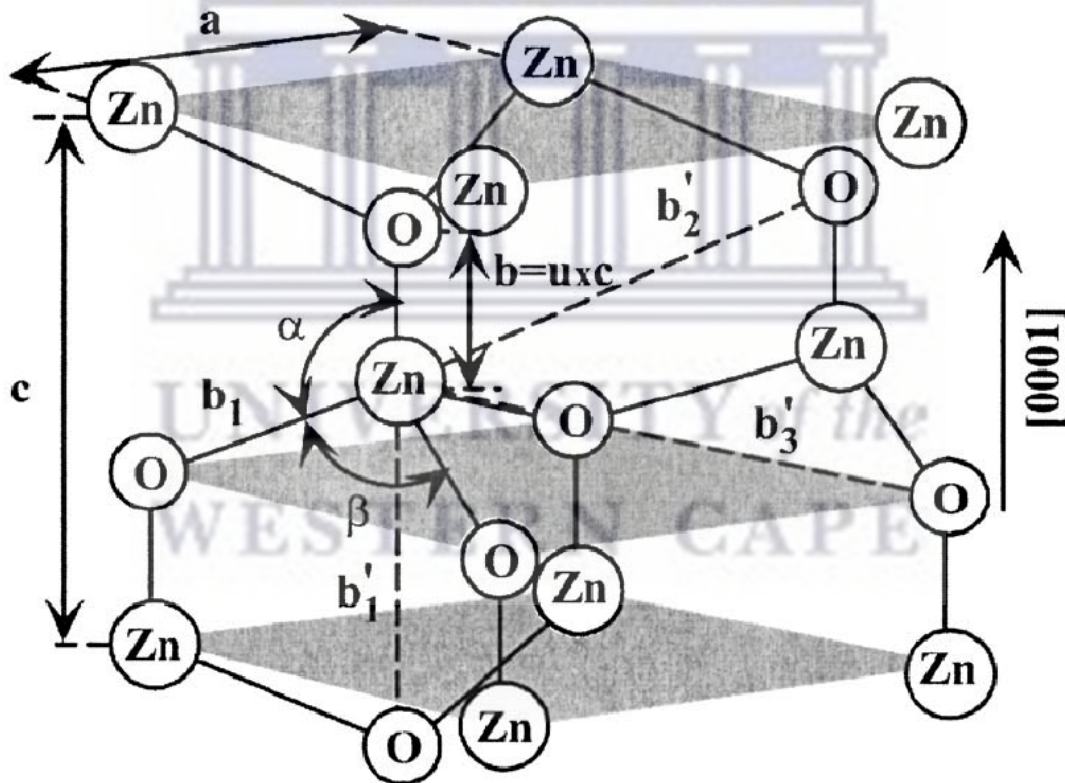


Fig. 2.2: Wurtzite unit cell [2.1]

2.2 Historical Background of the Hydrothermal Synthesis Technique

As mentioned in Chapter 1, the hydrothermal synthesis method stands out from other ZnO fabrication methods due to controlled growth rate, low cost, its simplicity and the ability to produce different nanostructures. As such this method will be exclusively used in this study for the synthesis of 1D ZnO nanowire arrays.

Hydrothermal synthesis can be defined as a heterogenous chemical reaction (solids + liquids) in an aqueous or mineralized solution, under high pressure and temperature. The term "*hydrothermal*" comes from geology. Sir Roderick Murchison (1792-1871) was the first researcher to use the term in explaining the action of water at elevated temperature and pressure, bringing about changes in the earth's crust leading to the formation of numerous rocks and minerals [2.2]. The largest single crystal formed in nature is the beryl crystal (beryllium aluminium silicate with the chemical formula $\text{Be}_3\text{Al}_2\text{Si}_6\text{O}_{18}$) of >100g formed by means of naturally occurring hydrothermal formation. Robert Wilhelm Bunsen is accredited for the work related to hydrothermal synthesis of materials, where he grew barium and strontium carbonate at temperatures above 200 °C and pressure above 100 bars in 1839. In 1845, Karl Emil von Schafhäütl reported the first results of laboratory-based hydrothermal reaction when he observed the formation of small quartz crystals upon transformation of precipitated silicic acid in a steam digester, the precursor of the autoclave. In the industry, hydrothermal processes play a significant role in the concepts of hydrometallurgy for instance, the classic Bayer process for the decomposition of bauxite [2.2, 2.3].

2.3 Chemistry Involved during Hydrothermal Synthesis of ZnO Nanostructures

There are many variations of hydrothermal synthesis reported for the growth of ZnO nanostructures [2.3]. In a typical experiment, the precursor materials (mainly oxides and salts) are dissolved in water (also referred to as the nutrient solution) and placed in an autoclave reactor, which is then placed in a high temperature oven for growth to commence. The autoclave

allows hydrothermal reaction at high pressure and high temperature and is also often referred to as a high-pressure vessel. Two types of autoclaves are found in practice, namely polytetrafluoroethylene (PTFE, or Teflon) lined reactors and polypropiolactone (PPL) lined reactors, as shown in Fig. 2.3. PTFE-lined autoclaves allow for reactions at a maximum of 240 °C, with a safe temperature of 200 °C advised, whereas PPL-lined reactors can tolerate higher operating temperatures, with a safe temperature of 260 °C and maximum temperature of 280 °C stipulated. PTFE-lined autoclaves are almost exclusively used for ZnO growth, as the highest reported synthesis temperature are around 110 °C for most ZnO structures [2.3].

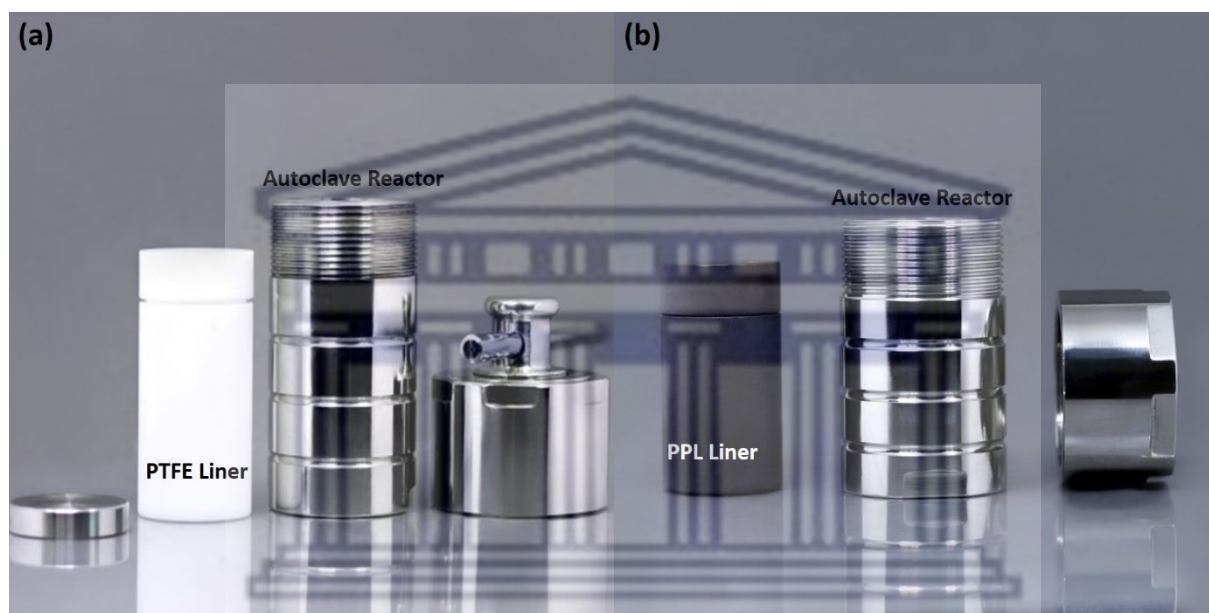
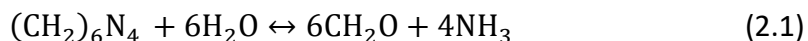
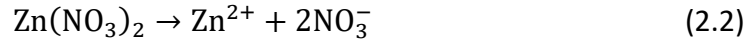


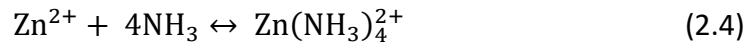
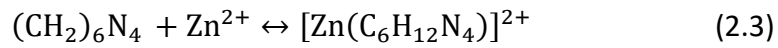
Fig. 2.3: (a) PTFE-lined autoclave and (b) PPL-lined autoclave reactor [<https://shilpent.com>]

The mechanism of the ZnO formation using zinc nitrate hexahydrate ($\text{Zn}(\text{NO}_3)_2 \cdot 6\text{H}_2\text{O}$) and hexamethylenetetramine (HMTA, with chemical formula $\text{C}_6\text{H}_{12}\text{N}_4$) as precursors in an aqueous solution was first proposed by Li *et al.* [2.4]. Ammonia and formaldehyde are formed during the hydrolysis of HMTA (equation 2.1), whereas Zn^{2+} ions are created in solution, during the decomposition of $\text{Zn}(\text{NO}_3)_2 \cdot 6\text{H}_2\text{O}$, as shown in equation 2.2:

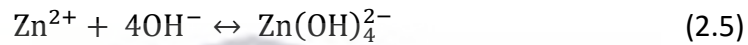




The Zn^{2+} ions created in equation (2.2) may react directly with HMTA or NH_3 ions created in (2.1), leading to the creation of positively charged Zn (II) complexes:



Negatively charged Zn(II) complexes are also formed, according to:



Under specific temperature and pH, the Zn(II) complex may exist as $\text{Zn}(\text{NH}_3)_4^{2+}$ or $\text{Zn}(\text{OH})_4^{2-}$. These reactions are in equilibrium and can be shifted from this equilibrium state by changing the physical parameters, such as temperature, precursor concentration, pH and the growth time. The ZnO crystalline lattice has characteristic polar planes (e.g., (0001), (0002)) that are positively or negatively charged and are closed with zinc (Zn^{2+}) ions or (O^{2-}) ions, respectively. Non-polar planes (e.g., $(10\bar{1}0)$, $(11\bar{2}0)$) which also consist entirely of both types of ions and have an electrically neutral charge are in competition with polar planes during crystal formation and control of either type of plane determines the ZnO shape and dimensions during growth. Polar planes are metastable and are more prone to participate in the growth process and chemical reactions due to their energy state. For example, they can be etched more easily, leading to a tubular nanostructure formation [2.4].

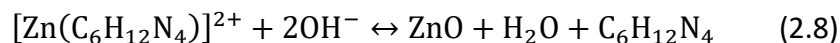
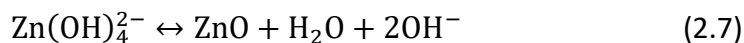
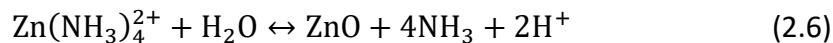
2.4 ZnO Nanowire Array Growth on Substrates

It is possible to grow ZnO NWs on most transparent conducting oxides (TCOs), for use in various semiconductor devices. The three most common TCOs commercially available are tin doped indium oxide (ITO), fluorine doped tin oxide (FTO), and aluminium doped zinc oxide (AZO). When compared to growth on ITO and FTO substrates, ZnO NW grown on AZO substrates has a few advantages. In the first instance, the AZO crystal structure distinguishes it from both ITO and FTO. Like ZnO, AZO has a hexagonal Wurtzite crystal structure. ITO, on the other hand, has a cubic crystal structure, while FTO has a tetragonal crystal structure. Because AZO and ZnO have similar crystal structures, direct epitaxial growth of nanowires on the AZO substrate is possible. ITO and FTO, because of their different crystal structures, do not allow for epitaxial growth and generally a lower degree of alignment and uniformity of the ZnO NWs are produced. As such, an initial ZnO seed layer is first required before growth can commence. These seed layers are typically spin-coated onto the ITO and FTO substrates, followed by heat treatment to induce Wurtzite crystallisation. As a result of the direct epitaxial growth on AZO, the ZnO NWs end up being more uniform and aligned as a result, which is advantageous for a variety of uses, like optoelectronics and energy conversion devices [2.5].

Secondly, the optical and electrical characteristics of TCOs are significantly influenced by surface roughness. In comparison to ITO and FTO films, AZO films are known to have a relatively smoother surface. This is explained by the AZO films' smaller grain size and high uniformity. The smaller grains are caused by the reduced aluminium dopant radius and the faster film growth rate during synthesis. A further benefit of using AZO substrates is that they are generally less expensive than ITO and FTO substrates [2.6]. This makes the option of producing ZnO NWs on a large scale using AZO interesting, and for these reasons, AZO substrates will be exclusively used in this study for growth of ZnO NW arrays.

ZnO NWs growth on a substrate is governed by the condensation of the charged complexes created in reactions (2.3), (2.4) and (2.5). These reactions are in equilibrium and can be controlled by tuning the experimental parameters such as the HMTA and $\text{Zn}(\text{NO}_3)_2 \cdot 6\text{H}_2\text{O}$ concentrations,

pH, and temperature of the nutrient solution in the autoclave reactor. The ZnO crystal formation during condensation/dehydration can be summarised as follows:



The crystallisation reactions (2.6) to (2.8) occur along the c-axis of the unit cell, which is orientated along the nanowire length. The nanowire length is thus formed by a layer-by-layer (i.e. epitaxial) stacking of the Zn^{2+} ions [2.7]. Fig. 2.4 shows a schematic of the nanowire growth process [2.8]. During formation, ZnO aggregation competes with nucleation for particle size and shape, with the HMTA serving as a template for hexagonal ZnO nucleation. The length and diameter of the nanowire array is governed by a competition for ZnO nucleation and Zn^{2+} depletion in the nutrient solution [2.9].

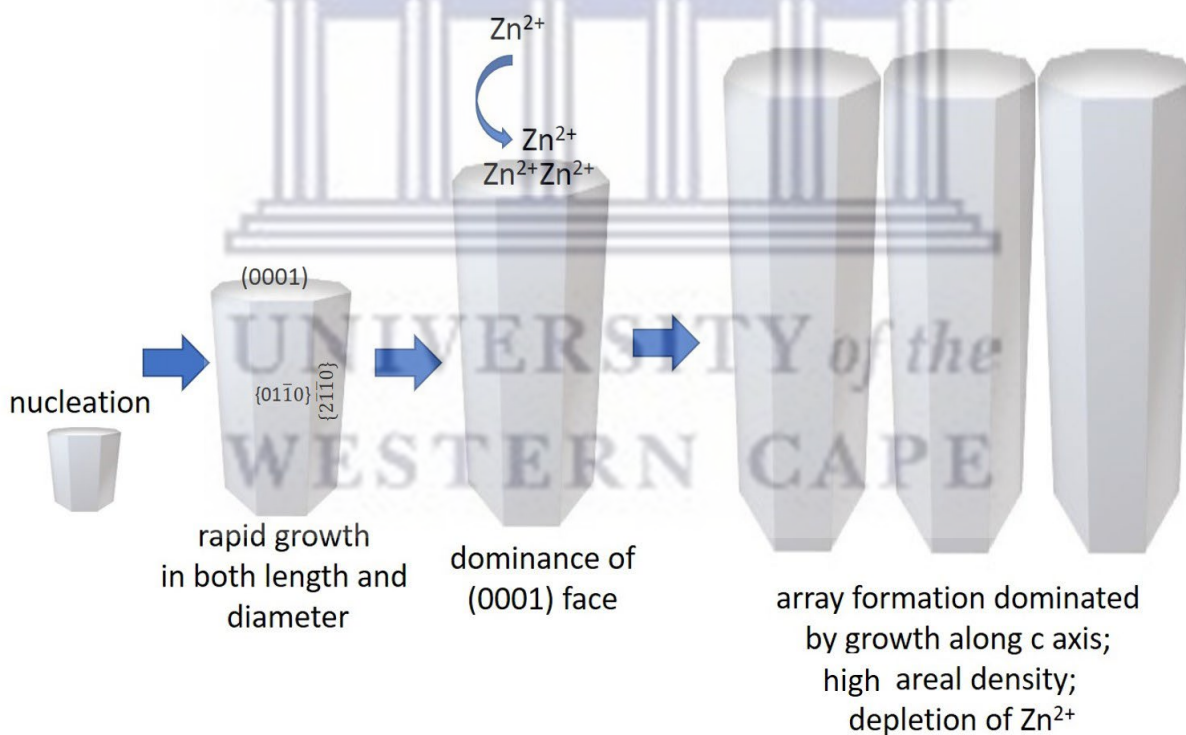


Fig. 2.4: Growth of ZnO nanorod/wires during hydrothermal synthesis [2.8]

The stable ZnO {0001} polar surface has higher kinetic energy compared to $\{2\bar{1}\bar{1}0\}$ and $\{0\bar{1}\bar{1}0\}$, which are the other most commonly observed facets, but non-polar. A growing crystal may form faces or facets on its surface with different polarities depending on the internal structure of the crystal and how it interacts with its surroundings [2.10]. Polar facets are described as the uneven distribution of electrical charge on a surface. On the surface of non-polar facets, the electrical charge is dispersed more uniformly. The ratio of polar to non-polar facets can affect the crystal's overall shape and rate of growth. A crystal can take on a complex, asymmetrical shape when it has both polar and non-polar facets. As an alternative, the crystal may exhibit a more uniform shape with a predominance of either polar or non-polar facets, depending on the solvent and other growth conditions [2.11]. Polar and non-polar facets in crystal growth refer to the different crystal surfaces that may form during the growth process. Non-polar facets do not have a net electrical charge, whereas polar facets do. The arrangement of the atoms on the surface of a crystal surface determines its polarity. The surface is polar if the atoms are arranged in such a way as to create a dipole moment. The surface is non-polar if the arrangement of the atoms does not create a dipole moment [2.12].

Usually, polar facets are more reactive than non-polar facets. This is due to the fact that the surface's net electrical charge can attract ions or molecules from the environment. A number of variables, such as temperature, growth rate, and the presence of impurities, can affect the kind of facet that forms during crystal growth. In general, higher temperatures and slower growth rates favour the formation of polar facets. This is so that the atoms have more time to arrange themselves in a way that creates a dipole moment due to the higher temperature and slower growth rate. The type of facet that forms can also be affected by the presence of impurities. Impurities can alter the surface's regular atomic arrangement, which makes it more challenging for the surface to become polar. After nucleation and incubation, the crystal evolves into a three-dimensional object with well-defined, low-index crystallographic faces. During nanorod/wire growth, the areas of the $\{2\bar{1}\bar{1}0\}$ and $\{0\bar{1}\bar{1}0\}$ facets are maximized because of the lower energy, whereas occasional planar defects and twins are observed parallel to the (0001) plane [2.12].

2.5 ZnO Nanowire Synthesis Procedure

2.5.1 AZO Substrate Preparation and Cleaning

AZO glass sheets (2mm thick, 10 x 10 cm², <10 Ohm/sq) were cut into 1.5 x 2 cm² rectangles using a high precision glass cutter, shown in Fig. 2.5 (a). A total of 10 rectangles were prepared and placed in a substrate rack and submerged in a 2 vol% Hellmanex III solution; the Hellmanex solution was prepared by measuring 2 ml solution and mixing with 100 ml distilled, boiled water. The substrates in the Hellmanex solution were then placed in an ultrasonic bath set at a temperature of 60 °C for 5 minutes. After 5 minutes, the substrate rack containing the AZO rectangles, was removed from the ultrasonicator and the Hellmanex solution discarded. The rack was then rinsed in fresh, boiled distilled water, two times. Once rinsed, the substrates were placed in 100% isopropanol and into the ultrasonic bath at 60 °C for another 5 minutes of cleaning. This was followed by another double rinsing step in fresh boiling water. Finally, the substrates were dried using nitrogen and stored under vacuum. The glass cutter was purchased from Zhuhai Kaivo Optoelectronic Technology©, Zuhai City, China, whereas the substrate rack and Hellmanex III, shown in Fig. 2.5 (b) were bought from Ossila©, Sheffield, United Kingdom. The AZO substrates were bought from MSE Supplies, Tucson USA.

2.5.2 Zinc Nitrate Nutrient Solution Preparation

An initial nutrient solution of Zn(NO₃)₂·6H₂O and HMTA was prepared as follows: 520.6 mg of Zn(NO₃)₂·6H₂O and 245.3 mg of HMTA were weighed off with a microbalance and added to 20 ml of deionised water in a glass beaker. This mixture was stirred for a minimum of 30 minutes using a magnetic stirrer bar and stage at room temperature. If after 30 minutes the solution was still murky, another 30 minutes of stirring was completed, with the aim being to obtain a clear, transparent solution.



Fig. 2.5: (a) Glass cutter (b) substrate rack and Hellmanex III solution used for sample cleaning

2.5.3 ZnO Nanowire Synthesis using Autoclave Hydrothermal Reactor

To commence nanowire synthesis, the clear nutrient solution prepared in Section 2.5.2 was transferred to a Teflon liner. A cleaned AZO substrate (as discussed in 2.5.1) was then placed in the nutrient filled liner at an angle of 45° with the AZO side facing up. The Teflon liner containing the AZO substrate was then transferred to the autoclave reactor and placed in a heating oven, as shown in Fig. 2.6. An initial experimental temperature and time of 90 °C and 3 hours were used for a first synthesis run. After the reaction time elapsed the autoclave was removed from the oven and allowed to cool to room temperature overnight. The next morning, the Teflon liner was taken out of the autoclave and it was noted that the AZO substrate was coated with white precipitates. The substrate was then cleaned by ultrasonic bath cleaning in ethanol for 10 mins followed by sonication with deionised water for another 10 mins. The substrate was then dried using the nitrogen gas, followed by annealing for 10 mins at 350 °C on a hotplate. Post annealing,

a hazy white substrate tinge was obtained, which was stored under vacuum until further processing.

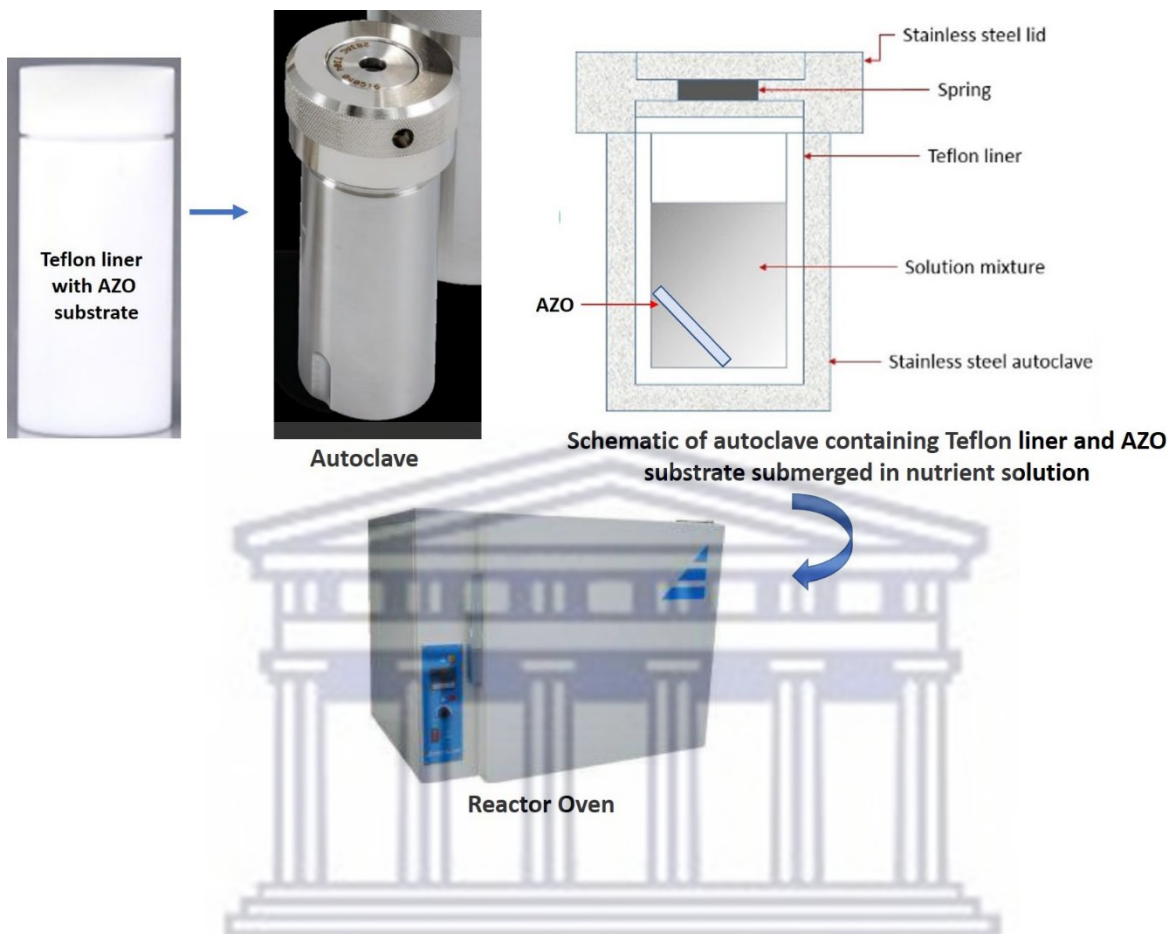


Fig. 2.6: Schematic of the methodology followed during ZnO NW synthesis using the autoclave

UNIVERSITY of the
WESTERN CAPE

2.5.4 ZnO Nanowire Synthesis without Autoclave Reactor

The results of Chapter 5 will show that the nanowire morphology obtained from the autoclave reactor is inconsistent and non-repeatable. This compelled the study to investigate alternative synthesis methods for the growth of the ZnO NW arrays. To this end, a nutrient solution consisting of $\text{Zn}(\text{NO}_3)_2 \cdot 6\text{H}_2\text{O}$, HMTA and polyethyleneimine (PEI) was prepared as follows: 520.6

mg $\text{Zn}(\text{NO}_3)_2 \cdot 6\text{H}_2\text{O}$ and 245.3 mg HMTA were weighed off and dissolved in 25 ml deionised water at 60 °C temperature under magnetic stirring. Once dissolved, 0.0032 ml of PEI was added to the solution and further stirred until a clear solution was obtained. A maximum stirring time of 2 hours and temperature of 60 °C were maintained. Once fully dissolved, the mixture was poured into a Teflon liner, followed by the AZO substrate being placed vertically the liner, submerged in the solution. Finally, the liner was placed in the reactor oven for 3 hours at 90 °C for 3 hours. Fig. 2.7 shows the schematic of the methodology used to synthesise the NWs without the use of an autoclave vessel.

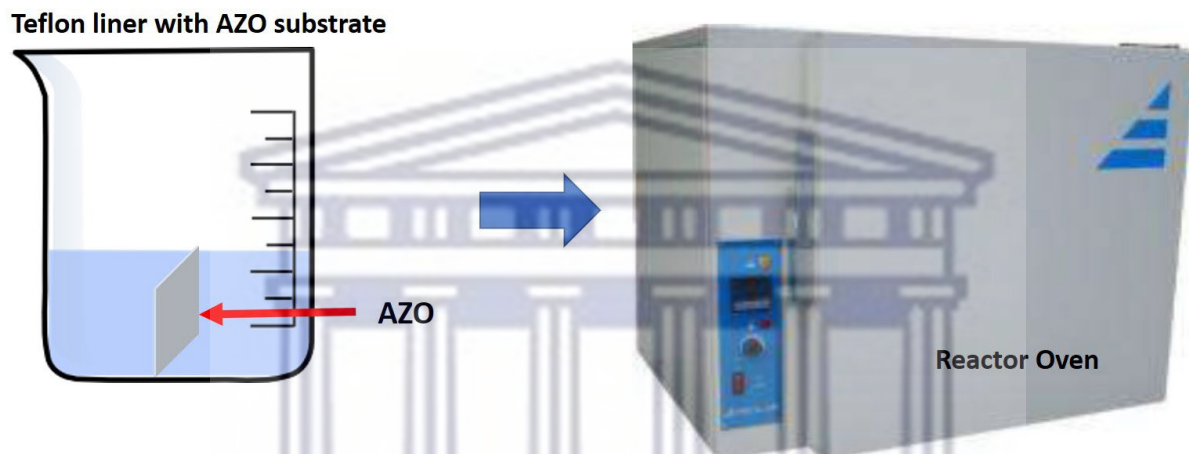


Fig. 2.7: Schematic of the methodology followed during ZnO NW synthesis using the autoclave

After 3 hours of synthesis, the Teflon liner was removed from the oven and the substrate dipped into 15 ml of ethanol, followed by ultra-sonication for 10 mins. After 10 mins, the substrate was transferred to a 20 ml of deionised water and sonicated for 10 mins. After all the cleaning processes, the substrate was dried using nitrogen gas and stored in a clean, dry sample box. The sample box was then vacuum sealed to avoid penetration of oxygen.

Polyethylenimine (PEI) was used during this synthesis method (hereon named chemical bath synthesis, or CB) because it acts as a surfactant, dispersant, and complexing agent to maintain

the surface charge of the particles to prevent clumping or aggregation. Diamines like ethylenediamine and PEI adsorb on the non-polar sidewalls of ZnO NWs to promote axial expansion at the expense of radial growth - this results in thin, long nanowire structures. In contrast, chlorine ions and citrate ions adsorb on the polar, top face of the ZnO crystal to inhibit the axial elongation, while promoting radial growth; this results in thick, short nanorod structures [2.13]. For controlled growth of crystals during CB synthesis, it is crucial that the particles remain suspended in the nutrient solution. As such, due to its ability to stabilise the solution and stop materials from precipitating, PEI is especially useful when an autoclave is not being used. This is crucial because, in the absence of an autoclave, it can be challenging to maintain the high pressure and temperature conditions required for a variety of crystal growth processes. These difficulties may be overcome while maintaining crystals of high quality by using PEI.

2.6 Summary of Experimental Parameters

This section summarises the experimental conditions investigated for nanowire growth during autoclave and non-autoclave (or chemical bath) synthesis.

2.6.1 Experimental Parameters maintained during Autoclave Synthesis

Table 2.1: Effect of the Hydrothermal Synthesis Time on NW Morphology

Sample	Time (hrs)	Temperature (°C)	Zn(NO ₃) ₂ ·6H ₂ O (mg)	HMTA (mg)
NW-AC 1h	1	90	520.6	245.3
NW-AC 3h	3	90	520.6	245.3
NW-AC 8h	8	90	520.6	245.3

Table 2.2: Effect of the Hydrothermal Synthesis Temperature on NW Morphology

Sample	Time (hrs)	Temperature (°C)	Zn(NO ₃) ₂ ·6H ₂ O (mg)	HMTA (mg)
NW-AC 90	3	90	520.6	245.3
NW-AC 100	3	100	520.6	245.3
NW-AC 110	3	110	520.6	245.3

Table 2.3: Effect of Zinc Nitrate-to-HTMA Concentration on NW Morphology

Sample	Time (hrs)	Temperature (°C)	Zn(NO ₃) ₂ ·6H ₂ O (mg)	HMTA (mg)
NW-AC 25M	3	90	185.9	87.6
NW-AC 50M	3	90	371.8	175.2
NW-AC 70M	3	90	520.6	245.3

2.6.2 Experimental Parameters Maintained during Chemical Bath Synthesis

Table 2.4: Effect of the Chemical Bath Synthesis Time on NW Morphology

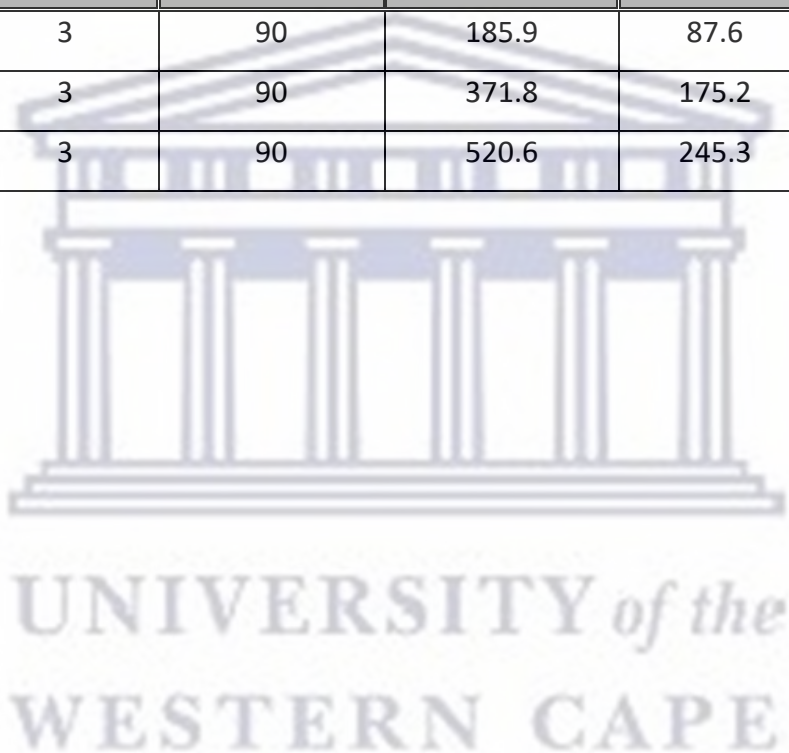
Sample	Time (hrs)	Temperature (°C)	Zn(NO ₃) ₂ ·6H ₂ O (mg)	HMTA (mg)	PEI (mg)
NW-CB 1h	1	90	520.6	245.3	6.5
NW-CB 3h	2	90	520.6	245.3	6.5
NW-CB 8h	3	90	520.6	245.3	6.5

Table 2.5: Effect of the Chemical Bath Temperature on NW Morphology

Sample	Time (hrs)	Temperature (°C)	Zn(NO ₃) ₂ ·6H ₂ O (mg)	HMTA (mg)	PEI (mg)
NW-CB 90	3	90	520.6	245.3	6.5
NW-CB 100	3	100	520.6	245.3	6.5
NW-CB 110	3	110	520.6	245.3	6.5

Table 2.6: Effect of Zinc Nitrate-to-HTMA Concentration on NW Morphology

Sample	Time (hrs)	Temperature (°C)	Zn(NO ₃) ₂ ·6H ₂ O (mg)	HMTA (mg)	PEI (mg)
NW-CB 1-25	3	90	185.9	87.6	6.5
NW-CB 2-50	3	90	371.8	175.2	6.5
NW-CB 3-70	3	90	520.6	245.3	6.5



References

- [2.1] H. Morkoç and U. Özgür, (2009), *“Zinc Oxide: Fundamentals, Materials and Device Technology”*, Wiley United States of America, ISBN: 978-3-527-40813-9
- [2.2] M. Shandilya, R. Rai, and J. Singh, *“Review: Hydrothermal Technology for Smart Materials,”* *Advances in Applied Ceramics* 115 (2016) 354 – 376, doi:<https://10.1080/17436753.2016.1157131>
- [2.3] K. Byrappa and M. Yoshimura, (2012), *“Handbook of Hydrothermal Technology, 2nd Edition”*, Elsevier United Kingdom, ISBN: 9781437778366
- [2.4] Q. Li *et al.*, *“Synthesis and Growth Mechanism of ZnO Rod-Like Nanostructures by a Microwave-assisted Low-Temperature Aqueous Solution Route,”* *Crystal Research and Technology* 49 (2014) 298 – 302, doi: <https://10.1002/crat.201300355>
- [2.5] Y. Zhang, M. K. Ram, E. K. Stefanakos, and D. Y. Goswami, *“Synthesis, Characterization and Applications of ZnO Nanowires,”* *Journal of Nanomaterials* 2012 (2012) 624520, doi: <https://10.1155/2012/624520>
- [2.6] S. Tabassum, E. Yamasue, H. Okumura, and K. N. Ishihara, *“Electrical stability of Al-doped ZnO Transparent Electrode Prepared by Sol-Gel Method,”* *Applied Surface Science* 377 (2016) 355 – 360, doi: <https://10.1016/j.apsusc.2016.03.133>
- [2.7] J. J. Cheng, S. M. Nicaise, S.M., K. K. Berggren and S. Gradečak, *“Dimensional Tailoring of Hydrothermally Grown Zinc Oxide Nanowire Arrays”*, *Nano Lett.* 16 (2016) 753–759, doi: <https://10.1021/acs.nanolett.5b04625>
- [2.8] B. L. Muhammad, Y. A. Jibrin, N. Babakatcha, M. B. Umar, A. A. Gbedako and F. R. Cummings, *“Effect of Synthesis Time on the Structural and Opto-electronic Properties of Hydrothermally grown ZnO Nanowires”*, *Nano Plus: Sci Tech Nanomat*, 4 (2022) 75-85; doi: <https://10.48187/stnanomat.2022.4.011>
- [2.9] M. N. Ali, S. A. Salman, M. O. Dawood, *“The Growth Mechanism of ZnO Nanorods and the Effects of Growth Conditions”* *Nat. Volatiles & Essent. Oils* 8 (2021) 1611-1620
- [2.10] R. Boppella, K. Anjaneyulu, P. Basak and S. V. Manorama, *“Facile Synthesis of Face Oriented ZnO Crystals: Tunable Polar Facets and Shape Induced Enhanced Photocatalytic*

- Performance*", J. Phys. Chem. C 117 (2013), 4597 – 4605; doi: <https://doi.org/10.1021/jp311443s>
- [2.11] E. Debroye, J. Van Loon, H. Yuan, K. P. F. Janssen, Z. Lou, S. Kim, T. Majima, and M. B. J. Roelofs, "Facet-Dependent Photoreduction on Single ZnO Crystals", J. Phys. Chem. Lett. 8 (2017) 340 – 346; doi: <https://doi.org/10.1021/acs.jpcllett.6b02577>
- [2.12] M. Huang, S. Weng, B. Wang, J. Hu, X. Fu and P. Liu, "Various Facet Tunable ZnO Crystals by a Scalable Solvothermal Synthesis and Their Facet-Dependent Photocatalytic Activities", J. Phys. Chem. C 118 (2014) 25434-25440; doi: <https://doi.org/10.1021/jp5072567>
- [2.13] R. Parize, J. D. Garnier, E. Appert, O. Chaix-Pluchery and V. Consonni, "Effects of Polyethylenimine and Its Molecular Weight on the Chemical Bath Deposition of ZnO Nanowires", ACS Omega 3 (2018) 12457-12464; doi: <http://dx.doi.org/10.1021/acsomega.8b01641>



CHAPTER THREE

Experimental Techniques: Mixed Halide MAPbI_{3-x}Cl_x Perovskite Film Synthesis on ZnO Nanowire Arrays

3.1 Introduction

As motivated in Chapter 1, in this study a one-step spin-coating technique will be used to deposit air-stable MAPbI_{3-x}Cl_x precursor solutions onto the ZnO nanowire arrays. In this chapter, the important physics and chemistry involved during crystallisation and film formation of the MAPbI₃ and mixed-halide MAPbI_{3-x}Cl_x structures will be summarised. The very important concept of ion migration in the perovskite layer and the role of chlorine ions in improving the stability of the perovskite will also be presented. The chapter will conclude by summarising the methodology used to synthesise the MAPbI_{3-x}Cl_x layers at different spin-coating conditions onto the different ZnO nanowire arrays.

3.2 The Spin-Coating Technique

Spin-coating is a technique used to prepare thin films by spinning out a precursor solution over the surface of a substrate. During deposition, the coating solution is added onto a spinning surface to allow the centrifugal force to drive the solution towards the edge of the substrate. The solvent rapidly evaporates to produce a uniform layer on the substrate, as shown in Fig. 3.1 [3.1]. Having precise control over the solvent evaporation rate, substrate spin rate and viscosity of the precursor solution is crucial in determining the film thickness and quality. Experimentally, this means that the precursor volume and concentration, substrate rotational speed and spin time must be investigated to obtain an optimum set of parameters for reproducible, high quality films. In some instances, organic additives are added during substrate spinning to adjust the

concentration, viscosity and volatility of the coating solution, thereby producing an ultrathin film on various substrates [3.2].

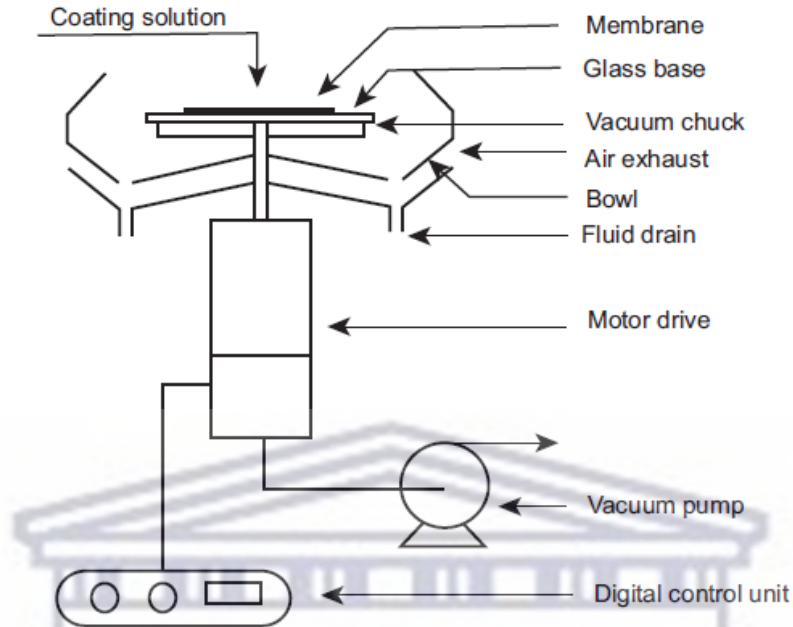


Fig. 3.1: Schematic illustration of a typical spin-coating apparatus [3.1]

Emslie *et al.* [3.3] derived a model for determining the film thickness, h , as a function of certain spin-coating parameters as follows:

$$h = \frac{h_0}{\left(1 + \frac{4\omega^2 h_0^2 t}{3\eta}\right)^{1/2}} \quad (3.1)$$

where h_0 is the initial film thickness, μ the spin rate, and η the viscosity. However, experimentally, this equation was rarely satisfied because the various operating conditions, such as ambient temperature, air-flow and humidity differed from lab to lab. Huang and Chou [3.4] proposed that the shear forces resulting from the viscosity and spinning of the solution mainly determine the film thickness; a less viscous precursor solution would produce a thinner, yet uniform layer.

3.3 MAPbI₃ Thin Film Formation during One-Step Spin-Coating

During MAPbI₃ spin coating, the precursor solution contains PbI₂ and methylammonium iodide (MAI). The choice of solvent is very important, as it must be able to dissolve the precursors and evaporate quickly. Dimethyl formamide (DMF), dimethyl sulfoxide (DMSO), γ -butyrolactone (GBL), or N- N-methyl-2-pyrrolidone (NMP) are commonly used as the main solvent agent as they allow for complete dissolution of PbI₂ and MAI [3.5].

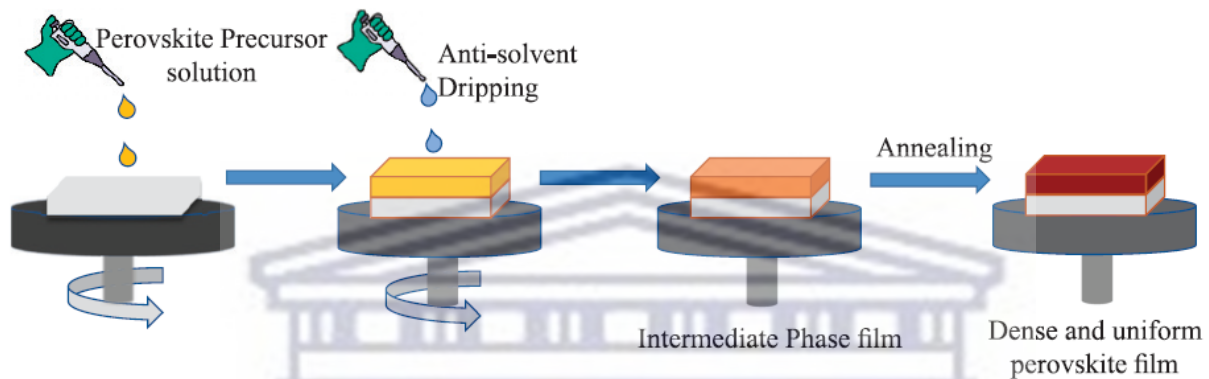


Fig. 3.2: One-step spin-coating process for perovskite thin film deposition [3.5]

The formation of the perovskite layer during one-step spin-coating involves two stages: (a) evaporation of excess solvent in the active layer and (b) crystallisation of the perovskite [3.6]. As shown in Fig. 3.3, this method often results in the formation of pinholes in the perovskite layer, which negatively affects the optoelectronic properties of the solar cell during operation [3.7]. The pin-holes are caused by the incomplete intermixing of the PbI₂ and MAI during the evaporation and intermediate phases (image 3 of Fig. 3.2) [3.7]. The most popular and straightforward means to decrease pin-hole formation, is the addition of a non-dissolving liquid (or so-called anti-solvents) to the precursor solution; this is shown by image 2 of Fig. 3.2 [3.5].

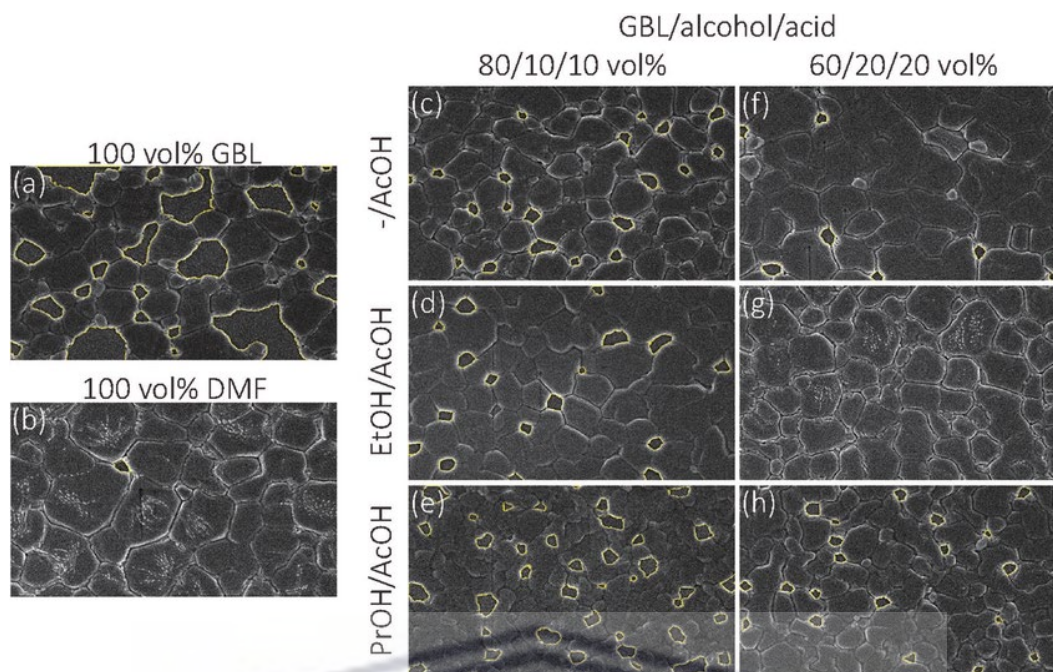


Fig. 3.3: SEM micrographs demonstrating the formation of pin-holes (outlined in yellow) during one-step spin-coating [3.7]

Antisolvent precipitation is a well-known technique for inducing rapid crystallisation of a substance. In Fig. 3.2, the anti-solvent addition is demonstrated. As shown, the perovskite precursor solution is dropped onto the spinning substrate and followed by anti-solvent addition. This results in speedy evaporation of the main solvent, fast nucleation and the formation of a homogeneous, intermediate film (image 3). To obtain the perovskite crystallisation, the substrate is removed from the spin-coater and annealed to obtain a smooth perovskite film with large crystal grains and minimal pin-holes (image 4). For the preparation of high-quality MAPbI_3 layers, anti-solvents such as benzene, toluene, ethanol, methanol, acetonitrile, benzonitrile chloroform, isopropyl alcohol, ethylene glycol, and chlorobenzene have been utilised [3.7 – 3.9]. It must be noted that the anti-solvent step must be done at the correct time during the spin-coating process and in the correct quantity, with a high level of proficiency. Failure to do so may result in uncontrolled crystallisation, which also causes pinholes and higher defect density. Currently, the

anti-solvent is dropped 15 seconds after the precursor spinning step, with chlorobenzene, toluene, and diethyl ether the most commonly used anti-solvents [3.7].

3.4 Fundamentals of Nucleation and Crystal Growth

Crystal growth is influenced by factors such as substrate temperature, solution concentration, solvent and the supersaturated environment. Fig. 3.4 (Top) shows a La Mer diagram in which these factors are correlated with the nucleation and growth processes. To initiate crystallisation, the solution must be supersaturated. Once supersaturation is reached, nucleation occurs, which can be either heterogeneous or homogeneous. Heterogeneous nucleation occurs at preferential nucleation sites on a surface in contact with the liquid, whereas nucleation without preferential sites is known as homogeneous nucleation. Homogeneous nucleation occurs spontaneously and randomly, but requires superheating or supercooling of the solution. Furthermore, compared to heterogeneous nucleation, this type of nucleation also occurs with much more difficulty and in the interior of a solution [3.10].

During perovskite crystallisation, the nucleation is influenced by the substrate temperature and post-spin coating thermal annealing (image 4 of Fig. 3.2). When the substrate temperature is below 100 °C, the perovskite formation may be divided into three steps: (1) *the solution stage*, where the MAI and PbI_2 phases are spin-coated as a wet layer onto the substrate, (2) *transition stage*, during which the wet layer transitions to a solid, film and finally (3) *the transformation stage* where the intermediates transform into a crystalline perovskite film under heat [3.10, 3.11]. Fig. 3.4 (bottom) shows the formation of the perovskite layer during each of these steps. When the substrate temperature is raised between 100 and 180°C, the wet film has enough energy to overcome the activation energy barrier of nucleation and subsequently no intermediate phase (step 2) occurs, leading to direct formation of the perovskite film.

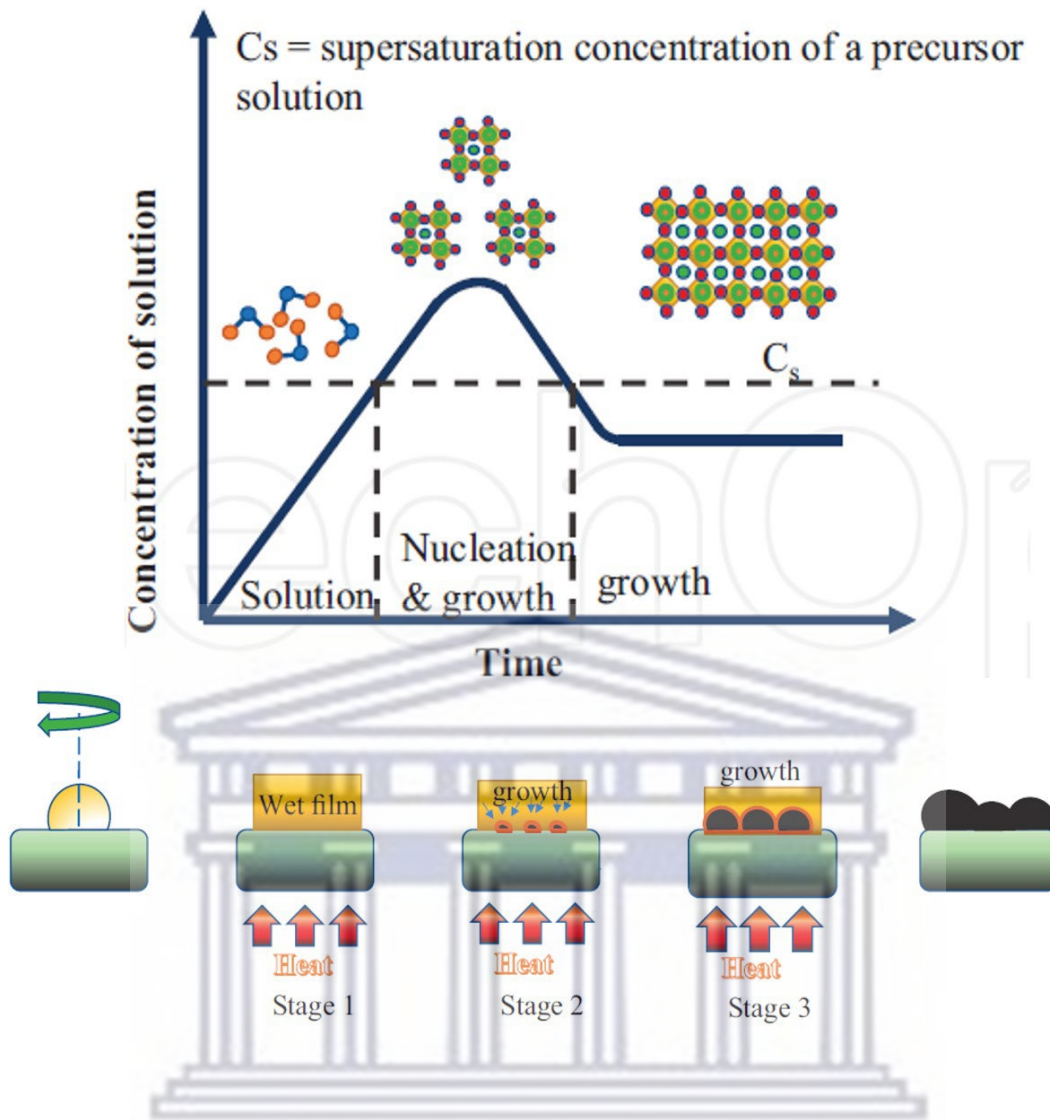


Fig. 3.4: (Top) Lar Mer model for nucleation and growth, (Bottom) Nucleation and growth of the perovskite film at each stage [3.7]

3.5 Morphology of MAPbI₃ and MAPbI_{3-x}Cl_x Thin Films Spin-Coated on ZnO Surfaces

3.5.1 Morphology of MAPbI₃ Spin-Coated on ZnO Thin Films

To achieve high performance perovskite solar cells (PSCs), a uniform layer of ZnO with low defect density is essential. Liu and Kelly [3.12] deposited 300 nm thin layers of MAPbI₃ on 70 nm ZnO thin films by spin coating and obtained PSC efficiencies as high as 15.7% and 10.2% on rigid and flexible substrates, respectively. Fig. 3.5 shows (a) low and (b) high magnification SEM micrographs of the resultant MAPbI₃ films, in which it can be observed that the films are rough with crystal grains ranging broadly between 100 and 1000 nm. These perovskite layers are very different in morphology compared to that grown on TiO₂ layers (Fig. 3.3) and is attributed to the absence of another thin, mesoporous layer of ZnO on top of the 70 nm film.

Apart from the ZnO film thickness, the size of the ZnO nanoparticles also affects perovskite morphology. Zhang *et al.* [3.13] spin-coated MAPbI₃ layers on ZnO thin films with particle sizes of 25, 40 and 50 nm and found that the perovskite morphology changes as shown in Fig. 3.6. The pore filling effect, during which the perovskite layers fills small pores in the ZnO mesoporous layers during the nucleation and intermediate growth phases, explains the difference in perovskite morphology.

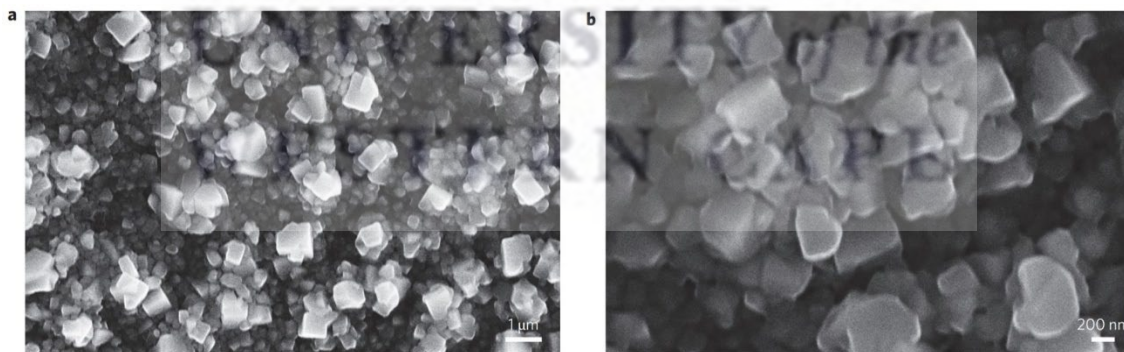


Fig. 3.5: (a) Low-magnification and (b) high-magnification SEM micrograph of MAPbI₃ film spin-coated onto a 70 nm thin layer of ZnO [3.12]

Poor filling of small particle (25 nm) films leads to perovskite layers with small grain sizes and high number of pin-holes, whereas large particle films (50 nm) produce perovskite filling and a film with large grain sizes and low number of pin-holes [3.13].

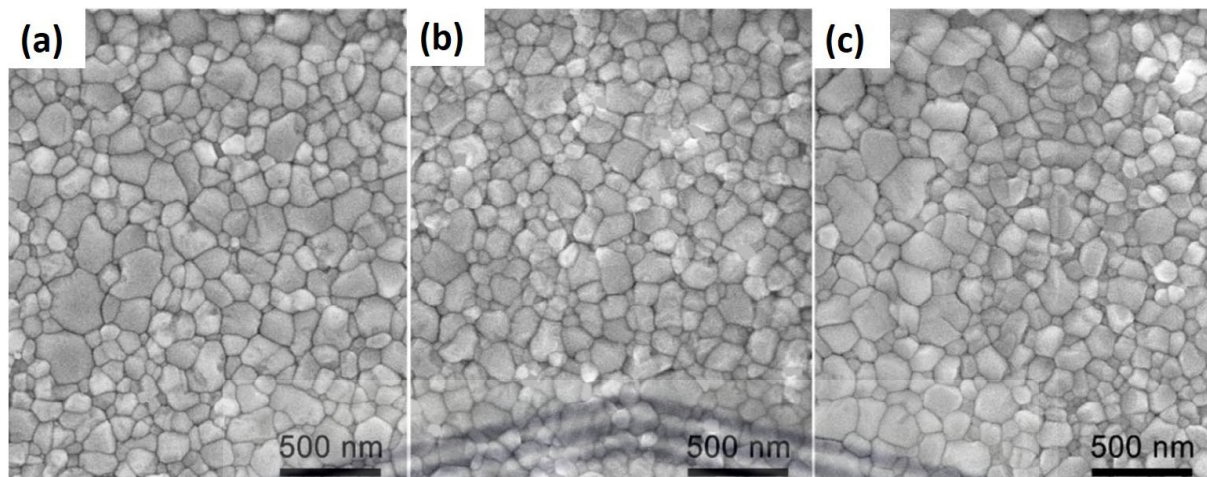


Fig. 3.6: SEM micrographs of the MAPbI₃ films grown on (a) 25, (b) 40 and (c) 50 nm ZnO nanoparticle films [3.13]

3.5.2 Morphology of MAPbI_{3-x}Cl_x Spin-Coated on ZnO Thin Films

The morphology of MAPbI_{3-x}Cl_x thin films grown on ZnO thin films is much different to the morphology of MAPbI₃ shown in Fig 3.5 and 3.6. Bastiani *et al.* [3.14] spin-coated 1000 nm thick ZnO thin films with particle sizes ranging between 20 and 70 nm. They found that the morphology of the mixed-halide perovskite varies significantly with a change in ZnO particle size, as shown in Fig. 3.7. In particular, the group showed that nucleation on 70 nm ZnO NPs gives rise to bridge-connected, condensed domains with micrometre-sized diameters (Fig. 3.7 (a)), whereas deposition on 50 nm particles yields clusters without the bridge connections and lower coverage of the ZnO film (Fig. 3.7 (b)). Fig. 3.7 (c) shows that a completely different morphology is obtained when the ZnO size is further reduced to 20 nm, with fibrous, elongated perovskite structures synthesised.

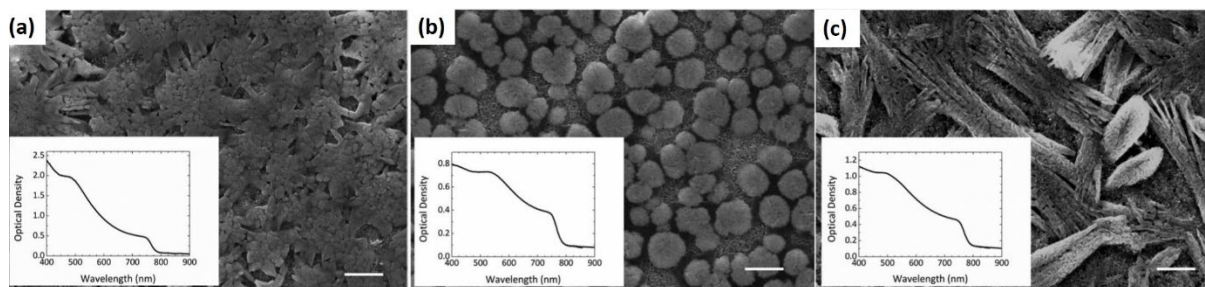


Fig. 3.7: SEM micrographs of $\text{MAPbI}_{3-x}\text{Cl}_x$ thin films on ZnO nanoparticles with diameters of (a) 70 nm, (b) 50 nm and (c) 20 nm Scale bar: 10 μm [3.14]

3.5.3 Morphology of MAPbI_3 and $\text{MAPbI}_{3-x}\text{Cl}_x$ Thin Films Spin-Coated on ZnO Nanowires

After an extensive literature search and review, no publications could be found on one-step spin coating of MAPbI_3 and $\text{MAPbI}_{3-x}\text{Cl}_x$ on ZnO nanowire and nanorod substrates. Instead, a large number of publications report on two-step, sequential spin coating of the MAI and PbI_2 and/or PbCl_2 precursor solutions on the nanowire arrays. Makenali *et al.* [3.15] summarises the major findings in a review article. An example of the morphology of MAPbI_3 grown on ZnO nanowires via two-step spin coating is shown in Fig. 3.8 (a). The results, published by Son *et al.* [3.16], show that some of the nanowires protrude after perovskite deposition, as shown in Fig. 3.8 (b). The protrusion was attributed to voids in the ZnO nanowire film, which cause incomplete pore filling with the perovskite. The fibrous morphology of the perovskite layer shown in Fig 3.8 (b) is similar to that found by Bastiani *et al.*, when reducing the ZnO NP size to 20 nm (Fig. 3.7 (c)).

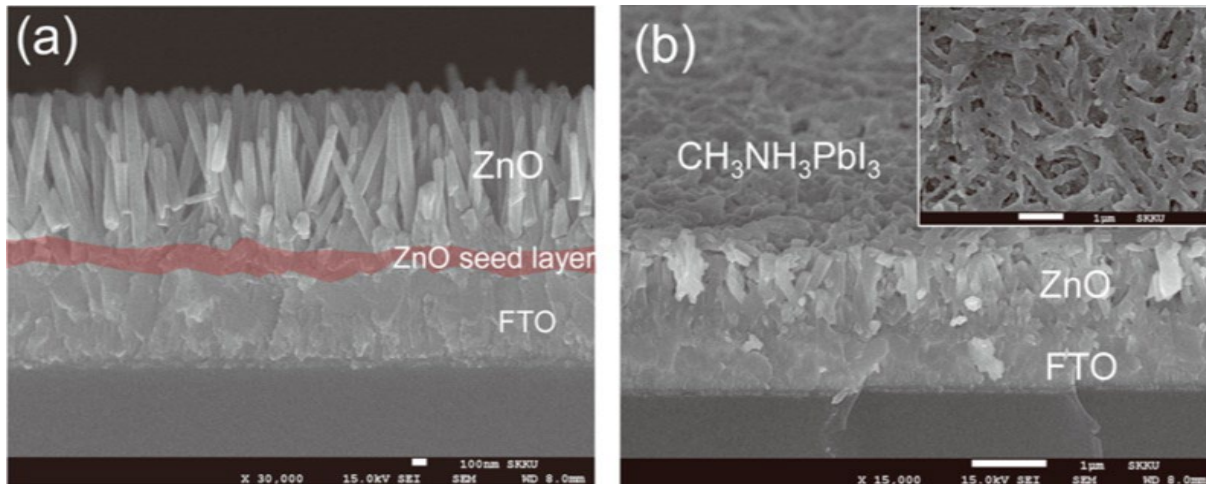


Fig. 3.8: SEM micrographs of (a) ZnO nanowire array and (b) MAPbI₃ thin films grown on ZnO nanowire array via sequential spin-coating [3.16]

Fig. 3.9 shows the morphology of MAPbI_{3-x}Cl_x thin films grown by sequential spin coating on various lengths of ZnO nanorods/nanowires [3.15]. As shown, for NWs with lengths of 320 and 430 nm, the perovskite layer completely covers the surface and a uniform, homogenous film without considerable pores is formed. However, when the length increases to 600 nm and 1.5 μ m, the perovskite film does not fully cover the surface and nanorod protrusion is visible on the surface of perovskite. As such, the NW length may be used as an effective parameter in controlling the coverage of the perovskite film, with shorter NWs allowing for better perovskite uniformity and coverage.

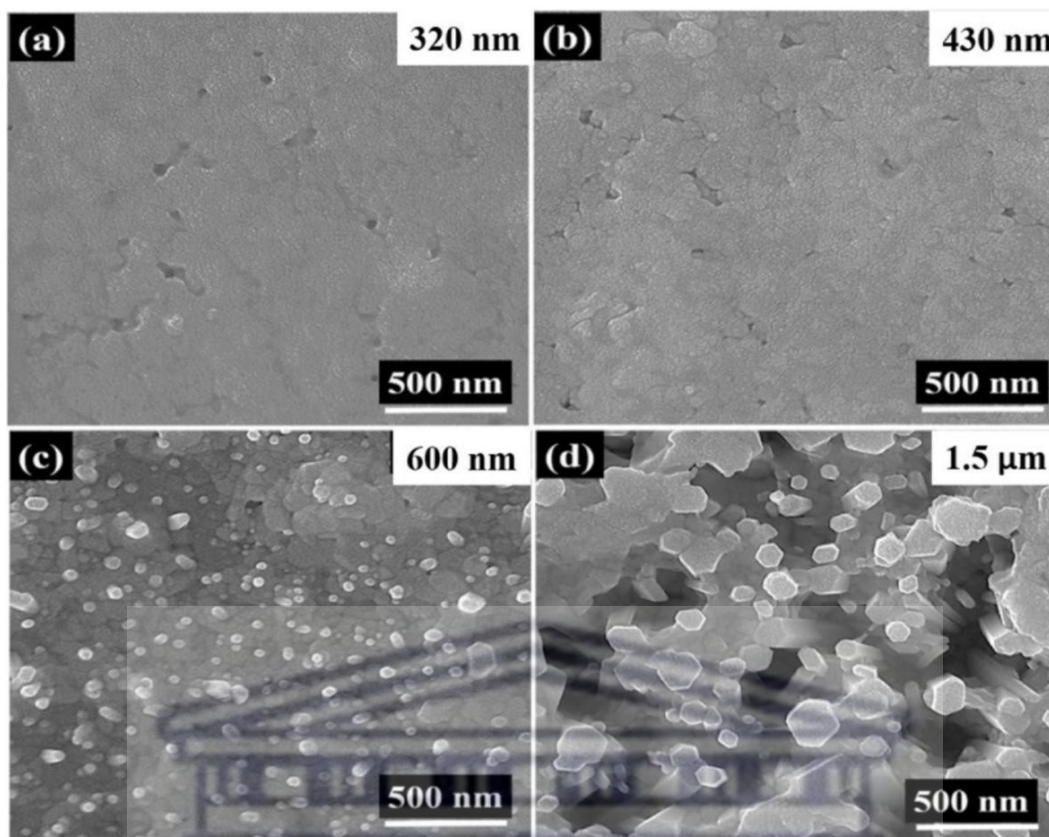


Fig. 3.9: SEM micrographs of $\text{MAPbI}_{3-x}\text{Cl}_x$ on various lengths of ZnO NWs [3.15]

3.6 Ion Migration and the Role of Chlorine Ions in Improving the Quality of $\text{MAPbI}_{3-x}\text{Cl}_x$ Layers

Chloride-iodide perovskites have attracted a lot of interest. However, the exact role that the Cl ions play in improving the overall perovskite layer stability and performance, remains a topic of hot debate. Adding a trace amount of Cl can significantly enhance both (a) opto-electronic properties and (b) morphology of the overall $\text{MAPbI}_{3-x}\text{Cl}_x$ film. It is well reported that Cl addition improves optoelectronic properties such as long carrier diffusion length and lifetime. However, other optical properties such as absorption and photogeneration are not apparent. Elsewhere, the Cl doping also significantly improves the conductivity of the $\text{MAPbI}_{3-x}\text{Cl}_x$ films compared to

MAPbI₃. Doping passivates dangling bonds at the interfaces or grain boundaries within the crystalline film and thereby causes band bending at these interfaces [3.17]. The addition of Cl also improves the crystallinity and film formation, resulting in larger crystalline domains. Photovoltaic performance highly depends on the film's crystallinity and morphology, with large crystal domain sizes and compact crystal structures such as cubic and tetragonal lattices preferable improved performance. In addition, surface coverage and film conformity are also crucial for high efficiency devices. Fig. 3.10 presents a schematic comparison between pure iodide perovskite and chloride-iodide perovskite films, and provides a visual summary of the three main challenges of chloride-iodide thin films. As shown in Fig. 3.10 (a, right) the mixed halide thin film has a long diffusion length, long carrier lifetime, large grain size, more Cl⁻ ion migration and less I⁻ ion migration compared to the pure iodide perovskite in Fig. 3.10 (a, left). However, as shown in Fig. 3.10 (b) Cl and I have a radius mismatch, Cl and I phase segregate during film growth and Cl sublimation during annealing is also prevalent [3.18].

Iodine has a bigger ionic radius than chlorine and it is postulated that the incorporation of the smaller sized Cl ions in the perovskite structure, leads to a more compact unit cell, which should reduce I⁻ migration. However, due to the mismatch it is also extremely challenging to incorporate Cl⁻ ions and at the same time reduce Cl⁻ migration. Ion migration is one of the most difficult concepts to understand and master in perovskite devices and is the underlying cause of poor stability [3.18]. The presence of vacancies in the perovskite lattice provides a pathway for ion migration [3.19, 3.20]. For example, I⁻ may easily migrate through the perovskite grains and even out the perovskite layer through interference with the metal electrode in a solar cell. The migrated iodide ions do not return to their original positions in the lattice, causing residual stress and strain within the crystal and overall poor stability of the perovskite layer. In the MAPbI₃ molecule, the iodide ion has the lowest defect activation energy of 0.58 eV, meaning that I⁻ diffusion is almost spontaneous at room temperature. The activation energy of the MA⁺ cation is 0.84 eV and the Pb²⁺ ion 2.31 eV, meaning that the Pb sublattice is immobile and do not migrate [3.21]. The most effective strategy to mitigate ion migration is enhancement of the chemical bonding among the perovskite ions [3.22]. Saidaminov *et al.* [3.23] suggested that small ion Cl⁻

incorporation suppresses the density of vacancy defects, which in turn cause lattice strain. The strain, in turn, causes tilting of the PbI_6 or PbCl_6 octahedra and ultimately the formation of halide vacancies. The group showed that this could be reduced by incorporating small ions such as Cl.

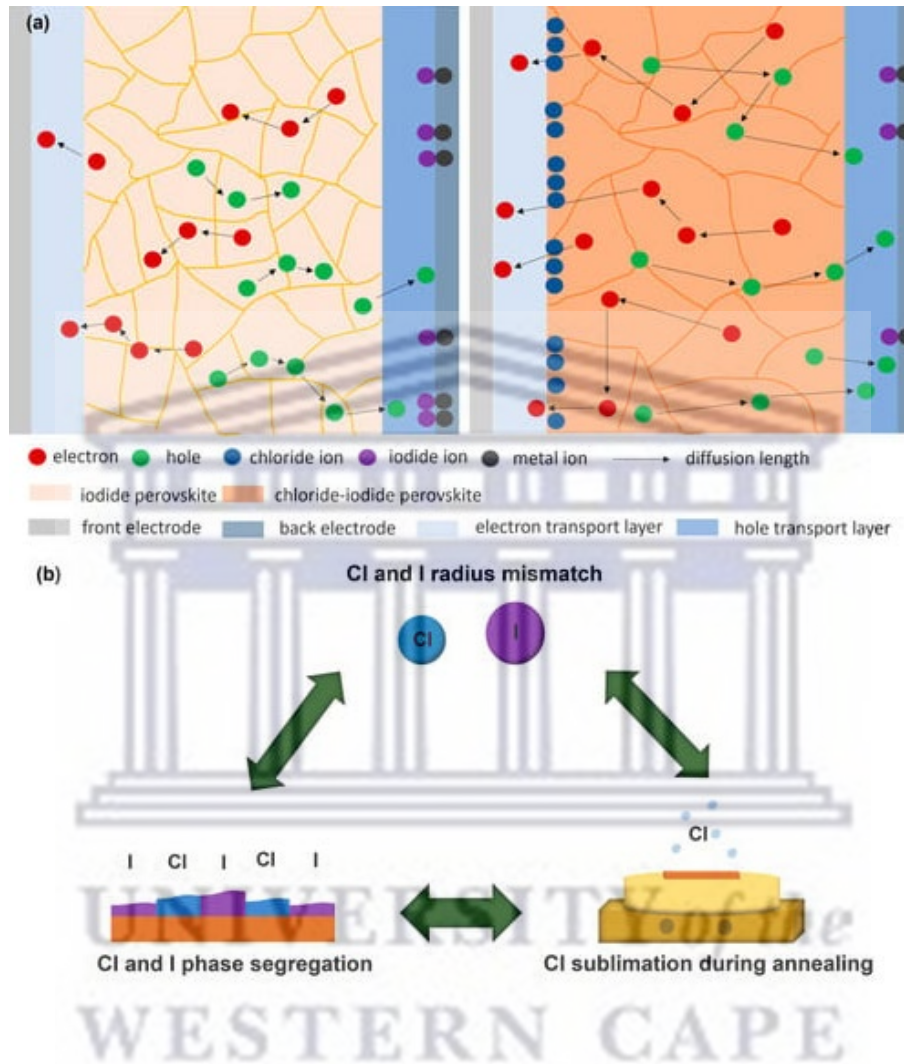


Fig. 3.10: Schematic representation of: (a) (left) MAPbI₃ and (right) MAPbI_{3-x}Cl_x thin films during operation in a solar cell; (b) three major issues facing MAPbI_{3-x}Cl_x thin films, namely ion radius mismatch, phase segregation and sublimation issues during annealing [3.18]

3.7 Phase Segregation and Cl Sublimation during Annealing

Chlorine and iodine phase segregation is very common in $\text{MAPbI}_{3-x}\text{Cl}_x$ perovskites. It is very challenging to synthesise a continuous, properly distributed chloride-iodide solid-phase film due to ion migration. Phase segregation in chloride-iodide perovskites occurs either during growth (Fig. 3.4, stage 2) or during annealing (Fig. 3.4, stage 3). During film growth, the constituent ions choose the weakest bonding interactions and eventually configure in the least energetically favourable configuration. This results in the formation of heterogeneous nucleation sites instead of homogeneous nucleation [3.18]. Tidhar *et al.* [3.24] found that the addition of PbCl_2 in the perovskite precursor results in the formation of nanocrystals, which act as heterogeneous nucleation sites at the time of perovskite crystal formation in the solution. As such if both PbI_2 and PbCl_2 are present, there is a high possibility of the formation of two different phase domains, such as MAPbI_3 and MAPbCl_3 . However, the formation of a wide-bandgap MAPbCl_3 phase is problematic for solar cell operation, as it generates fewer electron-hole pairs during illumination, inhibits electron transfer and deteriorates the overall photovoltaic performance [3.25].

Williams *et al.* [3.25] found that isolated PbCl_2 nucleation occurs directly after deposition and annealing of the films, as shown in Fig. 3.11 (a). During annealing, a Cl-rich region (shown in yellow) forms near the substrate surface (Fig. 3.11 (b)), whereas after complete annealing, segregated Cl and I phases (Fig. 3.11 (c)) form. Qiao *et al.* [3.26] showed that these phases decompose into MAPbI_3 and MAPbCl_3 over time. Furthermore, MAPbI_3 and MAPbCl_3 form tetragonal and cubic lattices, respectively, which cause phase segregation and eventual local residual stress and strain along the crystalline grain boundaries. In turn, localised stress and strain assist in the formation of vacancies, which may initially create shallow defects that eventually turn into deep traps via charge transfer with oxygen or water molecules – these processes accelerate perovskite degradation in ambient conditions. Saidaminov *et al.* [3.23] showed that a small amount of Cl substitution drastically reduces the lattice strain and suppresses defect formation.

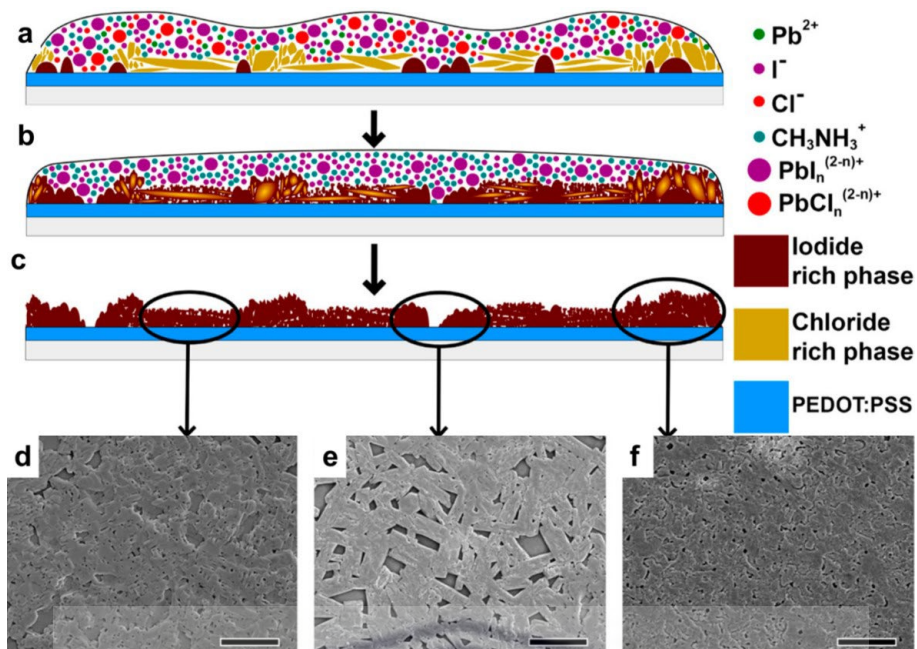
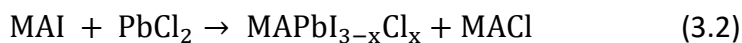


Fig. 3.11: Chloride–iodide perovskite film formation and morphology: (a) nucleation during deposition, (b) phase evolution and (c) growth during annealing; (d - f) SEM micrographs of the three major morphological constituents (scale bars = 2 μm) [3.24]

The conversion of a substance from the solid to gaseous state without initially transforming into a liquid, is known as sublimation. During annealing, the sublimation of chlorine plays a crucial role in the chloride–iodide perovskite formation. Grätzel *et al.* [3.27] suggest that the Cl-doped state would not exist at high annealing temperatures since the Cl-ion-containing phase would melt at 103 °C. Dualeh *et al.* [3.28] showed that a minimum temperature of 80 °C is required to ensure sufficient solvent vaporisation and perovskite crystallisation, whereas at high annealing temperatures additional PbI_2 is formed, which is detrimental to photovoltaic performance, since PbI_2 is insulating.

At lower annealing temperatures, the conversion to perovskite is summarised by the following the reaction:



As the annealing temperature is increased, additional PbI_2 forms according to:



MAPbCl_3 has a lower formation threshold energy and boiling point than $\text{MAPbI}_{3-x}\text{Cl}_x$ and decomposes into PbCl_2 and MACl during annealing. If the MAPbCl_3 phase persists during annealing, Cl could leave the film as MACl . The emission of Cl causes unwanted vacancies and pinholes in the perovskite layer. From equations (3.2) and (3.3) residual MAI is always formed during annealing, which ultimately converts into MAPbI_3 . A small amount of extra PbCl_2 could, however, enable the removal of excess MAI , even at low annealing temperatures. As such a case, longer annealing time will be needed to properly form chloride–iodide perovskite [3.29].

3.8 Deposition of Ossila Mixed-Halide Perovskite Precursor Ink on ZnO NW Arrays

A perovskite precursor solution (also referred to as ink) was purchased from Ossila (Leeds, United Kingdom). The ink is specifically manufactured by Ossila for processing by spin-coating in air and low humidity. The company states on their website that “...using a mixture of methyl ammonium iodide (MAI) and lead chloride (PbCl_2) dissolved in dimethyl formamide, our I101 perovskite ink will convert to a methylammonium lead halide perovskite under heat. The final product is a methylammonium lead iodide perovskite with trace amounts of chlorine given by the formula $\text{CH}_3\text{NH}_3\text{PbI}_{3-x}\text{Cl}_x$...”



Fig. 3.12: Ossila I101 perovskite [<https://www.ossila.com/products/perovskite-ink-air>]

During processing, the ink was heated and stirred for at least 2 hours at 70 °C to allow for complete redissolution of MAI and PbCl₂ solutes. The hot ink was then allowed to cool down to room temperature before deposition. A ZnO nanowire substrate was placed on the spin coater, shown in Fig. 3.13, and 30 - 50 µl of the ink dispensed on the substrate. As an initial experiment, the recommended spin-coating procedure, annealing range and time as provided by Ossila, was performed. This means that the substrate with the ink was spin-coated at 2000 rpm for 30 s, followed by annealing on a hot-plate at 90 °C, for 120 mins in air. After annealing, the film was placed into the sample box and the box was covered with a foil and vacuum-sealed to avoid the sample being exposed to sunlight and oxygen. The spin-rate, substrate annealing temperature and time were subsequently changed and investigated, as follow:

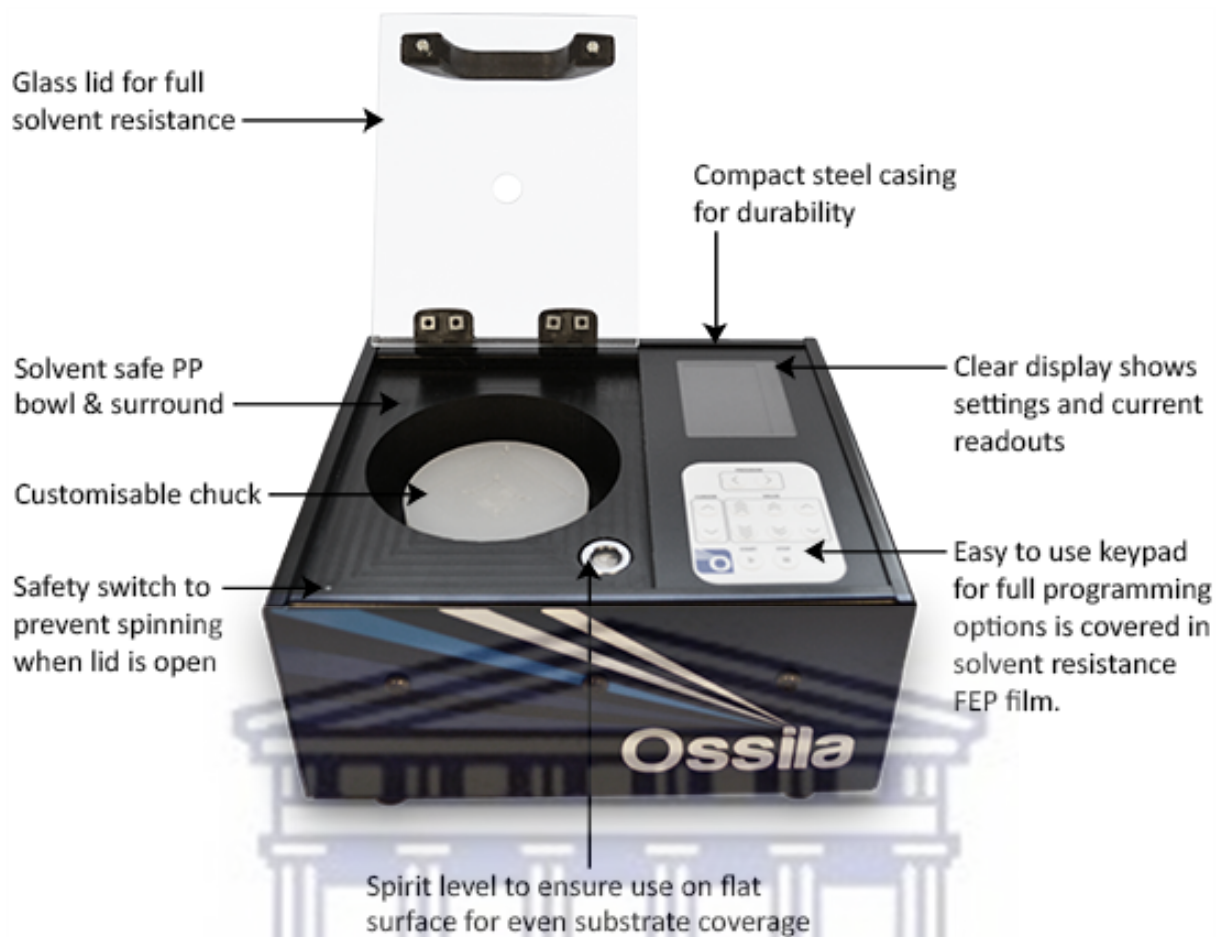


Fig. 3.13: Ossila spin coater used during this study for the deposition of $\text{MAPbI}_{3-x}\text{Cl}_x$ thin films

UNIVERSITY of the
WESTERN CAPE

Table 3.1: Effect of the spin-coating rate on perovskite morphology

Sample	Time (hrs)	Temperature (°C)	Zn(NO ₃) ₂ ·6H ₂ O (mg)	HMTA (mg)
NW 1000rpm	1	120	520.6	245.3
NW 2000rpm	1	120	520.6	245.3
NW 3000rpm	1	120	520.6	245.3

Table 3.2: Effect of annealing temperature on perovskite morphology

Sample	Time (hrs)	Temperature (°C)	Zn(NO ₃) ₂ ·6H ₂ O (mg)	HMTA (mg)
NW 80	1	80	520.6	245.3
NW 90	1	90	520.6	245.3
NW 120	1	120	520.6	245.3

Table 3.3: Effect of annealing time after spin-coating on perovskite morphology

Sample	Time (hrs)	Temperature (°C)	Zn(NO ₃) ₂ ·6H ₂ O (mg)	HMTA (mg)
NW 1h	1	120	520.6	245.3
NW 2h	2	120	520.6	245.3
NW 3h	3	120	520.6	245.3

References

- [3.1] J. D. Le Roux and D. R. Paul, "Preparation of Composite Membranes by a Spin Coating Process" *J. Membr.* 74 (1992) 233 – 252, doi: [https://doi.org/10.1016/0376-7388\(92\)80064-Q](https://doi.org/10.1016/0376-7388(92)80064-Q)
- [3.2] X. Chen, Y. Hu, Z. Xie and H. Wang, (2018) "Chapter 3: Materials and Design of Photocatalytic Membranes" *Photocatalytic Membranes and Photocatalytic Membrane Reactors*, Elsevier, United Kingdom, doi: <https://doi.org/10.1016/B978-0-12-813549-5.01001-X>
- [3.3] A. G. Emslie, F. T. Bonner and L. G. Peck, "Flow of a Viscous Fluid on a Rotating Disk" *J. Appl. Phys.* 29 (1958) 858, doi: <https://doi.org/10.1063/1.1723300>
- [3.4] Y. Y. Huang and K. S. Chou, "Studies on the Spin Coating Process of Silica Films" *Ceram. Int.* 29 (2003) 485 – 493, doi: [https://doi.org/10.1016/S0272-8842\(02\)00191-8](https://doi.org/10.1016/S0272-8842(02)00191-8)
- [3.5] B. Cai, W.-H. Zhang and J. Qiu, "Solvent Engineering of Spin-coating Solutions for Planar-structured High-efficiency Perovskite Solar Cells" *Chinese Journal of Catalysis* 36 (2015) 1183 – 1190, doi: [https://doi.org/10.1016/S1872-2067\(15\)60929-9](https://doi.org/10.1016/S1872-2067(15)60929-9)
- [3.6] P. Murugan, T. Hu, X. Hu X and Y. Chen, "Current Development Toward Commercialisation of Metal-Halide Perovskite Photovoltaics" *Advanced Optical Materials* 9 (2021) 2100390, doi: <https://doi.org/10.1002/adom.202100390>
- [3.7] K. L. Gardner, J. G. Tait, T. Merck, W. Qiu, U. W. Paetzold, L. Kootstra, *et al.*, "Nonhazardous Solvent Systems for Processing Perovskite Photovoltaics", *Adv. Energy Mater.* 6 (2016) 1600386, doi: <https://doi.org/10.1002/aenm.201600386>
- [3.8] N. J. Jeon, J. H. Noh, W. S. Yang, Y. C. Kim, S. Ryu, J. Seo, *et al.* "Compositional Engineering of Perovskite Materials for High-Performance Solar Cells" *Nature* 517 (2015) 476 – 480, doi: <https://doi.org/10.1038/nature14133>
- [3.9] M. Liu, M. B. Johnston and H. J. Snaith, "Efficient Planar Heterojunction Perovskite Solar Cells by Vapour Deposition" *Nature* 501 (2013) 395 – 398, doi: <https://doi.org/10.1038/nature12509>

- [3.10] M. J. Patel, H. Baishya, R.K. Gupta, R. Garai and P. K. Iyer, (2022) “Book Chapter: Thin Film Solution Processable Perovskite Solar Cell”, Recent Advances in Multifunctional Perovskite Materials, Intech Open, doi: <https://doi.org/10.5772/intechopen.106056>
- [3.11] M. Anaya, J. F. Galisteo-López, M. E. Calvo, C. López and H. Míguez, “Photophysical Analysis of the Formation of Organic–Inorganic Trihalide Perovskite Films: Identification and Characterization of Crystal Nucleation and Growth” J. Phys. Chem. C 120 (2016) 3071 – 3076, doi: <https://doi.org/10.1021/acs.jpcc.6b00398>
- [3.12] D. Liu and T. Kelly, “Perovskite Solar Cells with a Planar Heterojunction Structure Prepared using Room-Temperature Solution Processing Techniques” Nature Photon 8 (2014) 133 – 138, doi: <https://doi.org/10.1038/nphoton.2013.342>
- [3.13] R. Zhang, C. Fei, B. Li, H. Fu, J. Tian and G. Cao, “Continuous Size Tuning of Monodispersed ZnO Nanoparticles and Its Size Effect on the Performance of Perovskite Solar Cells” ACS Appl. Mater. Interfaces 9 (2017) 9785, doi: <https://doi.org/10.1021/acsami.7b00726>
- [3.14] M. De Bastiani, V. D’Innocenzo, S. D. Stranks, H. J. Snaith and A. Petrozza, “Role of the Crystallization Substrate on the Photoluminescence Properties of Organolead Mixed Halides Perovskites”, APL Materials 2 (2014) 081509; doi: <https://dx.doi.org/10.1063/1.4889845>
- [3.15] M. Makenali, I. Kazeminezhad, F. A. Roghabadi and V. Ahmadi, “Efficiency Improvement of Perovskite Solar Cells by Charge Transport Balancing using Length Tunable ZnO Nanorods and Optimised Perovskite Morphology” Solar Energy Materials and Solar Cells 230 (2021) 111206, doi: <https://doi.org/10.1016/j.solmat.2021.111206>
- [3.16] D.-Y. Son, J.-H. Im, H.-S. Kim and N.-G. Park, “11% Efficient Perovskite Solar Cell Based on ZnO Nanorods: An Effective Charge Collection System” J. Phys. Chem. C 118 (2014) 16567 – 16573, doi: <https://doi.org/10.1021/jp412407j>
- [3.17] Y. Zhao and K. Zhu, “CH₃NH₃Cl-Assisted One-Step Solution Growth of CH₃NH₃PbI₃: Structure, Charge-Carrier Dynamics, and Photovoltaic Properties of Perovskite Solar Cells” J. Phys. Chem. C 118 (2014) 9412 – 9418, doi: <https://doi.org/10.1021/jp502696w>

- [3.18] A. H. Howlader and A. Uddin, "Progress and Challenges of Chloride–Iodide Perovskite Solar Cells: A Critical Review" *Nanomanufacturing* 3 (2023) 3 177 – 216, doi: <https://doi.org/10.3390/nanomanufacturing3020012>
- [3.19] T. Zhang; C. Hu and S. Yang, "Ion Migration: A 'Double-Edged Sword' for Halide-Perovskite-Based Electronic Devices" *Small Methods* 4 (2020) 1900552; doi: <https://doi.org/10.1002/smt.201900552>
- [3.20] Y. Zhang, M. Liu, G. E. Eperon, T. C. Leijtens, D. McMeekin, M. Saliba, *et al.*, "Charge Selective Contacts, Mobile Ions and Anomalous Hysteresis in Organic–Inorganic Perovskite Solar Cells" *Mater. Horiz.* 2 (2015) 315 – 322, doi: <https://doi.org/10.1039/C4MH00238E>
- [3.21] Z. Li, C. Xiao, Y. Yang, S. P. Harvey, D. H. Kim, *et al.*, "Extrinsic Ion Migration in Perovskite Solar Cells" *Energy Environ. Sci.* 10 (2017) 1234 – 1242; doi: <https://doi.org/10.1039/C7EE00358G>
- [3.22] F. Wu, R. Pathak and Q. Qiao, "Origin and Alleviation of J-V Hysteresis in Perovskite Solar Cells: A Short Review" *Catal. Today* 374 (2021) 86 – 101; doi: <https://doi.org/10.1016/j.cattod.2020.12.025>
- [3.23] M. I. Saidaminov, J. Kim, A. Jain, R. Quintero-Bermudez, H. Tan, G. Long, *et al.*, "Suppression of Atomic Vacancies via Incorporation of Isovalent Small Ions to Increase the Stability of Halide Perovskite Solar Cells in Ambient Air" *Nat. Energy* 3 (2018) 648 – 654; doi: <https://doi.org/10.1038/s41560-018-0192-2>
- [3.24] Y. Tidhar, E. Edri, H. Weissman, D. Zohar, G. Hodes, D. Cahen, "Crystallisation of Methyl Ammonium Lead Halide Perovskites: Implications for Photovoltaic Applications" *J. Am. Chem. Soc.* 136 (2014) 13249 – 13256, doi: <https://doi.org/10.1021/ja505556s>
- [3.25] S. T. Williams, F. Zuo, C.-C. Chueh, C.-Y. Liao, P.-W. Liang and A. K.-Y. Jen, "Role of Chloride in the Morphological Evolution of Organo-Lead Halide Perovskite Thin Films" *ACS Nano* 8 (2014) 10640 – 10654; doi: <https://doi.org/10.1021/nn5041922>
- [3.26] W.-C. Qiao, J. Yang, W. Dong, G. Yang, Q. Bao, R. Huang, *et al.*, "Metastable Alloying Structures in $\text{MAPb}_{1-x}\text{Cl}_x$ Crystals" *NPG Asia Mater.* 12 (2020) 68; doi: <https://doi.org/10.1038/s41427-020-00249-w>

- [3.27] M. Grätzel, *“The Light and Shade of Perovskite Solar Cells”* Nat. Mater. 13 (2014) 838 – 842; doi: <https://doi.org/10.1038/nmat4065>
- [3.28] A. Dualeh, N. Tétreault, T. Moehl, P. Gao, M. K. Nazeeruddin and M. Grätzel, *“Effect of Annealing Temperature on Film Morphology of Organic–Inorganic Hybrid Perovskite Solid-State Solar Cells”* Adv. Funct. Mater. 24 (2014) 3250 – 3258; doi: <https://doi.org/10.1002/adfm.201304022>
- [3.29] H. Yu, F. Wang, F. Xie, W. Li, J. Chen and N. Zhao, *“The Role of Chlorine in the Formation Process of ‘CH₃NH₃PbI_{3-x}Cl_x’ Perovskite”* Adv. Funct. Mater. 24 (2014) 7102 – 7108; doi: <https://doi.org/10.1002/adfm.201401872>



CHAPTER FOUR

Analytical Techniques

4.1 Introduction

This chapter is dedicated to describing the underlying physics and operating principles of the analytical instruments used to characterise the ZnO nanowires and $\text{MAPbI}_{3-x}\text{Cl}_x$ thin films. The first part discusses the imaging techniques used to characterise the physical nature of the ZnO nanowires and perovskite layers: these are scanning electron microscopy (SEM) and transmission electron microscopy (TEM). The second half of the chapter discusses the characterisation of the nanowires and perovskite crystal structure and optical behaviour, using X-ray diffraction (XRD), X-ray photoelectron spectroscopy (XPS) and ultraviolet-visible (UV-Vis) spectroscopy.

4.2 Electron Microscopy

An electron microscope produces an image of an object using an electron beam and magnification is obtained using electromagnetic fields. This is different from light-optical microscopes, which create an image using light waves and magnification is obtained using a system of glass optical lenses [4.1]. There are three types of electron microscopes, namely (a) scanning electron microscopes (SEMs), (b) transmission electron microscopes and (c) scanning-transmission electron microscopes (STEMs). This chapter only focuses on the first two.

4.2.1 Scanning Electron Microscopy (SEM)

(a) Applications of Scanning Electron Microscopy

The SEM is arguably the most versatile research tool at present, as it allows for the imaging of a wide range of materials in their bulk form at high resolution. In addition to being an imaging tool, modern SEMs also allow for quantification of the elemental composition of materials, as well as identification of crystalline phases, to name a few. The application of scanning electron microscopy may be summarised as follows:

Topography: The surface features of an object or “how it looks”, its texture; direct relation between these features and materials properties (hardness, reflectivity)

Morphology: The shape and size of the particles making up the object; direct relation between these structures and materials properties (ductility, strength and reactivity).

Composition: The elements and compounds that the object is composed of and the relative amounts of them; direct relationship between composition and materials properties (melting point, reactivity and hardness).

Crystallographic Information: How the atoms are arranged in the object; direct relation between these arrangements and materials properties (conductivity, electrical properties and strength)

[4.1].

(b) Components

Electron gun: An electron beam is thermionically emitted from an electron gun fitted with a tungsten filament cathode. Tungsten has the highest melting point and lowest vapour pressure of all metals, thereby allowing it to be heated for electron emission, and because of its low cost. Other types of electron emitters include lanthanum hexaboride (LaB₆) cathodes, and field emission guns (FEG), which may be of the cold-cathode type using tungsten single crystal emitters or the thermally assisted Schottky type, using emitters of zirconium oxide.

Condenser Lenses: After the beam passes the anode it is influenced by two condenser lenses that cause the beam to converge and pass through a focal point. In conjunction with the selected accelerating voltage

the condenser lenses are primarily responsible for determining the intensity of the electron beam when it strikes the specimen.

Apertures: The function of these apertures is to reduce and exclude extraneous electrons in the lenses. The final lens aperture located below the scanning coils determines the diameter or spot size of the beam at the specimen. The spot size on the specimen will in part determine the resolution and depth of field. Decreasing the spot size will allow for an increase in resolution and depth of field with a loss of brightness.

Scanning System: Images are formed by rastering the electron beam across the specimen using deflection coils inside the objective lens. The stigmator or astigmatism corrector is located in the objective lens and uses a magnetic field in order to reduce aberrations of the electron beam. The electron beam should have a circular cross section when it strikes the specimen however, it is usually elliptical thus the stigmator acts to control this problem.

Specimen Chamber: The lower portion of the column is specimen stage and controls are located. Specimens are mounted and secured onto the stage which is controlled by a goniometer. The secondary electrons from the specimen are attracted to the detector by a positive charge Manual stage controls are found on the front side of the specimen chamber for x-y-z movement.

Electron Detectors: Detectors collect the signal generated from interaction of beam with specimen. Electronic detectors convert the signal into digital images and the most often collected signals are secondary electrons (SE) by secondary electron detector (Everhart–Thornley Detector, or ETD), backscattered electrons (BSEs) by backscattered electrons detector (solid-state detector) and X-rays signal by energy dispersive spectrometer (EDS) detector.

Vacuum System: A diffusion pump, backed by a mechanical pump, produces vacuum. In the diffusion pump a stream of hot oil vapor strikes and pushes air molecules toward a mechanical pump that expels them from the system. A mechanical pump and valve system are used to pre-evacuate the system because a diffusion pump only operates after a vacuum is created. If the column is in a gas filled environment, electrons will be scattered collide with air molecules which

would lead to reduction of the beam intensity and stability. Similarly, other gas molecules, which could come from the sample or the microscope itself, could form compounds and condense on the sample. This would lower the contrast and obscure detail in the image. The chemical and thermal stability is necessary for a well-functioning filament (gun pressure). The field emission gun, LaB6 and tungsten filament requires $\sim 10^{-10}$, $\sim 10^{-6}$ and 10^{-4} Torr, respectively. Hence, the gun column of the electron microscope requires very high vacuum to facilitate the electron signals from the sample to the detector for better imaging [4.1 - 4.3].

(c) *Basic Operation of the SEM*

Ernst Ruska and Max Knoll [4.4] created the first electron microscope in 1931 with a resolution of 100 nm, which was later improved to 0.05 nm by the inclusion of electromagnetic lenses. The SEM is used in the same way as an optical stereo-binocular microscope to examine the morphology and shape of a specimen.

During operation, the electron gun produces an electron beam when tungsten wire is heated by current and accelerated by the anode (in case of a thermionic SEM). The beam then travels down the vacuum column, and is focused by the electromagnetic lenses towards the sample. The deflection coils guide the beam so that it scans the surface of the sample in a raster pattern. When the incident beam touches the surface of the sample it, the surface produces three main signals, namely: (a) SEs, (b) BSEs and (c) characteristic X-rays. Other signals are also produced, but is not relevant to this study. The emitted signals are trapped by electrical detectors, converted into digital images or spectra and displayed on a screen as either a digital image or line spectrum. SEs and BSEs are used for image formation, whereas X-rays are used to determine the elemental composition of the sample [4.1, 4.2].

During analysis, the aim is to image the true surface of the sample. As such, lower accelerating voltages (kV) are preferable to prevent beam penetration into the sample, since SEs emerge from the top surface structure of a sample. Therefore, it is common to image at low kV, in the range

1-5kV, even though the SEMs are capable of up to 30 kV. The specimen in an SEM is subjected to a narrow electron beam from an electron gun, which rapidly moves over or scans the surface of the specimen (Fig. 4.1). This causes a shower of SEs and other types of radiation to be emitted from the specimen's surface. The intensity of the SEs is determined by the irradiated object's structure and chemical composition. The ETD collects the SEs and generates electronic signals, which are scanned in the same way as television signals are scanned, to produce an image on a digital screen [4.1].

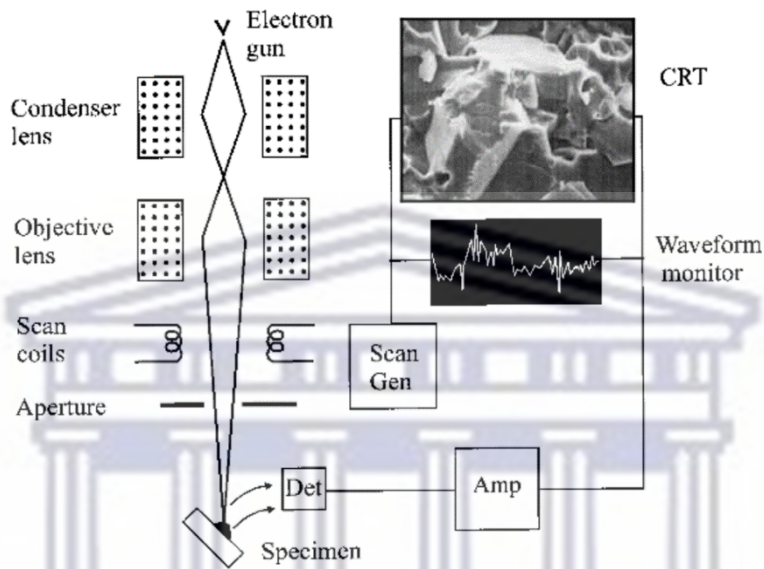


Fig. 4. 1: A schematic diagram showing the main components of a scanning electron microscope [4.1]

(d) *Energy Dispersive X-ray Spectroscopy*

Energy-dispersive X-ray spectroscopy (EDS or EDX) is an analytical technique commonly used in materials science and chemistry to determine the elemental composition of a sample, typically a solid material. EDS is often integrated with electron microscopes to provide valuable information about the chemical composition and spatial distribution of elements within a sample.

When an accelerated electron beam strikes a solid target, it induces electronic transitions in the atoms that result in X-rays, which are extremely energetic photons. Usually, when an incident electron strikes an

atom of the sample, it removes an electron from the metal's K-shell ($n = 1$ shell), leaving a vacancy or hole. X-rays are released if an electron from a different shell fills in that gap (electron transitions). Electronic transitions to the K-shell ($n = 1$), L-shell ($n = 2$), and M-shell ($n = 3$) are referred to as $K_{X\text{-rays}}$, $L_{X\text{-rays}}$, and $M_{X\text{-rays}}$ respectively.

The quality of the final EDS spectrum is primarily determined by the interaction volume and the volume from which the X-rays are generated. Additionally, both the average atomic weight of the sample and the energy of the X-rays have a significant impact on the amount of generated signal. For instance, only a few X-rays, such as carbon K_{α} , are detected because the solid sample easily absorbs them [4.1 – 4.3].

The identification of the elements present in the sample and their associated concentrations is made possible by the X-ray spectrum that is emitted by the specimen. When the primary X-rays pass through the specimen and interact with the sample's atoms, a small number of secondary X-rays may also be produced in addition to the emitted X-rays [4.5].

(e) Sample Preparation, Instrumentation and Data Collection

Fig. 4.2 (a) shows the Zeiss Auriga field emission SEM (FE-SEM, Electron Microscope Unit, University of the Western Cape) used to collect high-resolution images and elemental information of the ZnO and perovskite-deposited ZnO nanowires. The proper cleaning of the surface of the samples is important as it may contain a variety of unwanted contaminants, which interfere with the electron beam of the microscope. In this study, the ZnO nanowires and perovskite-deposited samples were mounted on double-side sticky conductive copper tape and stuck to a sample stage, which is connected to the ground of the SEM. Neither the ZnO nanowires, nor the perovskite-deposited nanowire samples were coated with either carbon or a metal. Instead, the samples were cleaned with a nitrogen plasma, using the Evactron 25 Plasma Cleaner, shown in Fig. 4.2 (b), which is hosted inside the Auriga SEM. The samples were cleaned at a plasma power of 14 W for 5 minutes, followed by flushing with nitrogen gas for 1 minute. Plasma cleaning is an effective technique for the removal of hydrocarbons and other carbon-rich contaminants on the surfaces.

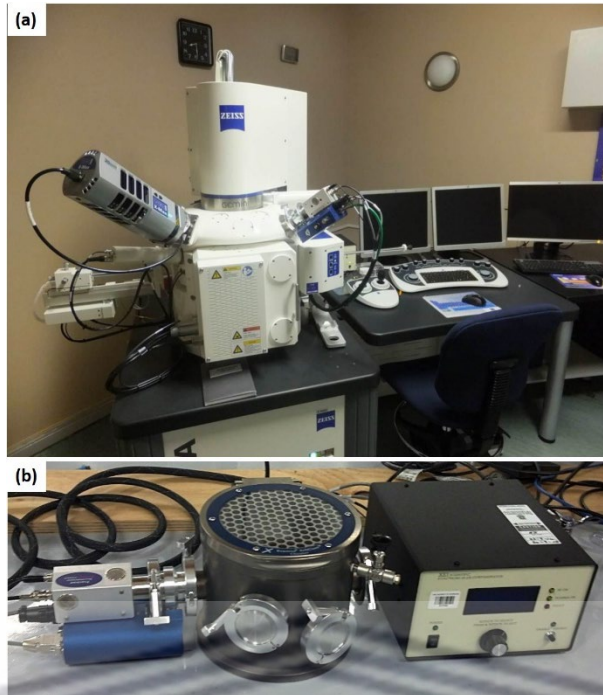


Fig. 4.2: (a) Zeiss Auriga FE-SEM, (b) Evactron 25 Plasma Cleaner

4.2.2 Transmission Electron Microscopy (TEM)

(a) Applications of TEM

TEMs provide topographical, morphological, compositional and crystalline information. The images allow researchers to view samples on an atomic level, making it possible to analyse structure and texture. This information is useful in the study of crystals and metals, but also has industrial applications [4.6].

(b) Basic Operation of the TEM

A high voltage electron beam is generated by electrical heating from a tungsten filament (cathode) or by field emission. The shaft of electrons is attracted towards an anode (magnetic lenses) and passes through an aperture. The beam is subsequently transmitted through the aperture, then an electromagnetic condenser, objective, intermediate, and projector lens. The focused electron beam is passed through a

very thin specimen (50 – 100 nm in size, semi-transparent for electrons, and carries information about the specimen's structure) loaded on a grid inserted in the pathway and adjusted by a goniometer [4.1, 4.6].

A part of the beam is absorbed, scattered and transmitted through the specimen. These rays then pass through an objective aperture and lens, which forms an intermediate image or electron diffraction pattern of the specimen. The intermediate image (or diffraction pattern) is further magnified by a set of intermediate lenses; projector lenses then provide the final magnification of the image/pattern, which is displayed on a fluorescence screen. The final image is viewed using an optical binocular mounted to the viewing glass. Situated below the fluorescent screen is a CCD (charge-coupled device) camera, which allows for digital recording and manipulation of the final image. The contrast of the final image is due to electron scattering rather than changes in absorbance, though mass thickness within the specimen also plays a role [4.1]. The major components of a typical TEM are shown in Fig. 4.3.

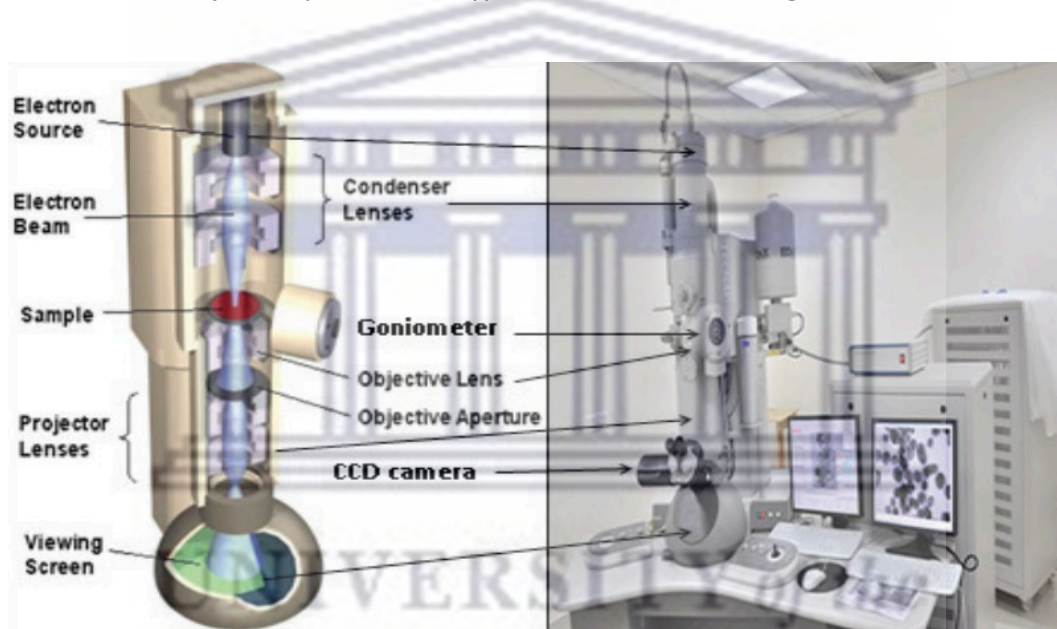


Fig. 4.3: Schematic diagram showing the main components of a TEM [4.3]

(c) *Selected Area Electron Diffraction*

When a beam of electrons impinges on a crystalline specimen, some of the electrons pass through specimen without interaction and hit a viewing screen, which is at distance L from the specimen, at position O . Other electrons are diffracted through an angle 2θ by the crystal planes of spacing d , and hit

the screen at position A, which is a distance r from O. This is shown schematically in Fig. 4.4. Bragg's Law of Diffraction, crystal planes and directions in a crystal will be discussed in the next section. From simple geometry and applying the small angle approximation, from Fig. 4.4 it can be determined that:

$$\frac{r}{L} = \tan(2\theta) = 2\theta \quad (4.1)$$

Combining (4.1) with the small angle simplified Bragg Law, it is found that:

$$\frac{r}{L} = \frac{\lambda}{d}, \text{ or } rd = L\lambda \quad (4.2)$$

where L and λ are independent of the specimen, and are a constant of the instrument, called the *camera constant*. It can be seen from (4.2) that the distance of the diffraction spot from the undiffracted spot, r , is inversely proportional to d -spacing of the diffracting planes. Hence, if the camera constant for the microscope is known, the interplanar spacing, d , can be determined simply by measuring r on the diffraction pattern.

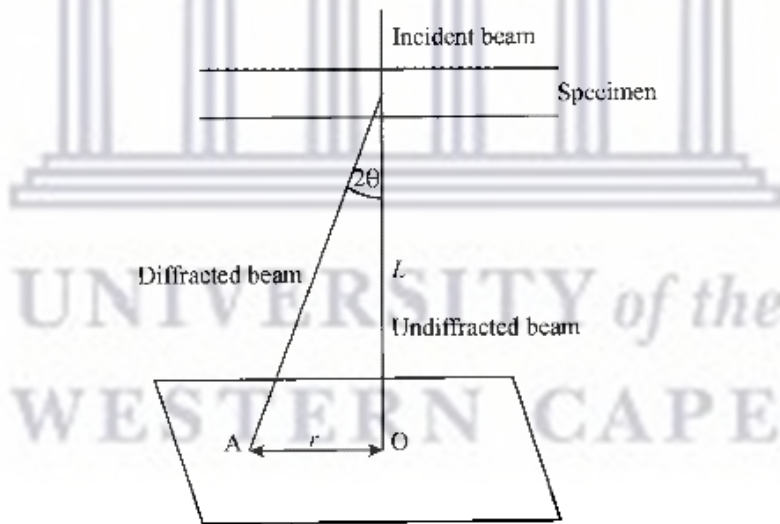


Fig. 4.4: Geometry of electron diffraction [4.1]

Single-crystalline specimen, oriented so that several sets of planes are parallel to the electron beam, produces a diffraction pattern consisting of a regular array of spots, as shown in Fig. 4.5 (a). If the specimen contains several crystals of different orientations, as shown in Fig. 4.5 (b), then the diffraction pattern is the sum of individual spot patterns, and more complicated – these types of patterns are typical of nanomaterials. From structure factor theory, only certain planes will diffract in the crystal, hence the number of possible d spacings and hence r spacings on the pattern is limited. Furthermore, spots are not randomly distributed, but fall on rings (each of which has constant r). Fig. 4.5 (c) shows a ring pattern from a specimen containing a large number of crystals of random orientation (poly-crystalline microstructure). In this case, the spots on the rings are so closely spaced, that the rings appear continuous [4.1]. In the TEM, a selected area diffraction (SAED) is typically collected, during which a small area of specimen selected by means of a diffraction aperture, although a larger area is being illuminated during imaging.

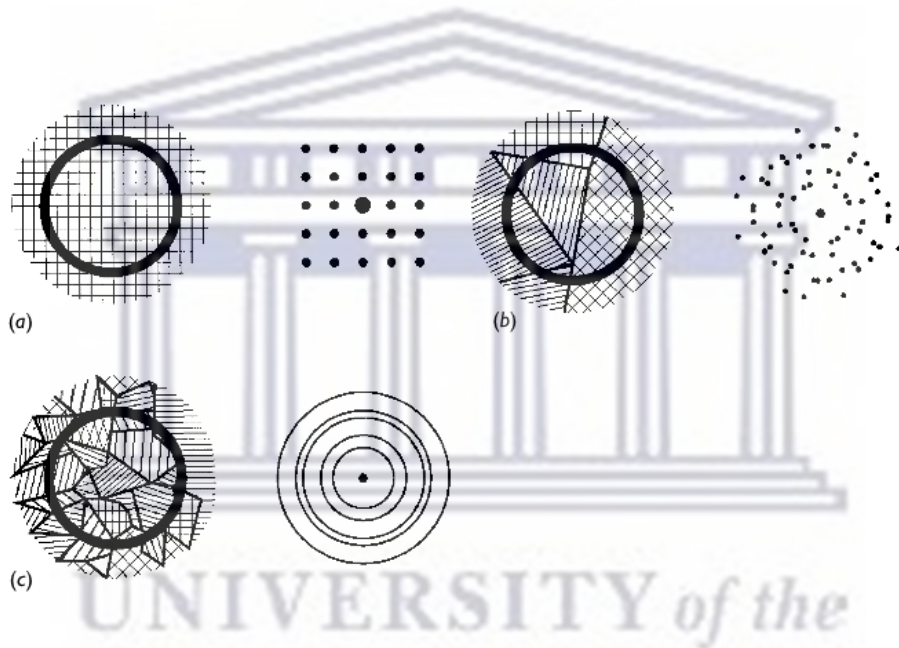


Fig. 4.5: Schematic representation of different electron diffraction patterns: (a) spot pattern from a perfect, single-crystalline material; (b) scattered spot pattern from a small number of crystalline grains and (c) a ring pattern emerging from a large number of randomly orientated grains [4.1]

(d) *Scanning Transmission Electron Microscopy and Spectral Image Mapping*

The first STEM was created by Manfred von Ardenne, a renowned applied physicist and prolific inventor, with the aim of imaging thicker samples, which posed a significant challenge for TEM imaging due to chromatic effects, without compromising image resolution. He explained how to calculate the current in an electron probe and the effects of lens aberrations on probe size. He also demonstrated where detectors should be placed for STEM imaging in bright-field (BF) and dark-field (DF), and he considered the effects of electron beam and amplifier noise on image quality. However, the total electron-beam intensity within the electron probe was significantly decreased when a smaller electron probe was used for high-resolution imaging, leading to a lengthy recording period to obtain each visually observable image. Since there were no low-noise electronic detectors that were appropriate at the time, photographic films had to be used to capture STEM images of a respectable quality [4.7].

Similar to traditional TEM, STEM is a strong imaging technique that scans a specimen with a focused electron beam. STEM, however, offers extra tools for high-resolution imaging and analysis that run simultaneously. STEM experiments can examine the structure and characteristics of materials at length scales of functional devices and materials down to single atoms due to instrumentation developments like highly coherent electron sources, aberration correctors, and direct electron detectors. STEM experiments can involve a wide range of adaptable operating modes, such as imaging, diffraction, spectroscopy, and 3D tomography [4.1, 4.7].

(e) *Key Components of STEM (Adapted from [4.1] and [4.7])*

- *Electron Beam Scanning:* A focused electron beam is raster-scanned across the sample, allowing for imaging with high spatial resolution.
- *Detectors:* STEM incorporates various detectors to collect different types of signals generated by the interaction of the electron beam with the sample, including transmitted electrons, scattered electrons, and X-rays.
- *Bright-Field (BF) Imaging:* BF STEM images are similar to conventional TEM images, where transmitted electrons are detected. This provides high-resolution imaging of the sample's morphology.

- *Annular Dark-Field (ADF) Imaging:* ADF STEM detects scattered electrons at high angles, which are sensitive to atomic number variations in the sample. ADF images provide contrast based on the Z-contrast, making them useful for imaging heavy elements and interfaces.
- *High-Angle Annular Dark-Field (HAADF) STEM:* A subtype of ADF STEM, HAADF STEM, uses detectors that collect electrons scattered at very high angles, enabling atomic-resolution imaging and enhancing sensitivity to heavy elements.
- *Energy-Dispersive X-ray Spectroscopy (EDS):* EDS detectors in STEM can simultaneously collect X-rays emitted from the sample, allowing for elemental analysis and mapping with high spatial resolution.
- *Spectral Image Mapping:* is an advanced technique that combines STEM with EDS to acquire detailed chemical information about a sample at high spatial resolution. It involves collecting a series of EDS spectra from various points across the sample and mapping the distribution of elements.

(f) *Key Components of Spectral Image Mapping*

- *Spectrum Acquisition:* EDS spectra are collected from each pixel or region of interest in the STEM image. Each spectrum contains information about the elements present and their relative concentrations.
- *Elemental Mapping:* Spectral Image Mapping generates elemental maps that display the spatial distribution of elements within the sample. Each pixel in the map represents the abundance of a specific element.
- *Spectral Analysis:* Researchers can perform detailed spectral analysis on the acquired data to identify chemical phases, quantify elemental compositions, and study variations in chemical composition at the nanoscale.
- *Quantitative Analysis:* Spectral Image Mapping allows for quantitative elemental analysis, providing information about the absolute concentration of elements in different regions of the sample.

(g) Sample Preparation and Data Acquisition

Fig. 4.6 shows the FEI Tecnai G²20 field emission TEM (FE-TEM) used in this study to investigate the internal structure of the synthesised ZnO nanowires. During sample preparation, the ZnO nanowires were scraped from the AZO substrate using a clean, sharp-edged blade and dispersed in 1 ml pure ethanol. A 3mm diameter copper grid coated with a perforated layer of carbon (also called holey carbon) was then dipped 3 times in the ZnO NW/ethanol dispersion. The Cu grid was then dried under a light source for 5 minutes and finally inserted in a FEI sample holder, as shown in Fig. 4.6 The sample holder was then inserted in the FEG-TEM to commence data collection. During analysis, normal bright-field micrographs were collected at a beam accelerating voltage of 200 kV; each image was collected using a CCD camera exposed for 60 seconds. SAED patterns were collected at a magnification of x78 000 using a 1 μ m diameter diffraction aperture. Dark-field images were collected in STEM mode, at 200kV using a Fischione high-angular annular dark-field (HAADF) detector. Energy dispersive x-ray spectra were collected with an EDAX liquid nitrogen cooled detector; each spectrum was collected for 2 minutes. STEM-EDS spectral images (or maps) were collected at a STEM magnification of x160 000, analysing a spectral image area of 300 x 300 nm², divided into 100 x 100 pixels, with each pixel analysed for 100 ms, yielding a total map collection time of approximately 45 minutes.

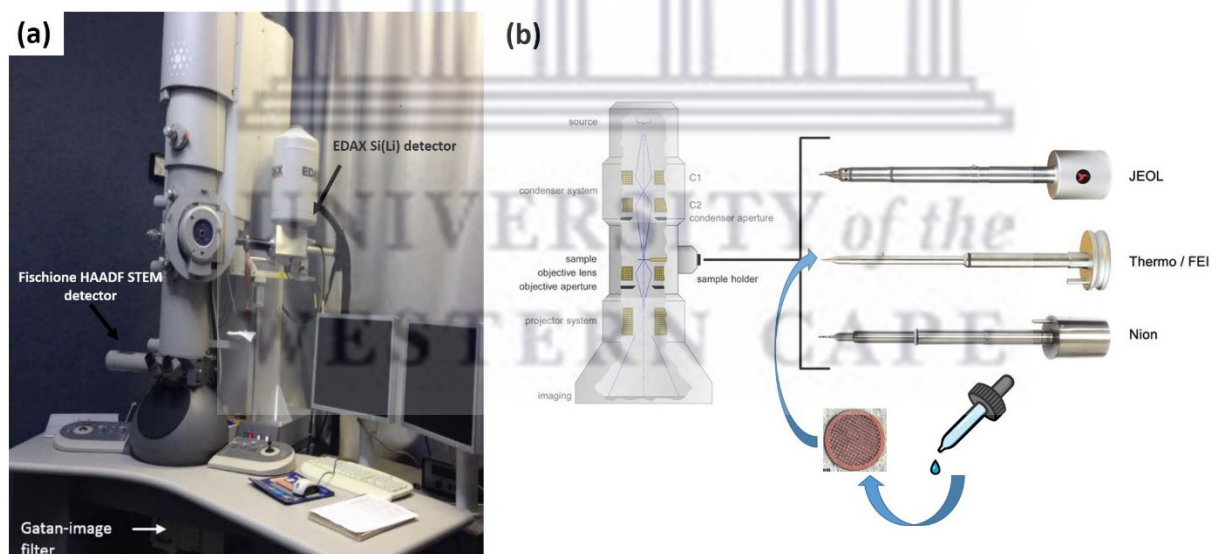


Fig. 4.6: FEI Tecnai G²20 FE-TEM (EMU, UWC)

4.3 X-Ray Diffraction (XRD)

In 1913, Sir William Henry Bragg and his son Sir William Lawrence Bragg showed that certain crystal faces reflect X-ray beams at certain angles of incidence, θ . Moreover, they discovered a relationship between the internal spacing between atomic layers in a crystal and the wavelength of the incident X-ray beam. This observation was significant as it showed that X-ray wave interference, now commonly known as X-ray diffraction (XRD), is possible by crystalline materials and provided concrete evidence for the periodic atomic structure of crystals, which had been predicted for decades [4.8].

4.3.1 Crystal Structure and Bravais Lattice

A crystal structure is made up of two parts: a space part called the *Bravais lattice*, and a chemistry part called the *basis*. To create the crystal structure, the basis must be arranged with the identical orientation and composition at each lattice point of the Bravais lattice. Copper has a face-centred cubic crystal (fcc) structure. A basis of one copper atom is placed on the lattice points of the face-centred cubic Bravais lattice to create this crystal. Diamond, another insulator, has a face-centred cubic crystal structure. A basis of two carbon atoms is placed on each lattice point of the face-centred cubic Bravais lattice to create this crystal. At each lattice point, the pair of atoms must have the same orientation. If one of the unit cell's corners is chosen as the origin, the coordinates of the carbon atoms of the basis at the origin are (0 0 0) and ($\frac{1}{4}$ $\frac{1}{4}$ $\frac{1}{4}$). This crystal structure can also be considered as two interpenetrating fcc structures with carbon atoms at each lattice point, with the origins of the two lattices separated by ($\frac{1}{4}$ $\frac{1}{4}$ $\frac{1}{4}$). This crystal structure can be found in the semiconductors silicon and germanium and is known as diamond cubic structure.

The Bravais lattice (space lattice) is a three-dimensional arrangement of points with identical surroundings. Translational symmetry is essential for the lattice, and Bravais demonstrated that there were only 14 distinct arrays that possessed this characteristic, and that these can form 7 groups. Cubic, Tetragonal, Hexagonal, Rhombohedral, Orthorhombic, Monoclinic, and Triclinic point lattices are listed in decreasing order of total symmetry. The unit cell is the smallest unit in the lattice that has full symmetry. The Bravais lattice determines the spatial component of a

crystal structure; the nature of the basis, which is placed on each lattice point with the identical composition and orientation, determines the chemistry of the crystal [4.9]. These seven crystal systems are cubic, tetragonal, hexagonal, orthorhombic, rhombohedral, monoclinic and triclinic. The lattice parameter relationships and unit cell sketches for each are represented in the figure below. Fig. 4.7 shows the 14 different 3-D configurations into which atoms can be arranged in crystals. A lattice can have a unit cell which is simply the smallest group of symmetrically aligned atoms which can be repeated in an array to make up the entire crystal [4.9].

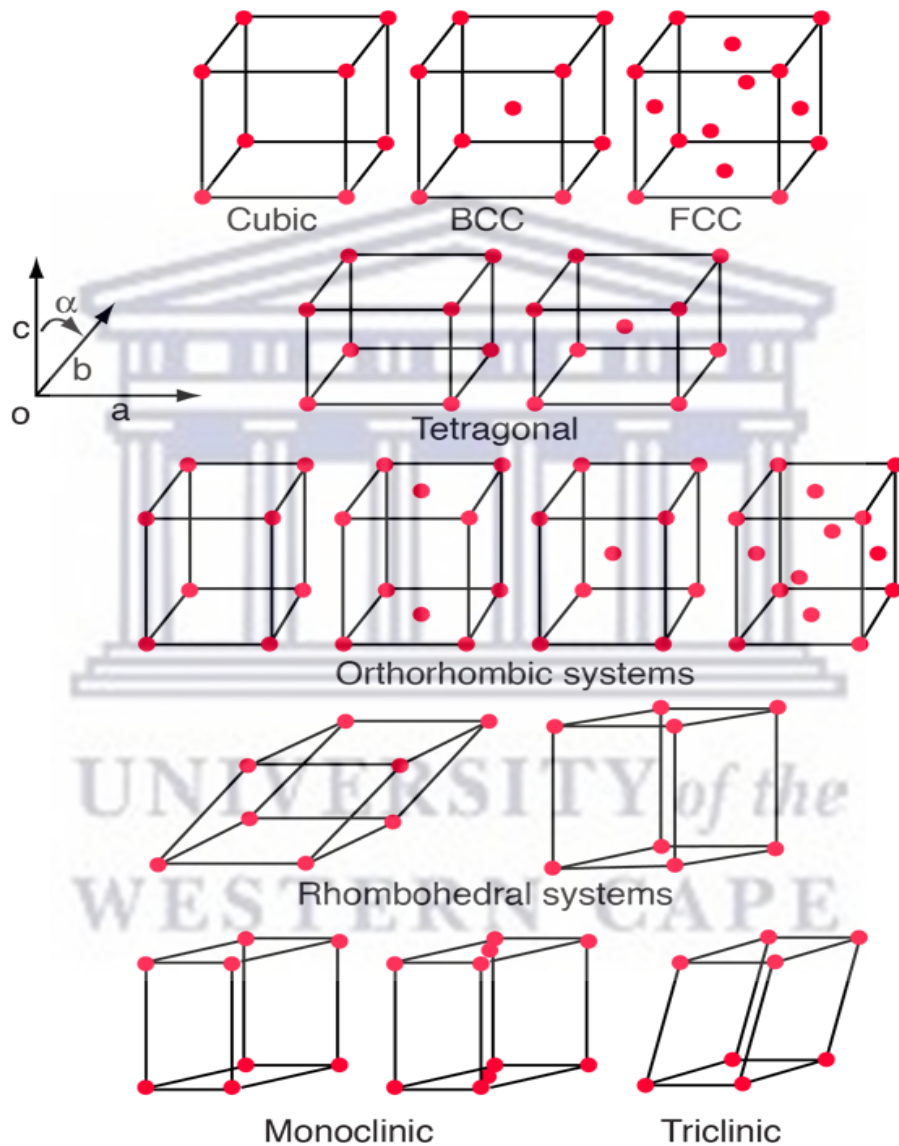


Fig. 4.7: The 14 Bravais Lattices [4.9]

4.3.2 Crystallographic Directions

The crystallographic directions describe a specific direction within the crystal lattice. They are represented using square brackets and three integers, denoting the direction of interest in terms of the lattice vectors. For example, $[uvw]$ represents a lattice direction along the u , v , and w axes.

How to Determine the Directions:

- A convenient-length vector is placed so that it crosses the coordinate system's origin. If parallelism remains, any vector may be translated without modification throughout the crystal lattice.
- The dimensions of the unit cells a , b , and c are used to calculate the length of the vector projection on each of the three axes.
- To get the smallest integer values, multiply or divide these three numbers by a common factor.
- Square brackets are used to enclose the three indices, which are not separated by commas, as in $[uvw]$. The reduced projections along the x , y , and z axes are represented by the integers u , v , and w , respectively. Fig. 4.8 shows a unit cell with directions indicated.

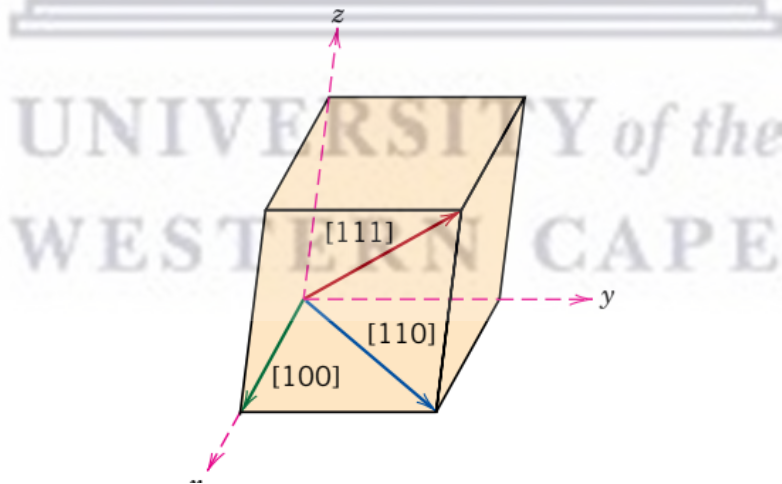


Fig. 4.8: Directions $[100]$, $[110]$ and $[111]$ with a unit cell $[4.10]$

For each axis, there is a positive and negative coordinate. The negative coordinates are represented by a bar over the appropriate index, i.e. $[1\bar{1}1]$. It shows that there is a negative component in the -y direction [4.10].

4.3.3 Crystallographic Planes

These describe a specific plane of atoms or lattice points within the crystal lattice. They are represented using curly braces and three integers, denoting the Miller indices of the plane. For example, $\{hkl\}$ represents a lattice plane with Miller indices h , k , and l . Miller indices (h, k, l) are used to uniquely identify a crystallographic plane within a crystal lattice. They are based on the reciprocals of the intercepts of the plane with the crystallographic axes (a , b , and c) of the lattice [4.10].

How to Identify Miller Indices:

- If the plane crosses the chosen origin, either a new origin must be set up at the corner of another unit cell, or another parallel plane must be created by a suitable translation within the unit cell.
- The length of the planar intercept for each axis is determined in terms of the lattice parameters a , b , and c at the point where the crystallographic plane either intersects or parallels each of the three axes.
- These numbers' reciprocals are used. It is possible to think of a plane that parallels an axis as having a zero index and an infinite intercept.
- These three numbers are multiplied or divided by a common factor, as needed, to produce the set of smallest integers.
- Lastly Miller indices are not separated by commas.

4.3.4 The X-ray Diffractometer

When high-energy electrons collide with metallic surfaces, they knock off bound electrons from atoms' inner shells. X-rays are emitted when electrons from the higher shells transition into the lower (now partially empty) shells. For example, the K_{α} line in copper ($\lambda = 154.18 \text{ pm}$) is created by the $n = 2$ to $n = 1$ transition, but the K_{β} line ($\lambda = 139.22 \text{ pm}$) is formed by the $n = 3$ to $n = 1$ transition. To obtain monochromatic X-ray beams, an x-ray tube is used with appropriate filters are used. The sample being studied may be either a powdered form of the solid or a single crystal. The Debye-Scherrer method, also called powder diffraction, is only applicable to powder samples [4.15]. Rolling a photographic film over the sample causes the diffraction pattern to trace a cone around the incident beam. Crystallites in the powder are distributed in a random pattern. If the incident light's angle is θ on any plane, the diffracted light will be at an angle of 2θ from the incident beam. The powdered sample is additionally rotated in the plane containing the X-rays to provide all feasible crystallite orientations towards the incident beam. Powder diffraction is highly effective in identifying materials because each substance's powder has a distinct diffraction pattern. This is shown schematically in Fig. 4.9. The incident angle $\omega = \theta$, is defined between the X-ray source and the sample. The diffraction angle, 2θ is defined between the incident beam and the detector. The incident angle is always $1/2$ of the detector angle 2θ .

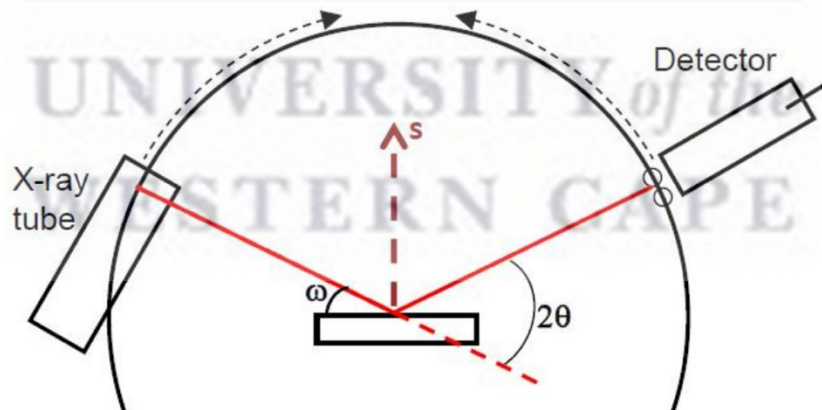


Fig. 4.9: A schematic diagram of a powder diffractometer [4.10]

4.3.5 Bragg's Law of Diffraction

Although Bragg's Law was used to explain the interference pattern of X-rays scattered by crystals, diffraction has been developed to study the structure of all states of matter using any beam, such as ions, electrons, neutrons, and protons, with a wavelength comparable to the distance between the atomic or molecular structures of interest. This law links the angle (at which the diffracted intensity is maximal) to the wavelength of X-rays and the inter-layer distance d between the planes of atoms/ions/molecules in the lattice. The details involved in the derivation of Bragg's Law are depicted in Fig. 4.10 below [4.10]. Constructive interference occurs only when:

$$n\lambda = AB + BC$$

$$n\lambda = 2AB$$

$$\sin \theta = AB/d$$

$$AB = d \sin \theta$$

$$n\lambda = 2d \sin \theta$$

Combining all the above relations, ultimately leads to Bragg's Law:

$$n\lambda = 2d_{hkl} \sin \theta_{hkl} \quad (4.3)$$

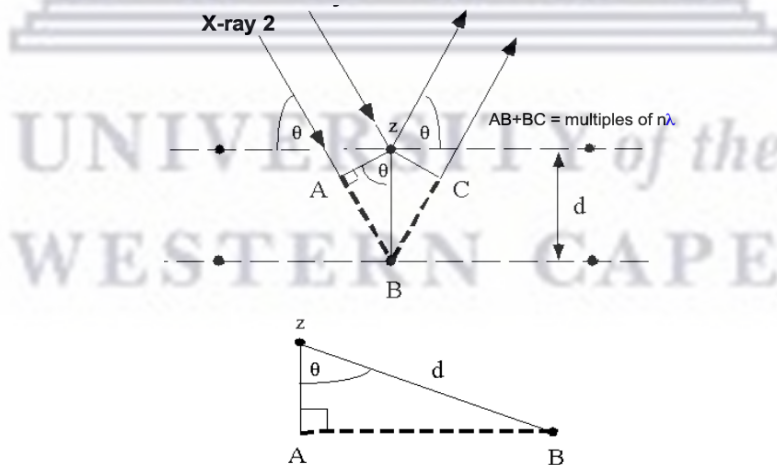


Fig. 4.10: Schematic representation of X-ray diffraction by a set of parallel planes and the derivation of Bragg's Law [4.10]

4.3.6 Instrumentation and Data Acquisition

In this study, XRD patterns were collected with a PANalytical Empyrean diffractometer with Cu K_{α} radiation ($\lambda=1.5406\text{\AA}$) as x-ray source, operated at 45 kV, 40 mA. This instrument, shown in Fig. 4.11, is hosted by the National Metrology Institute of South Africa, NMISA (CSIR Campus, Pretoria). The system was operated in θ - 2θ geometry, with each diffraction pattern collected at a 2θ range from 10 to 90 degrees, at 0.02 degrees step size, timed at 1 second per step for a total collection time of roughly 60 minutes. The raw data was subsequently analysed with X'Pert Pro and Highscore software, which allowed for phase identification and peak fitting. All ZnO NW samples were analysed without extra sample cleaning or preparation.



Fig. 4.11: PANalytical Empyrean diffractometer used in this work (NMISA, Pretoria)

4.4 Ultraviolet-Visible Spectroscopy (UV-Vis Spectroscopy)

Spectroscopy focuses on the investigation of the interaction of an electromagnetic field with matter. Historically, it was used to study how a prism disperses visible light based on wavelength. All interactions involving variations in radiative energy with wavelength or frequency were included in the original concept. A spectrum of emission from a wavelength- or frequency-dependent response is how spectroscopy data is displayed. In general, spectroscopy can be divided into two categories: (a) methods based on energy transfer between photon and sample, and (b) reflections, refractions, diffractions, dispersion, or scattering from the sample changing the amplitude, phase angle, polarisation, or direction of the electromagnetic radiation. For a fixed path length, UV-Vis spectroscopy can be used to determine the interaction of the absorbing species with radiation in the ultraviolet and visible regions of the electromagnetic spectrum. Predetermined wavelengths in these regions have been defined as: UV: 300 - 400 nm; visible (Vis): 400 - 765 nm and near infrared (NIR): 765 - 3200 nm. An instrument used for ultraviolet-visible (or UV-Vis) spectroscopy is called a UV-Vis-NIR spectrophotometer. Fig. 4.12 shows the electromagnetic spectrum and the small portion used to analyse materials during UV-Vis spectroscopy [4.11].

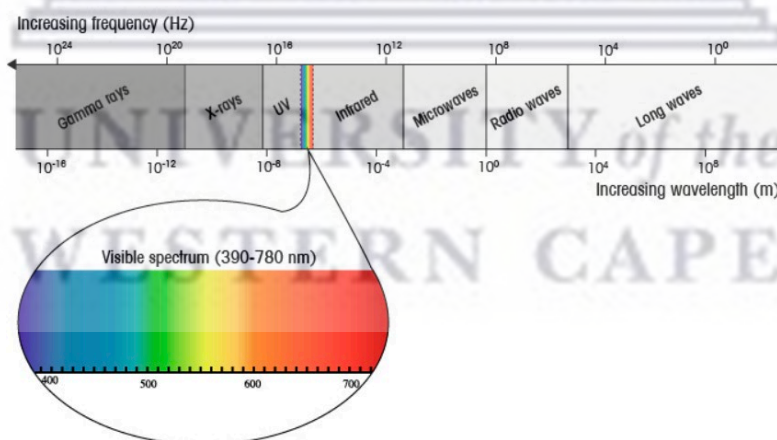


Fig. 4.12: A schematic showing the visible spectrum (390 – 780 nm) represented by only a small portion of the whole electromagnetic spectrum [4.11]

4.4.1 Operating Principle of UV-Vis Spectroscopy

(a) Light Source

A steady source that can emit light across a variety of wavelengths is required for this light-based technique. It is typical to use a single xenon lamp as a high intensity light source for both UV and visible wavelengths. However, compared to tungsten and halogen lamps, xenon lamps are more expensive and less stable. A tungsten or halogen lamp are used for visible light in instruments with two lamps, while a deuterium lamp is typically the source of UV light [4.12].

(b) Wavelength Selection

A wide-spectrum white light is produced by all of the light sources. The light is passed through a monochromator to focus it on a particular wavelength band. An entrance slit, a dispersion device to spread the light into various wavelengths (like a rainbow) and enable the selection of a nominated band of wavelengths, and an exit slit are all components of a monochromator [4.13]. The light of the nominated wavelengths passes through the exit slit and onto the sample.

(c) Detection

The sample's light is transformed into an electrical signal by a detector. It should have a linear response over a broad wavelength range, low noise, and high sensitivity, just like the light source. A photomultiplier tube detector or a photodiode detector are typically found inside spectrophotometers. On high-performance systems, there are additional specialized detectors to increase sensitivity or wavelength coverage. The sensitivity and wavelength range of each detector varies. When a system has more than one detector, the system will switch to the detector that matches the measurement's required wavelength range. Fig 4.13 shows a representative schematic of a common UV-Vis spectroscopy set-up [4.13].

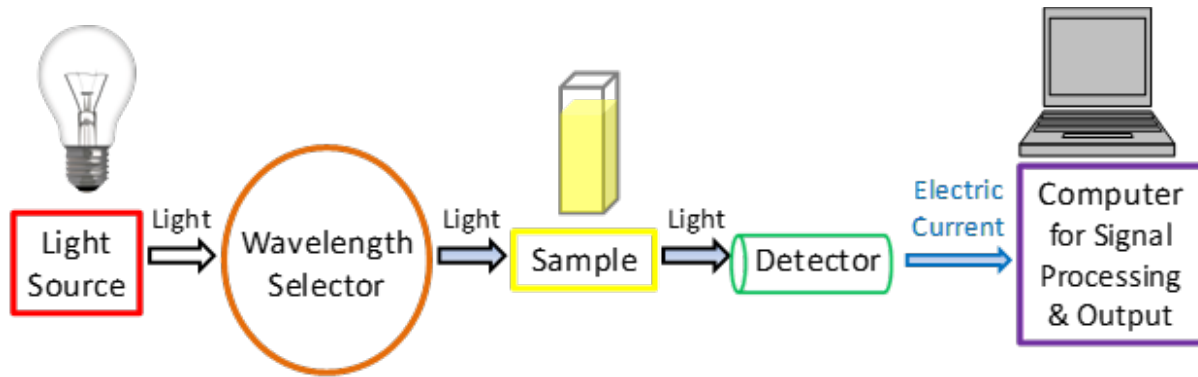


Fig. 4.13: Schematic showing the main components of UV-Vis spectrophotometer [4.13]

4.4.2 UV-Vis Spectra of Thin Films

UV-Vis is a widely used technique in semiconductors studies to accurately estimate the band gap energy of the semiconductors. Depending on the band position of the material, different types of electronic transitions can happen when the sunlight is absorbed. The HOMO-LUMO energy gaps, electrical and optical properties are examined using the UV-VIS Spectroscopy. The basic principles of visible spectroscopy and concepts such as the Beer-Lambert Law are used to explain the relationship of absorption and Transmission. The beer-Lambert Law explains that the light transmitted over the incident intensity is dependent on the path length of the light through the sample, the absorption cross section of the sample's transition, and the difference in the population of initial state and final state explained in equation (4.1) below [4.14]:

$$T = \frac{I_T}{I_0} = \exp(-\sigma(N_1 - N_2)) l \quad (4.4)$$

where I_T is the light transmitted, I_0 the incident intensity, l the path length through the layer, σ the absorption cross section of the material under investigation, N_1 the initial state and N_2 the final state of the absorbing species. Absorbance is defined as

$$A = \epsilon cl = -\log_{10}\left(\frac{I_T}{I_0}\right) \quad (4.5)$$

where ε is the molar absorptivity of the material under review and c the concentration of absorbing species. Normalising equation (4.5) gives the absorption coefficient as

$$\alpha = \frac{\ln(10)A}{l} = \ln(10)\varepsilon c \quad (4.6)$$

$$\alpha l = -\ln\left(\frac{I_T}{I_0}\right) \text{ or } I_T = I_0 \exp(-\alpha l) \quad (4.7)$$

A semiconductor is known as a direct band gap material when the conduction band and valence band are at the same value of k and the photon has enough energy to produce an electron-hole pair. In this case, the electron is promoted to the conduction band by a direct transition. However, if the minimum of the conduction band and the maximum of the valence band occur at different values of k , the promotion of an electron from the valence to the conduction band would result in a change in its momentum, and this must be provided by a phonon (i.e., a lattice vibration). This electronic transition can be classified by UV-vis as direct or indirect. The absorption spectrum can be interpreted to obtain the energy band gap of the thin film by fitting a tangent line to the curve [4.14].

4.4.3 Instrumentation and Data Acquisition

A Semiconsoft MProbe[®]20 Thin Film Measurement System, shown in Fig. 4.14, was used to collect UV-Vis transmission spectra in this study. During measurement, a baseline transmission spectrum was first collected, with no sample in the beam path. Thereafter an AZO reference sample was analysed to obtain a reference spectrum. This will be discussed in Chapter Five. Spectra were collected between 200 and 1000 nm, with no prior sample preparation necessary.



Fig. 4.14: Semiconsoft MProbe®20 spectrometer, hosted in the Department of Physics and Astronomy, UWC

4.5 X-ray Photoelectron Spectroscopy (XPS)

The photoelectric effect, which Einstein first described in 1905 and for which he received the Nobel Prize in 1921, is used in XPS, and involves atoms emitting electrons in response to incident electromagnetic radiation. When the energy of incoming photons exceeds the binding energy of the material's electrons, as predicted by Einstein, photoelectrons will be produced from the material; the energy of these photoelectrons is proportional to the frequency ($h\nu$), not the intensity or duration of exposure to the incident electromagnetic radiation [4.15].

XPS is a surface-sensitive, non-destructive tool that is used to examine the outermost 10 nm (30 atomic layers) of both naturally occurring and artificially created materials. By measuring the binding energies of elements, which are connected to the type and strength of their chemical bonds, XPS is frequently used to ascertain the following: a) the composition of material surfaces

(elemental identification), b) the relative abundances of these components on surfaces (semi-quantitative analysis), and c) the chemical state of polyvalent ions. The surfaces of various materials, including inorganic compounds (minerals), semiconductors, organic compounds, and thin films and coatings on naturally occurring and artificially created materials, are characterised using XPS [4.16].

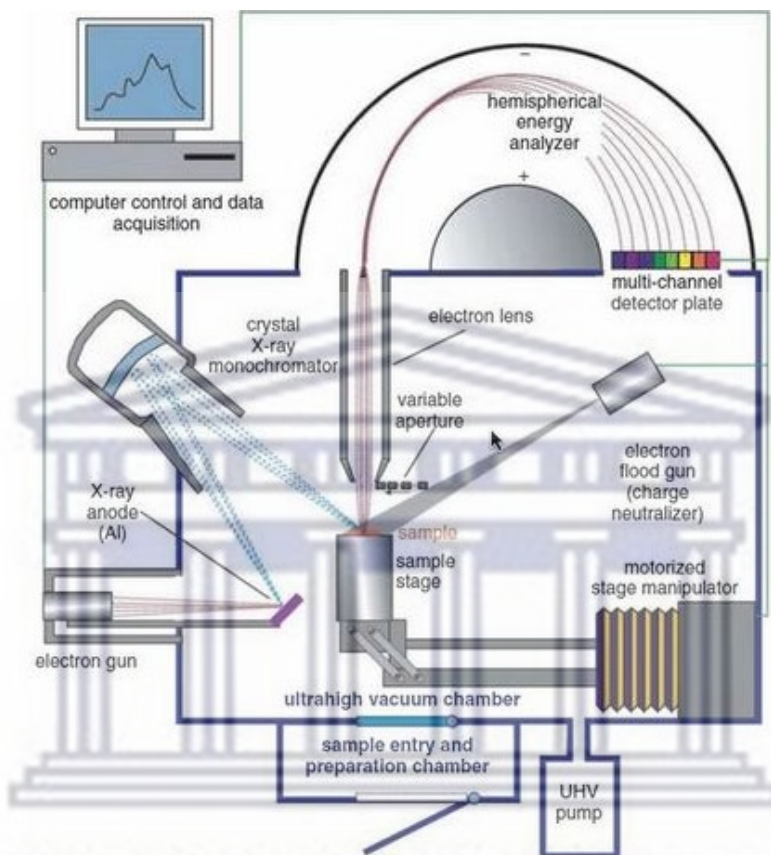


Fig. 4.15: Schematic representation of XPS instrumentation [4.15]

4.5.1 Operating Principle of XPS

XPS instruments consist of the following components:

- Ultrahigh vacuum system; typically, operating conditions are at $<10^{-10}$ kPa. This is required because the emitted photoelectrons have a relatively low energy and are readily absorbed by ambient atmosphere. In other words, photoelectrons have a relatively small

mean free path between sample and detector as they are readily adsorbed by gas molecules in the chamber.

- X-ray source; Al K_{α} or Mg K_{α} X-rays are typically used to excite the sample; a monochromator is used to permit only X-rays of this fixed energy to impinge on the sample.
- An electron energy analyser is used to discriminate among the energies of the photoelectrons that are produced. This is typically a Concentric Hemispherical Analyzer (CHA).
- Ar ion gun is used a) to sputter material surfaces to "dust off" environmental contaminants (e.g., adsorbed carbon from the atmosphere) off of material surfaces, and b) to obtain depth profiles across surface layers on the material surface.
- Charge neutralisation capability using an electron "flood gun" is used to minimize surface charging under the X-ray beam.
- Computer and data reduction software

The emission of the electron is done with the help of homogeneous light that has been applied on the material by the photoelectric effect. The measuring method of intensity distribution and electron energy is called XPS method

4.5.2 Physics of Photoelectron Emission

Photoelectron emission is a phenomenon in which electrons are emitted from a material's surface when it is exposed to electromagnetic radiation, typically in the form of photons. The emitted photoelectron is the result of complete transfer of the x-ray energy to a core level electron.

$$h\nu = BE + KE + \phi_{spec} \quad (4.8)$$

Equation (4.8) is the quantum mechanics equation of conservation of energy, which state that the energy of the X-ray is equal to the binding energy (BE) of electron plus the kinetic energy (KE) of the electron that is emitted and the work function (ϕ_{spec}), which is a constant value.

This equation can be manipulated to determine the binding energy of an electron

$$BE = h\nu - KE - \phi_{spec} \quad (4.9)$$

The element and orbital from which the photoelectron ejected are noted on photoelectron peaks. For instance, "O 1s" refers to electrons that leave an oxygen atoms 1s orbital. The sample should emit any electrons with binding energies less than the energy of the x-ray source so that they can be observed using the XPS technique. An electron's binding energy is a property of the material and is unaffected by the x-ray source that ejected it. The binding energy of photoelectrons will not change when experiments are conducted with various x-ray sources, but the kinetic energy of the photoelectrons emitted will change as described by equation (4.9).

A series of circumstances leads to an Auger electron. First, a core electron is ejected by an electron beam with enough energy to create a vacancy (see Fig 4.16 (a)). The primary electrons typically have energies between 3 and 30 keV. In order to fill the void, a secondary electron (imaging electron) with a higher energy falls down (see Fig 4.16 (b)). This secondary electron then emits enough energy to eject a tertiary electron (Auger electron) from a higher shell (see Fig 4.15 (c)).

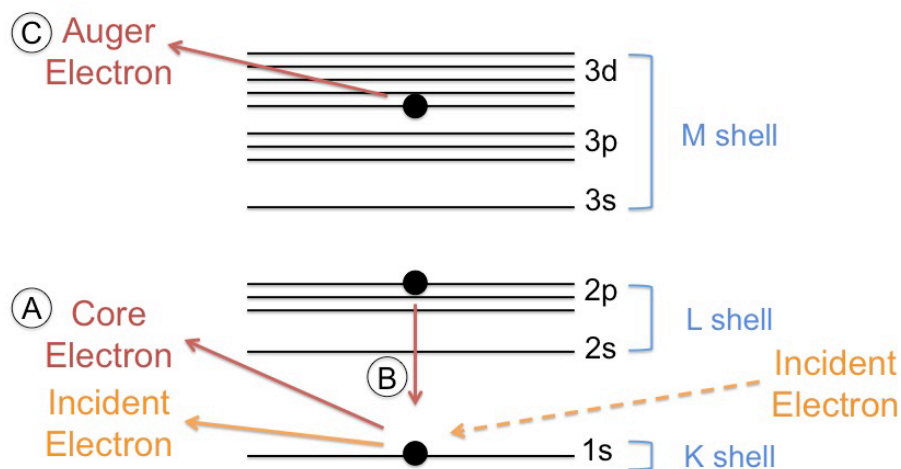


Fig. 4.16: Schematic representation of Auger process [4.17]

4.5.3 Peak Identification

X-ray peak identification A key component in determining the composition of elements and chemical states of a material's surface is photoelectron spectroscopy (XPS). When a sample is exposed to X-rays, XPS analyses the binding energies of the electrons that are released from the sample. The characteristic binding energies of each element and chemical state are used to identify the elements and compounds in the sample.

4.5.4 Instrumentation and Data Collection

A Thermo ESCALab 250Xi spectrometer, as show in Fig. 4.16 below, was used to collect photoelectron emission spectra of the ZnO nanowires. The ESCALab 250Xi makes use of monochromatic Al K_{α} X-rays (wavelength = 1486.7 eV) at a beam diameter size of 900 μm and high-resolution spectral energy resolution of 20 eV. This instrument is hosted by NMISA, Pretoria RSA. The C 1s peak was used as energy scale calibration throughout all measurements. This peak is used, as the C 1s species at 285 eV emanate from hydrocarbon contamination on the sample

surface. All ZnO NW samples were analysed in the as-synthesised state, without extra sample cleaning or preparation.

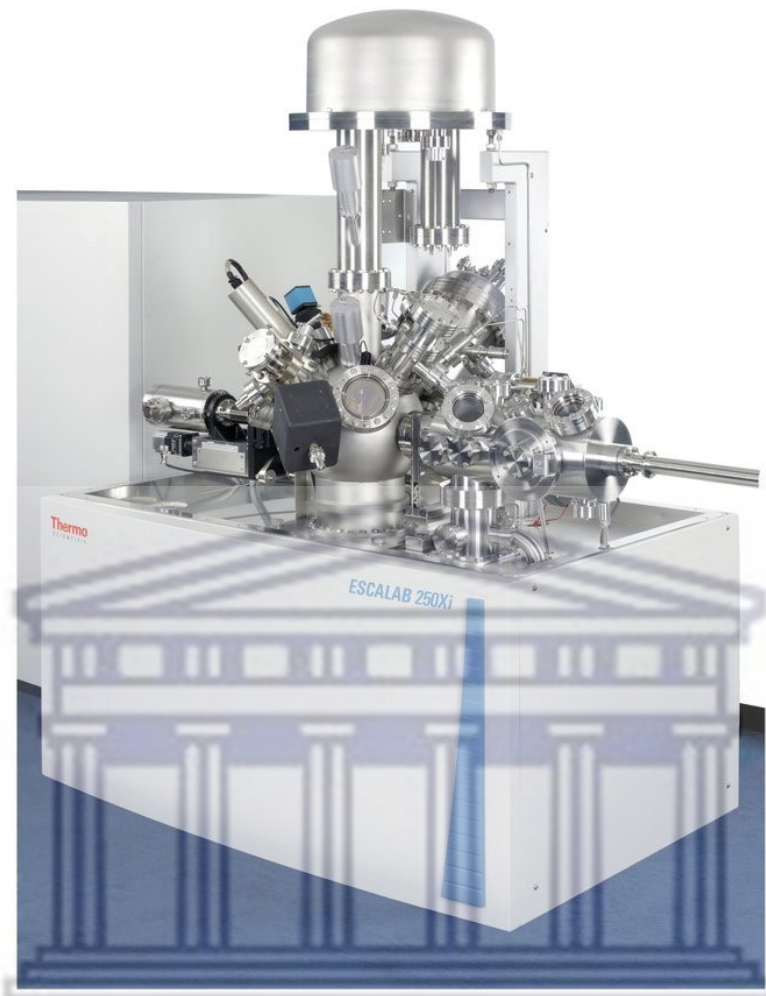


Fig. 4.16: Thermo ESCALab 250Xi XPS spectrometer, hosted by NMISA, Pretoria RSA

References

- [4.1] P.J. Goodhew, J. Humphreys and R. Beanland, (2001) *“Electron Microscopy and Analysis, 3rd Ed”*, Taylor and Francis, New York, USA
- [4.2] L. Reimer, *“Scanning Electron Microscopy: Physics of Image Formation and Microanalysis”*, *Measurement Science and Technology* 11 (2000) 1826; DOI: <https://doi.org/10.1088/0957-0233/11/12/703>
- [4.3] T. Klein, E. Buhr, C. G. Frase, *“TSEM: A Review of Scanning Electron Microscopy in Transmission Mode and Its Applications”*, *Advances in Imaging and Electron Physics* 171 (2012) 297–356; DOI: <https://doi.org/10.1016/B978-0-12-394297-5.00006-4>
- [4.4] P. W. Hawkes, *“Ernst Ruska: Obituary”*, *Physics Today* 43 (1990) 84 – 85; DOI: <https://doi.org/10.1063/1.2810640>
- [4.5] A. V. Girao, G. Caputo and M. C. Ferro *“Application of Scanning Electron Microscopy: Energy Dispersive X-Ray Spectroscopy (SEM-EDS)”* *Comprehensive Analytical Chemistry* 75 (2017) 153 – 168; DOI: <https://doi.org/10.1016/bs.coac.2016.10.002>
- [4.6] P. Sciau, *“Transmission Electron Microscopy: Emerging Investigations for Cultural Heritage Materials”*, *Advances in Imaging and Electron Physics* 198 (2016) 43 – 67; DOI: <https://doi.org/10.1016/bs.aiep.2016.09.002>
- [4.7] J. Liu, *“Advances and Applications of Atomic-Resolution Scanning Transmission Electron Microscopy”* *Microscopy and Microanalysis* 27 (2021) 943 – 995; DOI: <https://doi.org/10.1017/S1431927621012125>
- [4.8] J. M. Thomas, *“The Birth of X-ray Crystallography”*, *Nature* 491 (2012) 186 – 187; DOI: <https://doi.org/10.1038/491186a>
- [4.9] H. P. Myers, (1997) *“Introductory Solid State Physics, 2nd Ed”*, Taylor & Francis, London United Kingdom; DOI: <https://doi.org/10.1201/9780429320286>
- [4.10] W. D. Callister Jr and D. G. Rethwisch, (2018) *“Materials Science and Engineering: An Introduction, 10th Ed”* Wiley, New Jersey USA
- [4.11] M. Picollo, M. Aceto and T. Vitorino, *“UV-Vis Spectroscopy”*, *Physical Sciences Reviews* 4 (2019) 20180008; DOI: <https://doi.org/10.1515/psr-2018-0008>

- [4.12] M.R. Sharpe, *“Stray Light in UV-Vis Spectrophotometers”* Analytical Chemistry 56 (1984) 339A - 356A; DOI: <https://doi.org/10.1021/ac00266a003>
- [4.13] A. Cosimo and H. Claudia, *“UV/VIS Spectrophotometry: Fundamentals and Applications”* Mettler-Toledo (2015) ME-30256131
- [4.14] Z. Chen and T.F Jaramillo, *“The Use of UV-visible Spectroscopy to Measure the Band Gap of a Semiconductor”* , Edited by B. Brunshwig 19/09/2017
- [4.15] F.A Stevie and C.L Donley, *“Introduction to X-ray Photoelectron Spectroscopy”* J. Vac. Sci. Tech. A 38 (2020) 063204; doi: <https://doi.org/10.1116/6.0000412>
- [4.16] J. F Watts and J. Wolstenholme, *“Introduction to Surface Analysis by XPS and AES”*; doi: <https://doi.org/10.1002/0470867930>
- [4.17] M.V Pavan and A.R Barron, *“Auger Electron Spectroscopy”*,
[https://chem.libretexts.org/Bookshelves/Analytical_Chemistry/Physical_Methods_in_Chemistry_and_Nano_Science_\(Barron\)/01%3A_Elemental_Analysis/1.14%3A_Auger_Electron_Spectroscopy#:~:text=Auger%20electron%20spectroscopy%20\(AES\)%20is,ray%20photoelectron%20sp](https://chem.libretexts.org/Bookshelves/Analytical_Chemistry/Physical_Methods_in_Chemistry_and_Nano_Science_(Barron)/01%3A_Elemental_Analysis/1.14%3A_Auger_Electron_Spectroscopy#:~:text=Auger%20electron%20spectroscopy%20(AES)%20is,ray%20photoelectron%20sp) , [Accessed on 14/04/2023]



CHAPTER FIVE

Results and Discussion

5.1 Introduction

This chapter will summarise the major findings of this study. The results of the experimental and characterisation methods discussed in Chapter 2 and 3 will be systematically presented to demonstrate the optimisation of the $\text{MAPbI}_{3-x}\text{Cl}_x$ perovskite film morphology on the ZnO nanowire array. In Chapter 5.1, the inconsistent, non-repeatable nature of high-pressure autoclave hydrothermal synthesis will be investigated and presented to show the need for a facile, upscalable synthesis technique. Chapter 5.2 will present the technique developed in this study and show the consistent trends in the nanowire structure upon changes in the experimental conditions. The optimised experimental conditions for obtaining a consistent perovskite film thickness, grain size, minimal pin-holes and other structural imperfections, will be shown. In Chapter 5.3, the morphology of the $\text{MAPbI}_{3-x}\text{Cl}_x$ layers will firstly be investigated on commercial aluminium-doped zinc oxide (AZO) substrates, followed by study of the growth on nanowire arrays with different structural features, such as diameter, length and areal distribution.

5.2 Characterisation of the Aluminium-doped Zinc Oxide Substrate

Characterisation of the commercial aluminium-doped zinc oxide (AZO) substrate (MSE Supplies LLC, USA) is important as it does not only act as a support, but also provides the ZnO seed layer required to initiate direct epitaxial growth of the nanowires. Fig. 5.1 (a) and (b) show SEM micrographs of the AZO substrate from which the crystal grain size (or diameter) and film thickness were measured. From the cross-sectional view in Fig. 5.1 (b), a film thickness of 890.6

nm was measured, and from the histogram in Fig. 5.1 (c), the AZO grain size with a mean value of 174.64 nm and standard deviation of 71.53 nm was determined. The AZO grain size is important since it controls the nanowire diameter and packing density during growth [5.1], whereas the nanowire length is determined by competition between depletion of Zn²⁺ ions in the precursor solution and stacking of Zn (II) complexes (equations 2.3 to 2.5 of Chapter 2) along the polar faces.

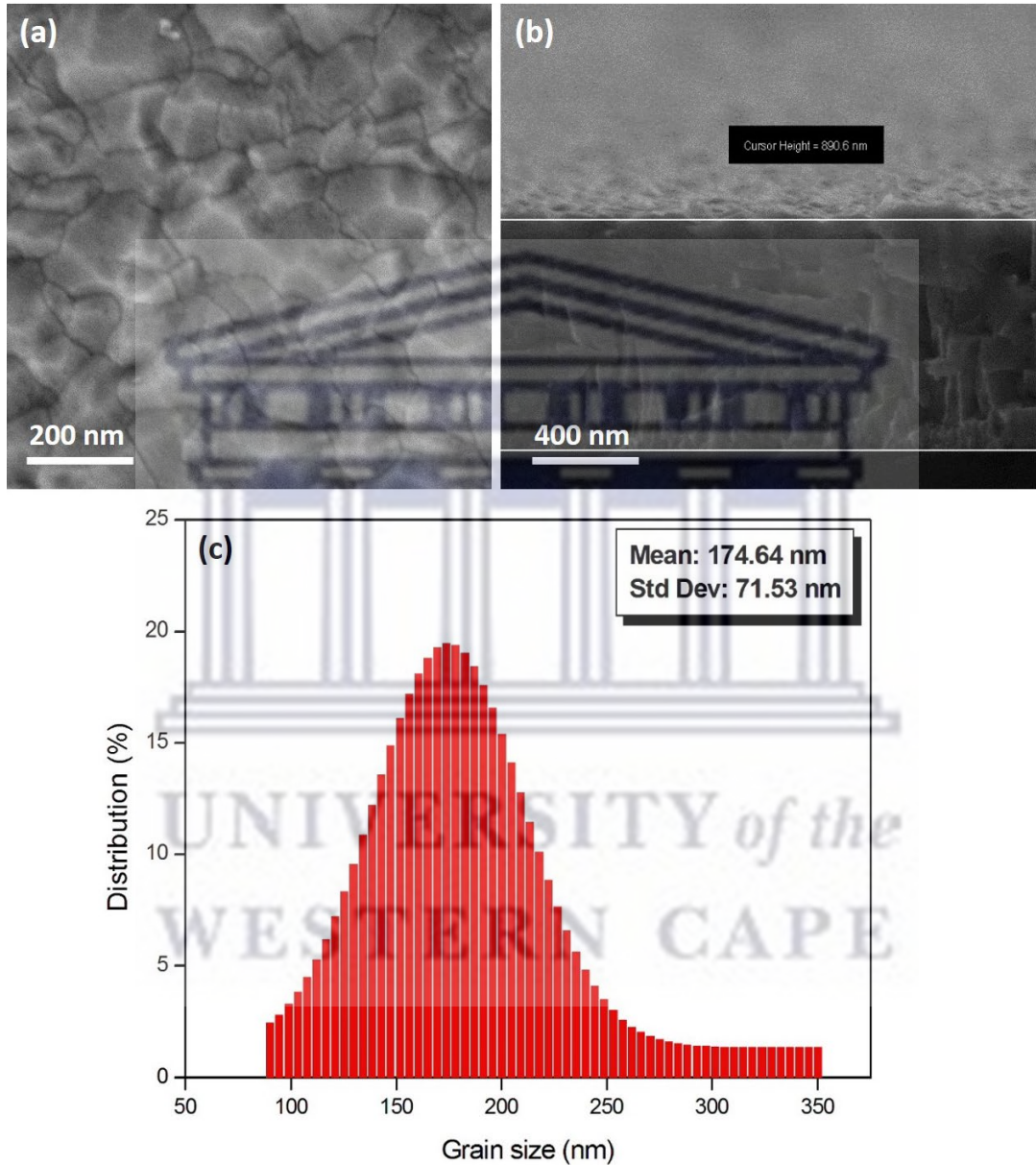


Fig. 5.1: (a) Top-view and (b) Side-view SEM micrographs of the as-bought AZO substrate; (c) histogram showing the diameter distribution of the AZO crystal grains

Fig. 5.2 (a) shows a representative EDS spectrum of the AZO substrate and secondary electron image containing the spot from which the spectrum emerges. In total 20 spots analysed and the averaged elemental composition determined. As shown by the table in Fig 5.2 (a), the substrate contains 1.62 ± 0.19 at% Al. The variance of the Zn:O ratio from 1:1 is due to the fact that no oxygen or zinc standards were run during the EDS analysis. Instead, the preset factory semi-quantitative analysis routine was performed during analysis. This said, an Al concentration between 1 and 2 at% is within the ballpark figure for commercial AZO substrates [5.2].

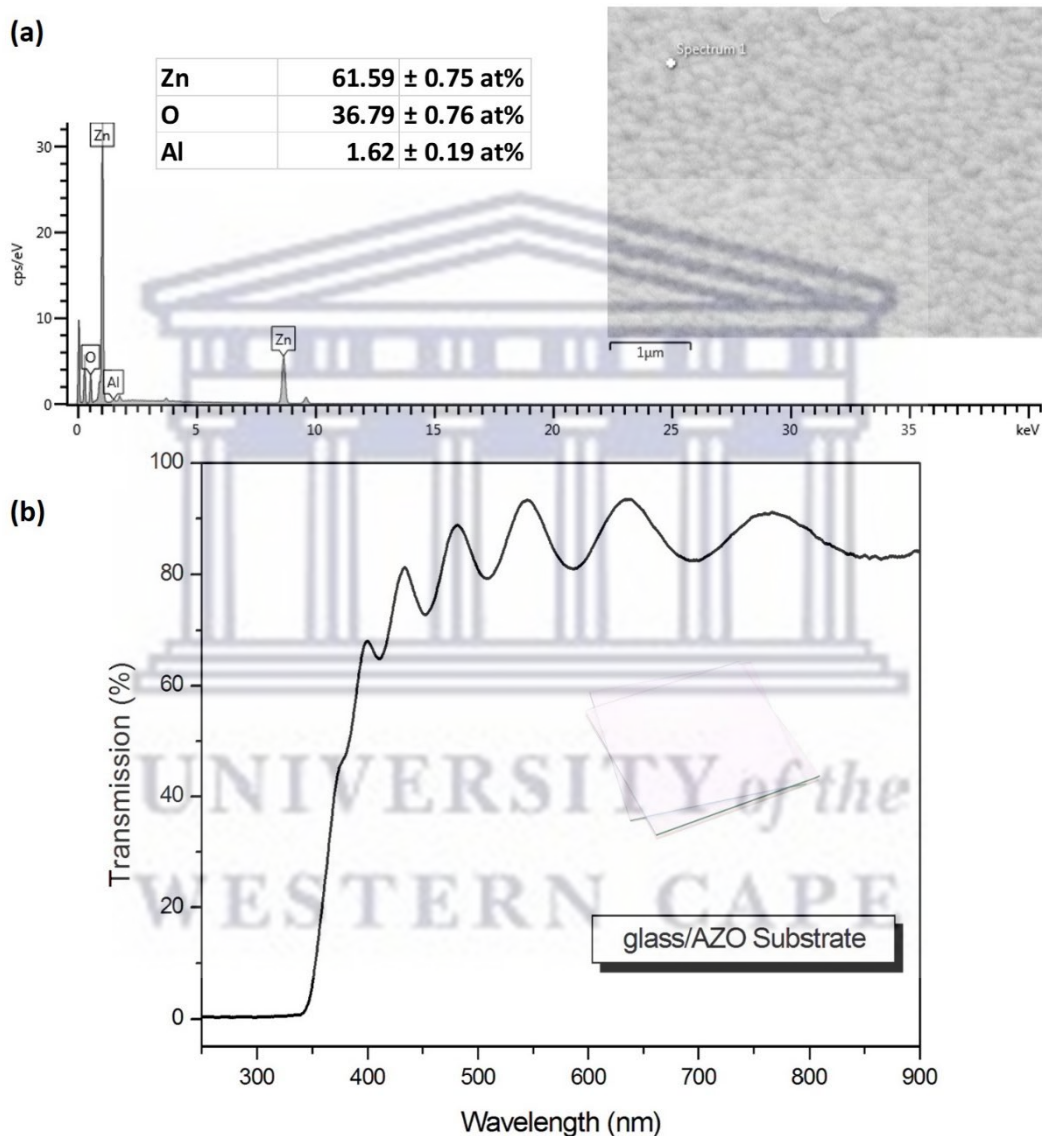


Fig. 5.2: (a) EDS data and (b) UV-Vis transmission spectra of the commercial AZO substrate

The UV-Vis spectrum of Fig. 5.2 (b) shows transmittance above 85% and the presence of interference fringes in the visible region. These interference fringe patterns arise due to multiple reflections at the front (AZO and air) and back interface (AZO and glass) of the film. The frequency and depth of the fringes are controlled by the film thickness and optical constants such as the refractive index and extinction coefficient of the layer [5.3]. High transmittance is very important for solar cell application as the AZO must allow for maximum light transmission; failure to do so will result in low light absorption in the perovskite layer, ultimately leading to low photocurrent generation and an overall inefficient device.

Fig. 5.3 shows an XRD pattern of the commercial AZO, in which the Miller indices of the diffracting planes are indexed against each noticeable peak. The peak indexing was done using crystallographic information from the Joint Committee on Powder Diffraction Studies (JCPDS), with reference from [5.4]. From the pattern, it is determined that the AZO crystallises in the hexagonal Wurtzite crystal structure, discussed in Chapter 2.1. Using Bragg's Law (Chapter 4.3) the d-spacings of the (100), (002), (101), (102), (110), (103) and (112) planes are calculated as 0.281, 0.259, 0.247, 0.191, 0.162, 0.148 and 0.138 nm, respectively. The relationship between the interplanar spacing, d , lattice constants (a and c) and Miller indices (hkl) for the hexagonal crystal is given by:

$$\frac{1}{d^2} = \frac{4}{3} \left(\frac{h^2 + hk + k^2}{a^2} \right) + \frac{l^2}{c^2} \quad (5.1)$$

From equation (5.1) the lattice constants $a = 0.325$ nm and $c = 0.519$ nm were calculated, yielding a c/a ratio of 1.598. This value is lower than the theoretical ratio of 1.66 for hexagonal lattices and is attributed to compressive strain along the c -axis of the AZO film, as discussed by *Jun et al.* [5.5].

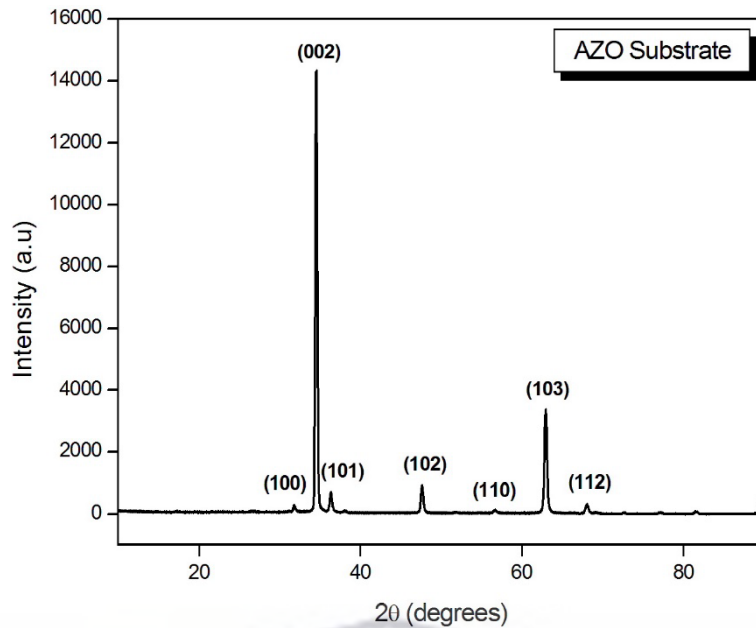


Fig. 5.3: XRD pattern of commercial AZO substrate

5.3 High-Pressure Autoclave Synthesis of ZnO NW Arrays on AZO Substrates

5.3.1 Effect of Synthesis Time on NW Morphology

Fig. 5.4 shows top-view SEM images of the ZnO NW samples synthesised according to the experimental conditions summarised in Table 2.1 of Chapter 2. In this series of experiments, the synthesis time was increased to 1, 3 and 8 hours, while keeping the $\text{Zn}(\text{NO}_3)_2 \cdot 6\text{H}_2\text{O}$ and HMTA in an equimolar ratio of 1:1 (1.75 mmol in 100 ml solution) and a synthesis temperature of 90 °C. The samples were subsequently named NW-AC 1h, NW-AC 3h and NW-AC 3h, respectively to indicate the changes in synthesis time. Parameters that are important for well-defined NWs are the nanowire diameter and packing density. The latter describes the number of wires occupying a specific surface area and is important when used as an electron transport layer in photovoltaics. Generally, an even nanowire coverage, with good interspacing is required, as it allows for sufficient penetration of the perovskite layer [5.6]. As shown in Fig. 5.4, after 1hr of synthesis

densely packed, hexagonally shaped structures form with a diameter of 160.73 ± 36.94 nm, which is similar to that of the AZO grains, shown in Fig. 5.1 (c). From this micrograph it appears that the nanowire growth was still at the initial stages of formation. With the increase in synthesis time up to 3hrs, the NW structure becomes more defined and an average nanowire diameter of 134.08 ± 24.49 nm measured - in some areas, clear nanowire structures can be observed. Increasing the synthesis time to 8hrs, however, yields bigger diameter structures, densely packed and poor defined nanowire structure. In all cases, the hexagonal shaped structures, predicted by the growth model discussed in Chapter 2.3 and 2.4 are observed. From these results, a clear optimised synthesis time of 3 hours was established and used in the next series of experiments.

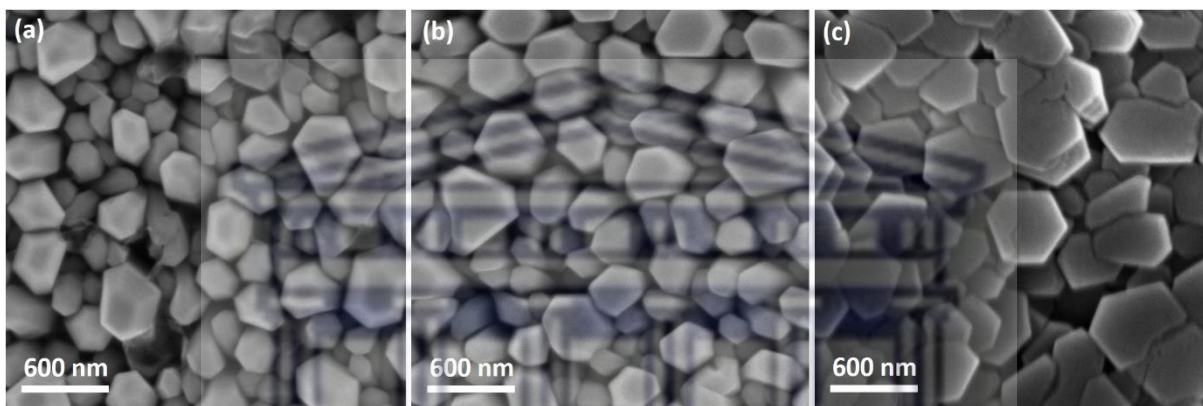


Fig. 5.4: SEM micrographs of (a) NW-AC 1h, (b) NW-AC 3h and (c) NW-AC 8h

5.3.2 Effect of Synthesis Temperature on NW Morphology

Fig. 5.5 shows the SEM images of the structures formed at autoclave chamber temperatures of 90, 100 and 110 °C, as summarised in Table 2.2 of Chapter 2. These samples are correspondingly labelled NW-AC 90, NW-AC 100 and NW-AC 110. From the SEM micrographs it is noticed that NWs form at each condition, however when the temperature is increased from 90 °C to 110 °C, an increase in the size of nanowires is observed, and is in accordance with Mohammadi and Ghasemi [5.7]. This shows the reduction rate of metal ions increased by temperature, high temperatures lead to high reaction kinetics. It is also observed that the higher the temperature the denser the NW packing. From equation 2.7 in Chapter 2, the decrease of hydroxide shows

that high temperature speeds up the condensation process and favour the formation of ZnO. As such, to avoid dense packing an increased nanowire size, from this set of experiments, a preferred temperature of 90 °C was selected.

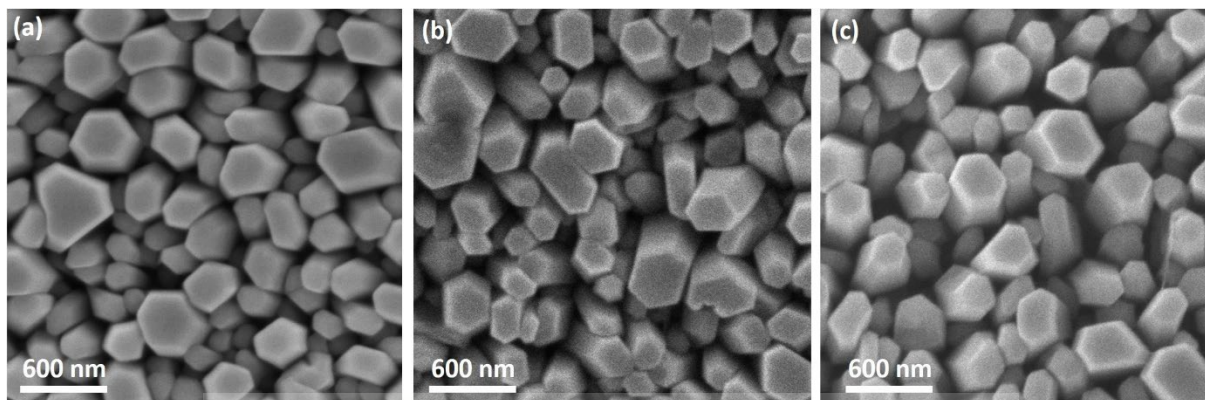


Fig. 5.5: SEM micrographs of (a) NW-AC 90, (b) NW-AC 100 and (c) NW-AC 110

5.3.3 Effect of Precursor Concentration on NW Morphology

Table 2.3 of Chapter 2 summarises the different ratios of zinc nitrate-to-HTMA used experimentally. Fig. 5.6 shows SEM micrographs of samples NW-AC 25M, (b) NW-AC 50M and (c) NW-AC 70M, which contain a ratio of 25, 50 and 70 mmol.l⁻¹ of zinc nitrate and HTMA in solution. As shown, the different concentrations visibly affected the shape and microstructure of the nanowires. When the NWs were synthesised at a low equimolar solution and growing temperature of 90°C, increasing duration growth time does not have an impact on the shape of the nanowires. More defined ZnO nanowires were observed for a solution concentration of 70 mM. The hydrothermal method tends to produce highly increased density nanowires under any given conditions, some of the nanowires end up overlapping one another, which leads to the breakage of the wires and change in the orientation. It was found that increasing precursors concentration leads to increased density and nonalignment of hexagonally structured nanowires [5.8].

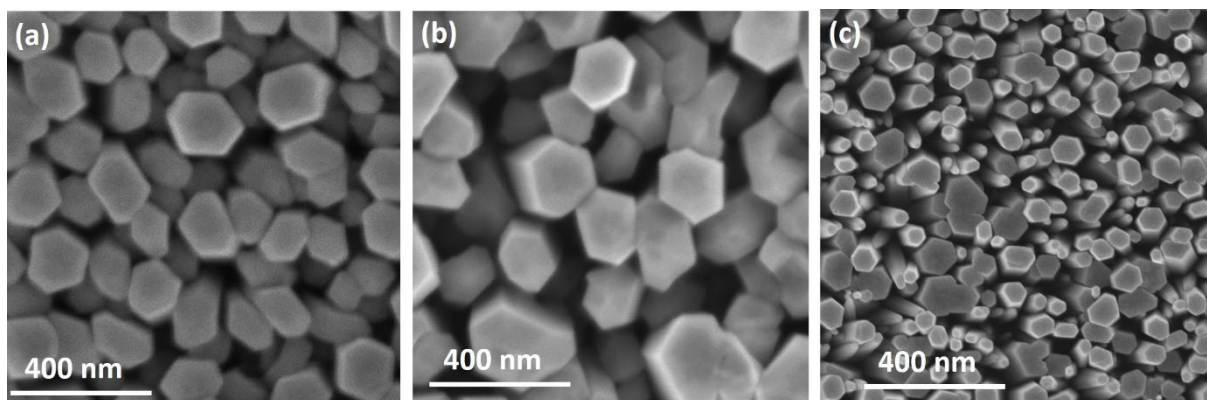


Fig. 5.6: SEM micrographs of (a) NW-AC 25M, (b) NW-AC 50M and (c) NW-AC 70M

One of the challenges of using the hydrothermal method is the curing temperature. After the reaction, the Teflon liner and the solution take time to reach room temperature, which may affect the reaction time and sometimes the substrates end up with the formation of unwanted structures. Akgun *et al.* [5.9] found that the longest ZnO nanowires were obtained at a HMTA/Zinc acetate dihydrate ratio of 1. In a solution where the actual concentration of NH_3 is lower than the nominal concentration, excess $(\text{CH}_2)_6\text{N}_4$ provides sufficient amounts of OH^- ions for the growth of ZnO nanowires. The best results were achieved with NW-AC 25M and NW-AC 70M. The experiment was repeated with the same condition and different results were obtained. This is due to high supersaturation level, which favours nucleation. Hence, the study was conducted to investigate the morphology of zinc oxide nanowires using a different method, which is discussed below.

5.4 Chemical Bath Synthesis of ZnO NW Arrays on AZO Substrates

5.4.1 Effect of Synthesis Time on NW Morphology

Fig. 5.7 shows SEM micrographs of samples (a) NW-CB 1h, (b) NW-CB 3h and (c) NW-CB 8h fabricated under conditions summarised in Table 2.4 of Chapter 2. Vertically aligned ZnO nanowires were formed on the AZO substrate exhibiting hexagonal shape at the tips, which is

associated with the wurtzite structure. Fig. 5.7 (a) depicts that ZnO nanowires with different lengths were formed in 1 hour of experimentation, whereas image (b) shows that ZnO nanowires that are tightly packed were formed, with some nanowires overlapping/suppressing one another. As the time of experiment was increased, it is shown that nanowires were formed with the hexagonal structures and a small hexagonal shape on top. It appears that at longer synthesis times, zinc highly ionises in solution, causing the Zn^{2+}/OH^{-} ratio to be higher, leading to high etching rate of the nanowires, leading to the smaller nanowire diameters observed.

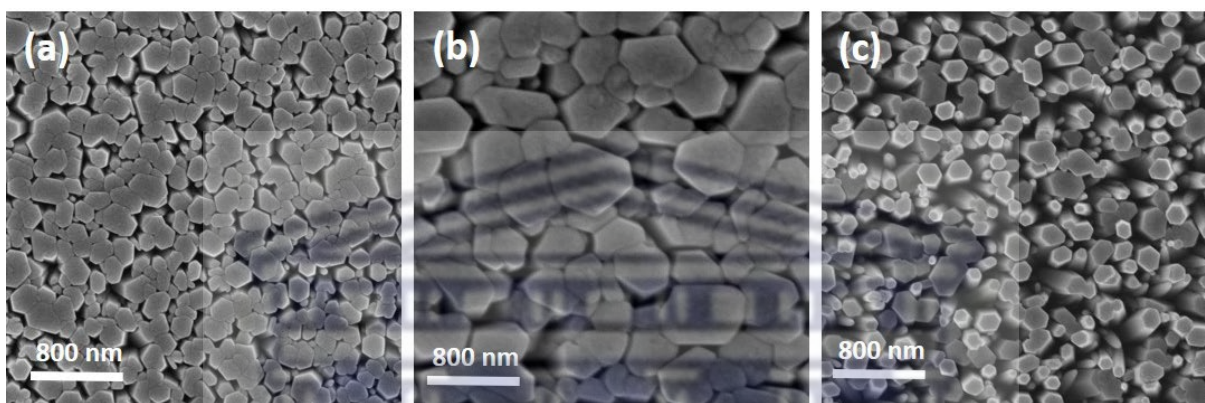


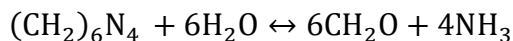
Fig. 5.7: SEM micrographs of (a) NW-CB 1h, (b) NW-CB 2h and (c) NW-CB 3h

5.4.2 Effect of Synthesis Temperature on NW Morphology

SEM observation in Fig. 5.8 shows the correlation between the surface microstructure and growth temperature. The surface microstructure of the ZnO NW film profoundly changed with varying temperature. ZnO nanowires exhibiting hexagonal wurtzite structure were formed in all the conditions. Image (a) and (b) shows that nanowires with high packing density were formed. Image (c) shows that nanowires with a different shape were formed. The surface morphology varied in shape with increasing growth temperature as shown in Fig. 5.8. The increase in temperature may cause biaxial film stress. This stress is caused by the imbalance between the substrate and the film thermal expansion coefficients following high-temperature deposition [5.11]. Due to the potential interaction between point defects and threading dislocations, the

low temperature may be advantageous for reducing stress. Changing the growth temperature improved ZnO grain sizes, however at the highest temperature of 110 °C, ZnO structural quality was affected, and this may be due to change in thermal expansion.

Temperature has a significant impact on the formation, growth, and structural maintenance of hexagonal ZnO nanowires. The influence of temperature on ZnO nanostructure nucleation and growth can be explained by looking at equation 2.1 in Chapter 2:



which shows that seven moles of reactants result in ten moles of products, raising the temperature of the reaction will cause more HMTA to hydrolyse and will cause the equilibrium to advance along with an increase in entropy [5.12]. It is evident that rising temperatures make Zn ions more mobile and promote ZnO nucleation to reduce their free energy.

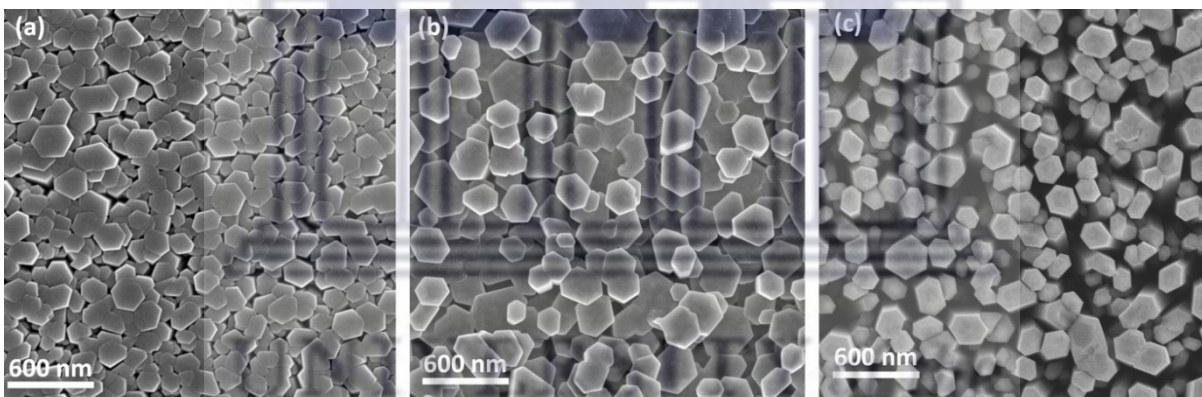


Fig. 5.8: SEM micrographs of (a) NW-CB 90, (b) NW-CB 100 and (c) NW-CB 110

5.4.3 Effect of Synthesis Concentration on NW Morphology

Sample NW-AC 1-25, fabricated at low precursor equimolar solution at 90 °C, is shown in Fig. 5.9(a): low density and hexagonally shaped nanowires were formed at this condition. Increasing the concentration of the precursors affected the shape of ZnO nanowires causing them to be

more of prism shaped. The addition of PEI to the solution enhanced the diameter definition of the nanowires and the shape. The heterogeneous growth of ZnO NWs on the polycrystalline AZO glass substrate is favoured by the addition of PEI, which suppresses the homogeneous growth in aqueous solution by presumably forming PEI-Zn (II) ion complexes. Image (a) and (b) shows the best conditions that is used to fabricate ZnO nanowires.

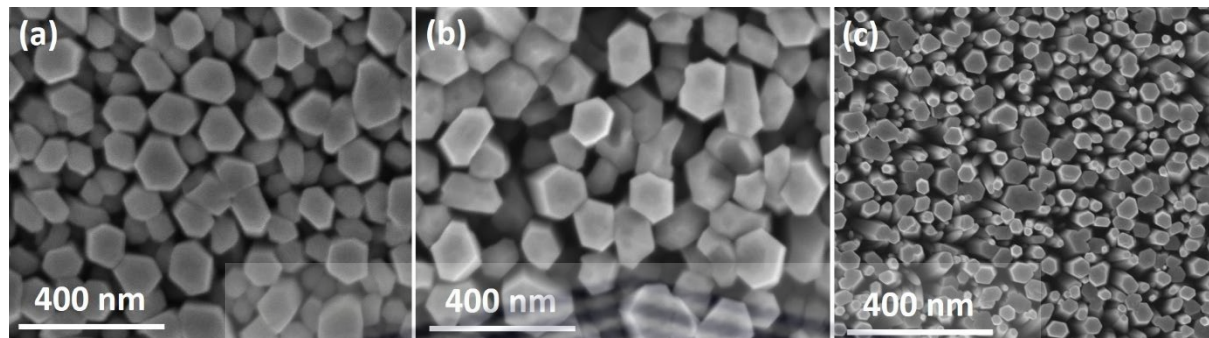


Fig. 5.9: SEM micrographs of (a) NW-CB 1-25, (b) NW-CB 2-50 and (c) NW-CB 3-70

5.5 Structural and Optical Characterisation of Chemical Bath Synthesised ZnO NWs

The XPS survey scan of Fig. 5.10 (a) confirms the presence of the Zn 2p peak at 1022 eV and oxygen (O) 1s peak at 531 eV. The C 1s peak at 285 eV is due to hydrocarbon contamination, which is common for samples exposed to air over extended periods [5.13]. The C 1s peak was used as the energy scale calibration for all measurements. As shown in Fig. 5.10 (b), the Zn 2p_{3/2} and Zn 2p_{1/2} core lines of the ZnO crystal are located at 1021.81 and 1045.05 eV, respectively. Fig. 5.10 (c) shows the deconvolution of the O 1s core spectrum. The presence of three peaks are identified: the main peak (green line) at 530.00 eV is attributed to Zn-O lattice bonding; the second, broader peak (red line) at 531.2 eV is due to C-O and a small, wide peak (blue line) at 532.7 eV is assigned to C=O bonding [5.14]. The latter bonds are assigned to hydrocarbon surface contamination as identified in the survey scan. No Al signal could be detected in the survey scan, which is explained by the surface characterisation nature of XPS: a depth profile analysis is required, but unavailable at the time of measurement. The peak fitting and associated bonding

quantification are shown in Fig 5.10 (d). From the fitted data it was found that the Zn 2p and O 1s (metal oxide) concentrations were 20.1 and 13.0 at% respectively, which yields a Zn:O ratio of 1.55:1. This disparity from an ideal ratio of 1:1 is attributed to the presence of oxygen vacancies on the surface of the ZnO NWs [5.13, 5.14].

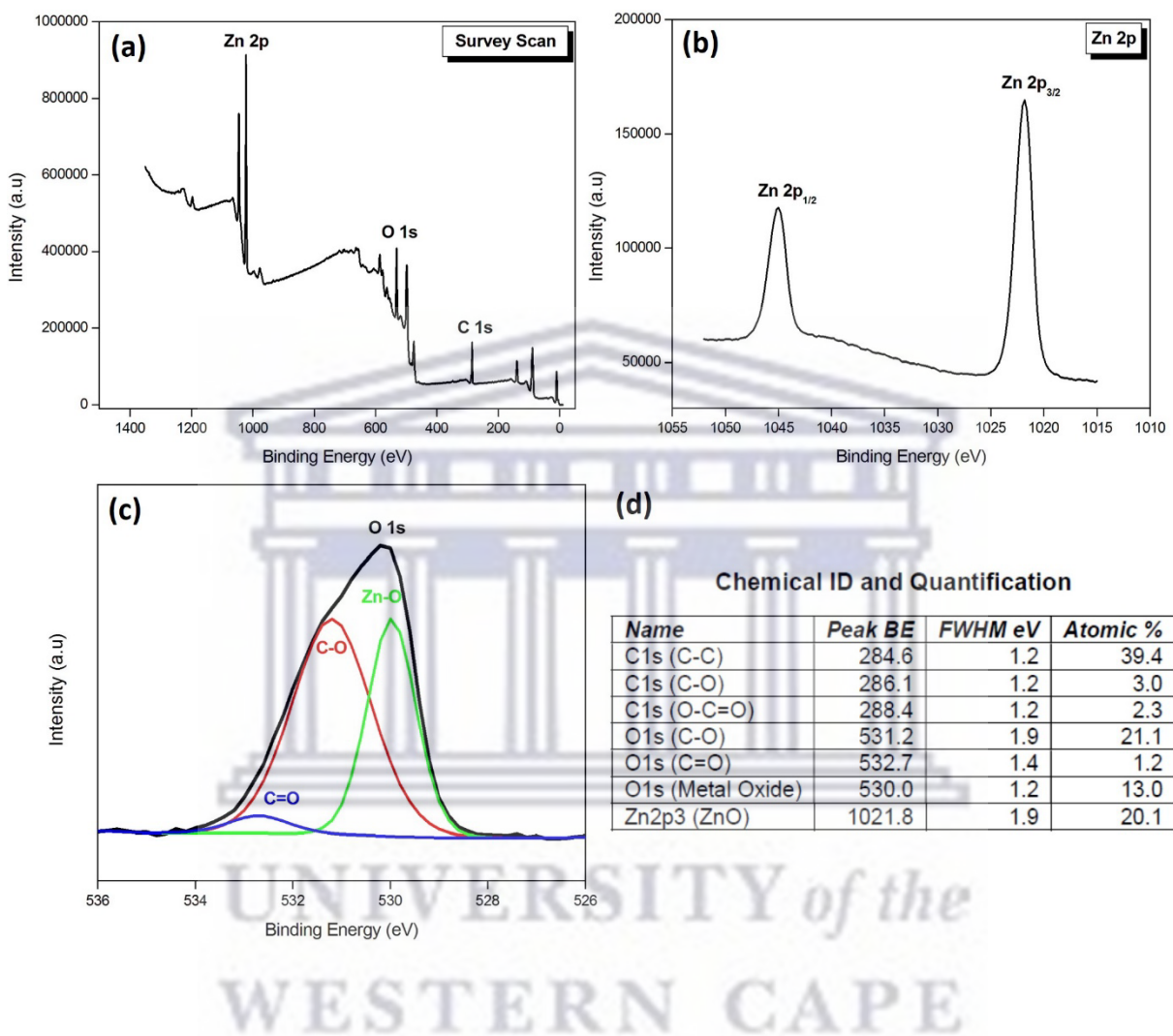


Fig. 5.10: (a) XPS survey scan, (b) high resolution scan of (b) Zn 2p and (c) O 1s line profiles, and (c) summary of the chemical identification and quantification

To determine whether the NWs are indeed Al-doped, HR-TEM and STEM, coupled with high-resolution EDS mapping were employed. Fig. 5.11 (a) shows a bright-field TEM micrograph of a single ZnO NW synthesised at the best condition, as discussed in Section 5.5. From this image, the hexagonally shaped wurtzite apex of the NW can be observed once more. The high-resolution image of Fig. 5.11 (b) shows the $(10\bar{1}1)$ lattice planes on the sides of the ZnO NW and has an interplanar spacing of 0.249 nm. This is in accordance with the model discussed in Chapter 2. 4, with the $(10\bar{1}1)$ plane being part of the non-polar $\{0\bar{1}\bar{1}0\}$ family of planes. The indexed SAED pattern of figure (c) shows the major diffracting planes of a single nanowire, and is similar to the XRD pattern of the AZO substrate shown in Fig. 5.3. This shows that the NWs maintain the same crystal structure of the AZO seed layer, in accordance with the epitaxial growth models discussed in Chapter 2.

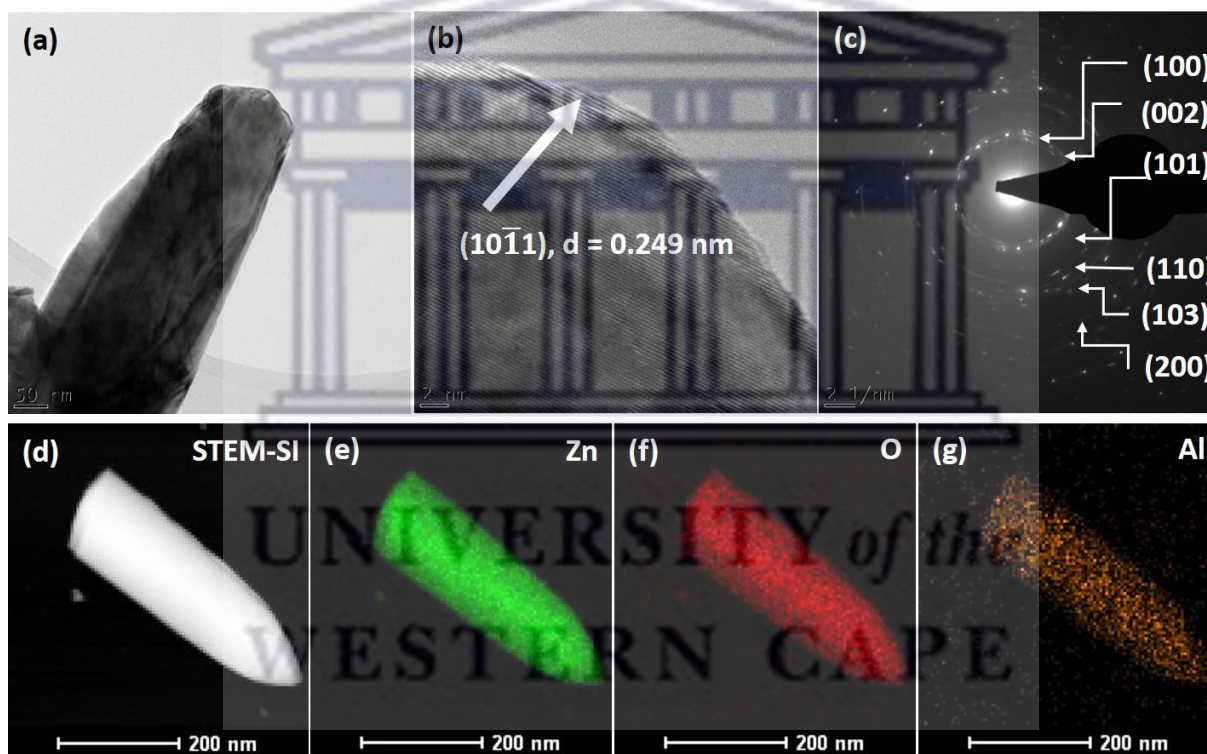


Fig. 5.11: (a) Bright-field and (b) high-resolution micrographs of a single NW; (c) corresponding SAED pattern; (d) STEM spectral image, with extracted EDS maps of (e) Zn, (f) O and (g) Al

The STEM spectral image of Fig. 5.11 (d) contains elemental information about the NW. This image was collected at a TEM magnification of 160 000x over a total scan area of 300 x 300 nm². This area was divided into 100 x 100 pixels, with each pixel analysed for 100 ms, collecting both secondary electrons (used for imaging) and x-rays, used for elemental composition during EDS analysis. The EDS maps are displayed in Fig. 5.11 (e) to (g), with Zn, O and Al clearly detected. From the quantification, an Al concentration of less than 0.5 at% was determined. This shows that individual nanowires are indeed Al doped, after synthesis from the AZO substrate.

Fig. 5.12 compares the UV-Vis transmission spectra of a ZnO NW array to the commercial AZO substrate, analysed in Section 5.2. As shown, there is minimal loss in transmission, with the nanowire layer showing transmission above 80% in the visible to IR region. The slight loss in transmission and shift of the absorption edge (~350 nm) are ascribed to the presence of oxygen vacancies, as shown by the XPS results of Fig. 5.10. These states cause recombination centres just below the conduction band edge within the bandgap [5.11].

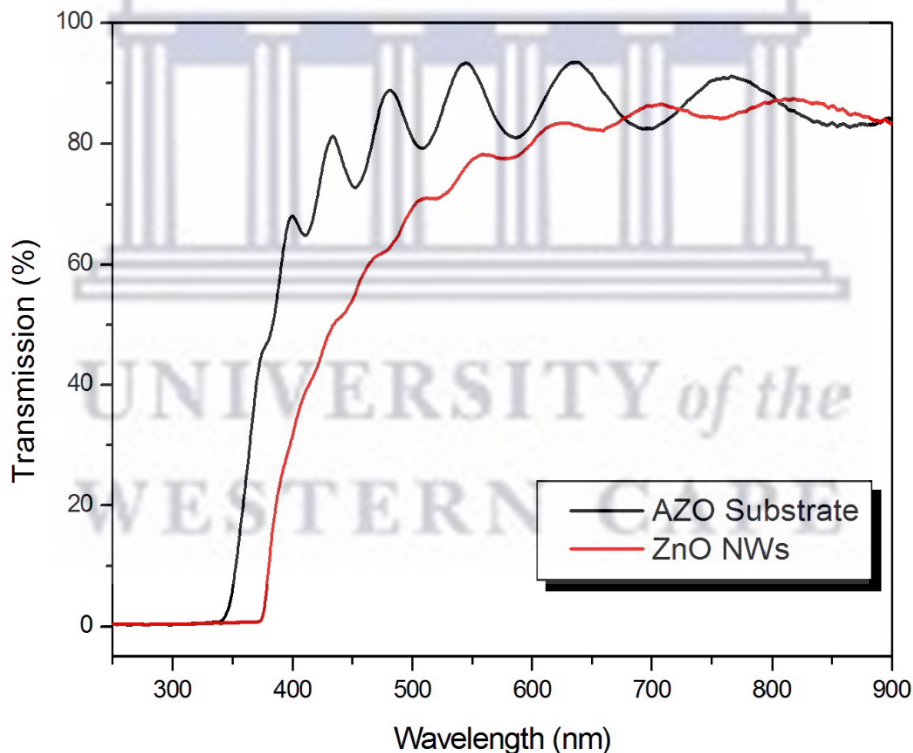


Fig. 5.12: UV-Vis transmission spectra comparison between AZO substrate and AZO/ZnO NWs layer

5.6 Optimisation of Perovskite Spin-Coating Conditions

5.6.1 Effect of Spin Rate and Time on Perovskite Morphology

Fig. 5.13 shows MAPbI_{3-x}Cl_x layers spin-coated on a ZnO nanowire film synthesised at the best hydrothermal conditions, as discussed in Chapter 5.4. From the top-row of images in Fig. 5.13, the perovskite layer spin-coated at 2000 rpm has a better film coverage than the one spin coated at 1000 rpm and 3000 rpm. Furthermore, from the bottom the perovskite spin coated for 60 s shows better coverage and a better-defined grain size. As such, spin-coating at 2000 rpm for 60 s produces better results as it will result in thicker films with a full coverage on the substrate, larger crystallites, and increased porosity. Post spin-coating all samples were annealed for 2 hours at 90 °C, according to the supplier (Ossila) instructions.

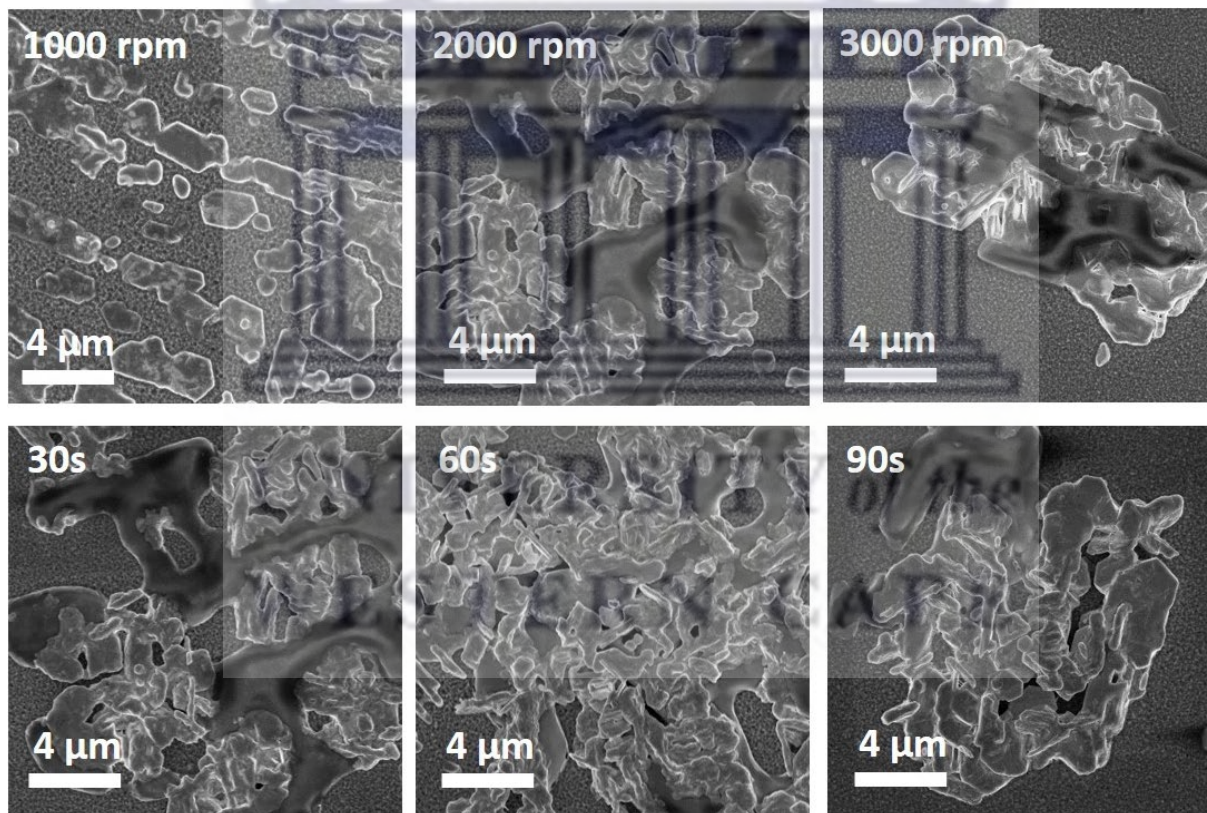


Fig. 5.13: *Top Row:* SEM micrographs showing the effect of spin-rate; *Bottom Row:* effect of spin-coating time on MAPbI_{3-x}Cl_x thin film formation on a ZnO NW layer

5.6.2 Effect of Annealing Temperature and Time on Perovskite Conversion and Morphology

Annealing is a critical step in the fabrication of perovskite layers as it significantly impacts the conversion of the perovskite precursor materials into the desired perovskite phase and morphology, as discussed in Chapter 3. Moreover, the substrate type and film thickness affect the optimal annealing conditions [5.15, 5.16]. Fig. 5.14 shows the effect of annealing temperature and time on the morphology of the spin-coated perovskite layers; these layers were spin-coated for 60s at 2000rpm, established in section 5.6.1.

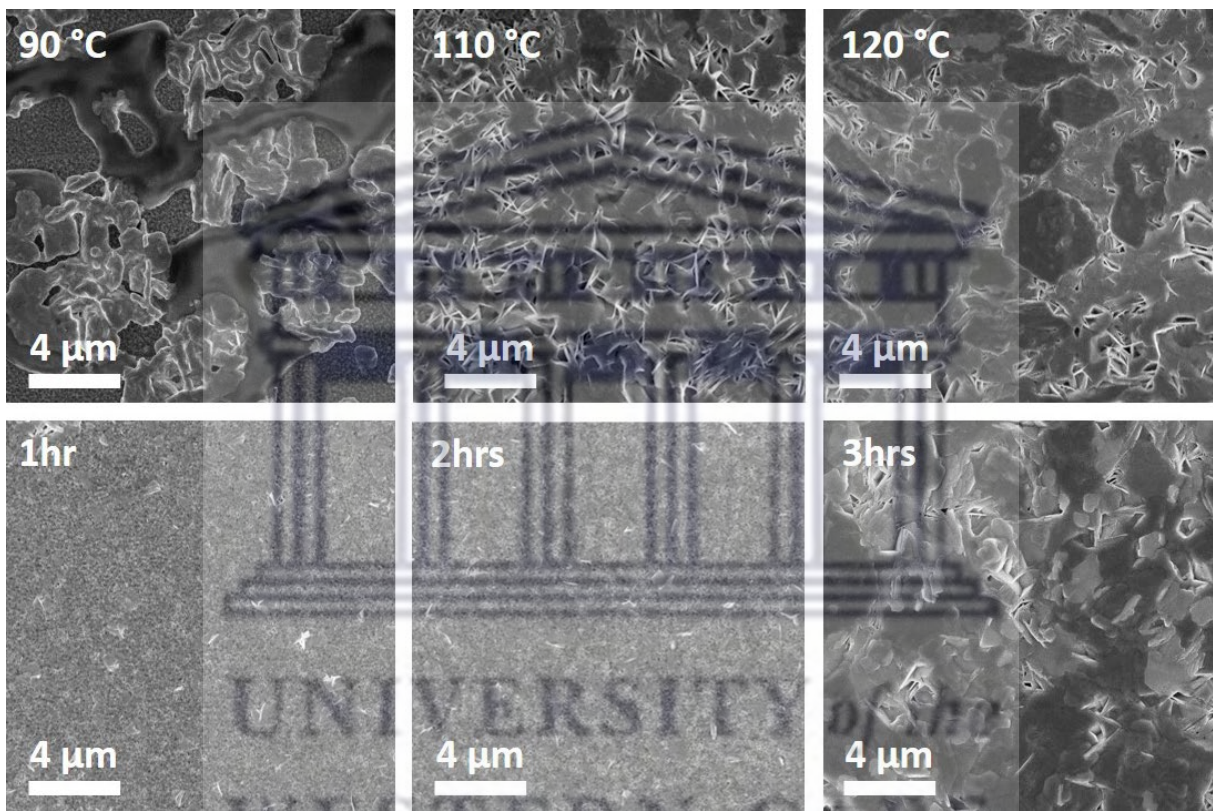


Fig. 5.14: Effect of annealing temperature and time on $\text{MAPbI}_{3-x}\text{Cl}_x$ conversion on NW array substrate

The top row of Fig. 5.14 shows the resultant morphology when increasing the temperature from 90 to 120 °C at a fixed annealing time of 2 hours. By exploring the results in Fig. 5.14, increasing the annealing temperature results in much better coverage and a decrease in the number of

pores (pin-holes) in the film, causing bigger grain sizes. It is also observed that the perovskite crystallisation increases as the annealing time increases from 1 to 3 hours at a fixed annealing temperature of 90 °C. From these experiments, it was determined that the best conditions for perovskite deposition and conversion are:

- dynamic spin-coating at 2000 rpm
- spin-coating time: 60s
- annealing temperature: 120 °C
- annealing time: 3 hours

At the above conditions, the Pb:I:Cl ratios were calculated using EDS data. More than 30 different spots were analysed. Fig. 5.15 shows a representative area and spectrum, along with the averaged semi-quantitative composition. From these results it may be observed that the Pb:I:Cl is in a ratio of 1: 1.96: 1.04. Of course, this does not confirm the crystalline nature of the thin films nor the stoichiometric relationship between the different ions, but do give an indication of the relative composition, namely $\text{MAPbI}_{1.96}\text{Cl}_{1.04}$ (where $x = 1.04$). To confirm the crystallinity, XRD diffraction is required; these results will be discussed below.

A chlorine molar concentration of 1.04 compares favourably with that reported by Nggoloda *et al.* [5.17], who showed an optimised molar ratio for $\text{MAPbI}_{3-x}\text{Cl}_x$ of Pb:Cl:I of 1: 1.89: 1.11, with $x = 1.11$ when depositing thin films using sequential chemical vapour deposition. However, these are gross overestimates as density functional theoretical calculations, supported by experimental diffraction and quantification studies by Colella *et al.* [5.18] show that Cl can exist as a doping agent in the $\text{MAPbI}_{3-x}\text{Cl}_x$ lattice at a maximum theoretical limit of about 4 at% or $x = 0.12$. This implies that the excessive chlorine concentrations measured during the EDS experiments may originate from unreacted PbCl_2 as well as other chlorine rich phases. The existence of these phases may explain the difficulty in converting the MAI and PbCl_2 into mixed halide perovskite form on a nanowire substrate as discussed in section 5.6.1.

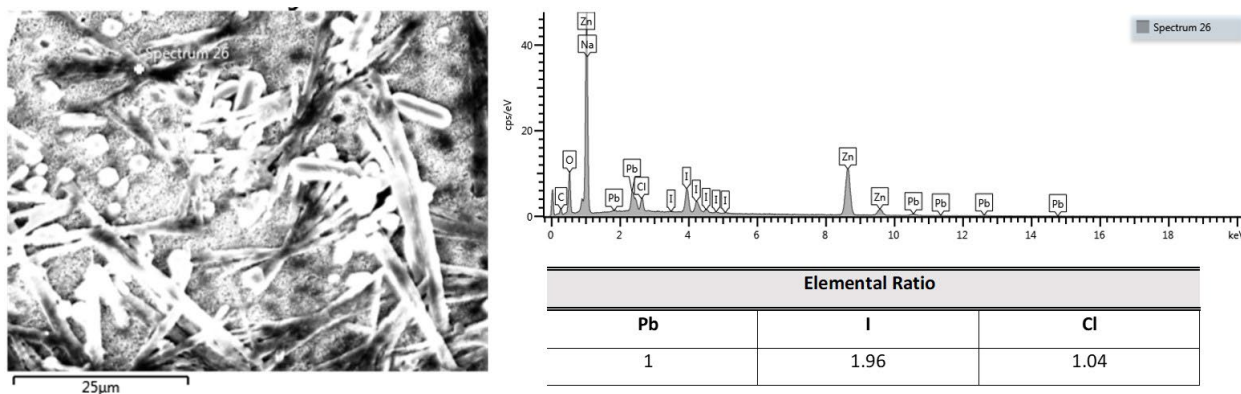


Fig. 5.15: EDS analyses of the Pb:Cl:I ratios for a perovskite layer deposited and converted at the optimised spin-coating and annealing conditions

5.7 Spin-coating and Conversion of Perovskite Layers on Different Nanowire Morphologies

Fig. 5.16 shows top- and side-view SEM images of $\text{MAPbI}_{3-x}\text{Cl}_x$ layers deposited on ZnO nanowire arrays with different morphologies, synthesised at different chemical bath conditions. The perovskites were spin coated and converted at the optimised conditions found in sections 5.6.1 and 5.6.2, namely a dynamic spin-rate at 2000 rpm, spin-coating time of 60s and annealing temperature and time of 120 °C and 3 hours, respectively. The blue-enclosed block of images shows a better surface coverage with minimised pore size when depositing the perovskite layer on a NW array synthesised for 3hours. From the green-enclosed block of micrographs, it was observed that increasing the temperature from 90°C to 120°C increases the grain size of perovskites, as well as that the shape of the produced perovskite film to be significantly influenced by the annealing temperature. This is a preferable for solar cell applications, as Wie et al found that millimetre-scale crystalline grains, deposited by a solution-based hot-casting approach produced 18% solar cell efficiency [5.16]. It was further observed from the yellow-enclosed block of images, that perovskite deposition on 70 mM synthesised nanowires have a better surface coverage than 25 mM, due to the high porosity and well-defined nanowire architecture shown in Fig. 5.8 (c).

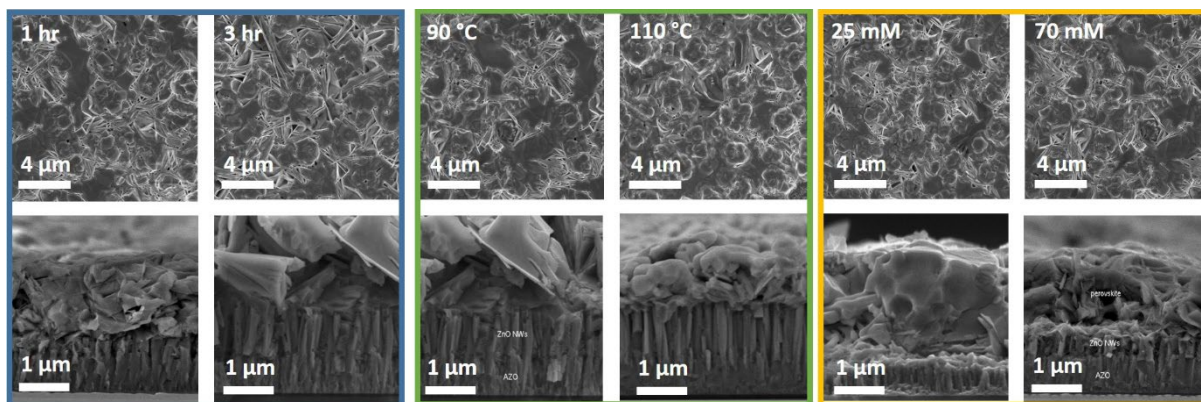


Fig. 5.16: MAPbI_{3-x}Cl_x thin film morphology after conversion on substrates with different NW morphology

MAPbI_{3-x}Cl_x has the same crystal structure as the undoped MAPbI₃ lattice. MAPbI₃ crystallises in orthorhombic, tetragonal and simple cubic unit cells, with the two main phases at solar cell operational temperatures being the tetragonal and cubic phases. Of these, the tetragonal phase is preferable for high photon absorption, but destabilises into the cubic structure below 54 °C [5.19]. Subtle differences exist between these two phases, caused by a slight rotation of the PbI₆ octahedra along the c-axis. The unit cells of these two crystal structures of MAPbI₃ are shown in Fig. 5.17 [5.20].

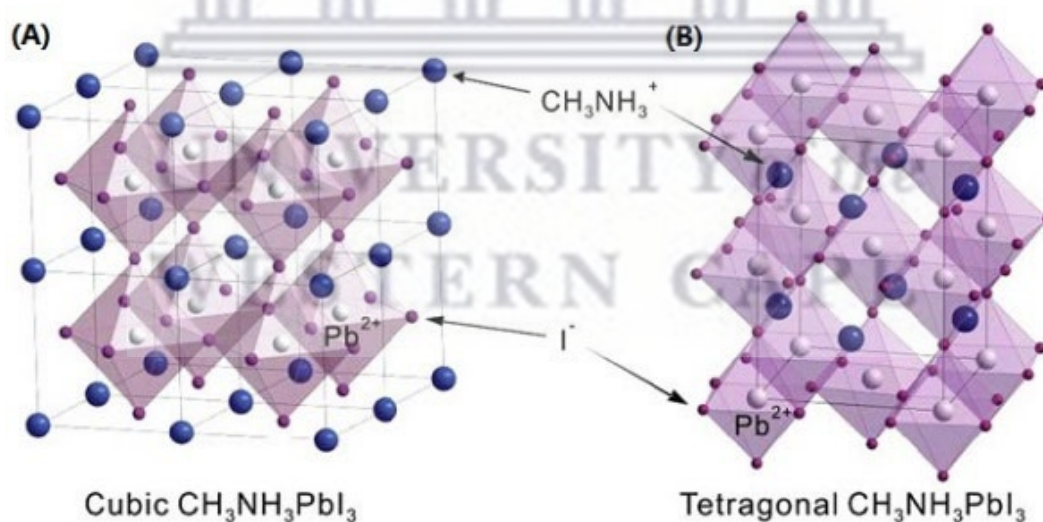


Fig. 5.17: Unit cells of (a) cubic and (b) tetragonal MAPbI₃ [5.20]

The tetragonal phase exists as a pseudo-cubic structure with $a^* = \frac{a}{\sqrt{2}}$ and $c^* = \frac{c}{2}$. At 54 °C, the cubic phase of MAPbI₃ transforms into the tetragonal phase and at 100 °C, the tetragonal phase converts back into the cubic phase [5.21]. The XRD patterns of these two phases are shown in Fig. 5.18. During transformation, the cubic (100) peak splits into tetragonal (002) and (110); the (110) into (112) and (200) and the cubic (200) into tetragonal (004) and (220); in addition, new (211) and (213) peaks also appear at 2θ of 23.5 and 31°, respectively. The peak splitting is usually used as indicator for phase transformation, with the MAPbI_{3-x}Cl_x showing a preference for the cubic phase of MAPbI₃, but with growth along the cubic (100) and (200) directions [5.21].

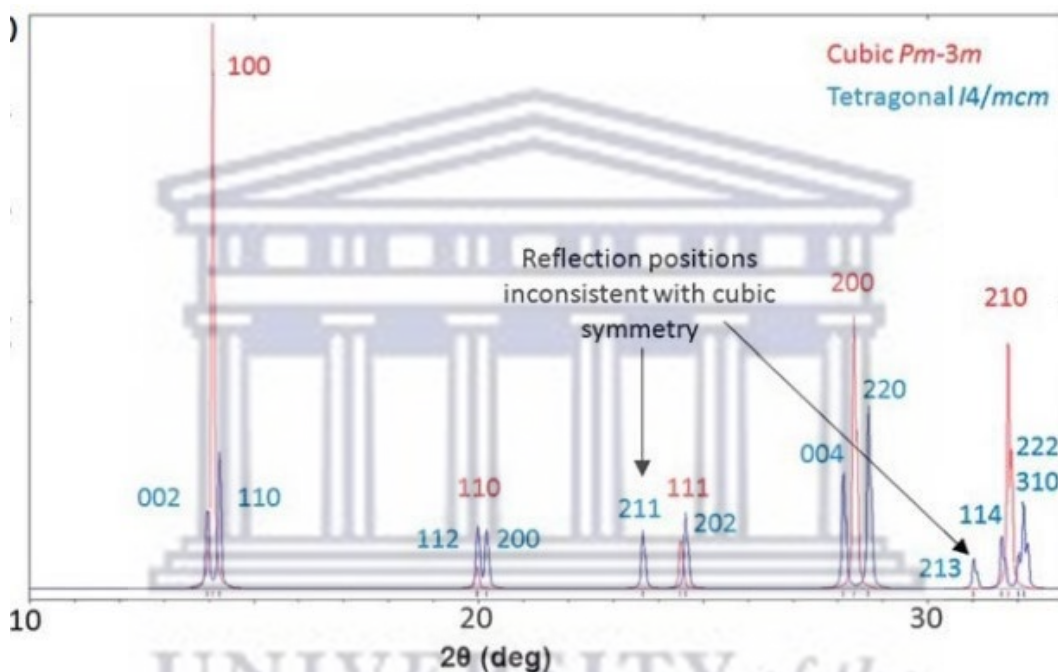


Fig. 5.18: XRD pattern of cubic (red) and tetragonal (blue) MAPbI₃ [5.21]

Fig. 5.19 show the XRD pattern of the ZnO NWs without a deposited perovskite layer with the (100), (002), (101) and (102) diffraction peaks located at 2θ values of 31.83°, 34.51°, 36.32° and 47.66°. From these peaks the crystal structure of the ZnO NWs is determined as Wurtzite, with a lattice constant $a = 0.324$ nm and $c = 0.520$ nm, according to equation (5.1). The diffraction pattern of the perovskite layer converted on a NW array synthesised with the chemical bath for 1 and 3hr respectively. The SEM images are shown in Fig. 5.7 (a) and (c) respectively.

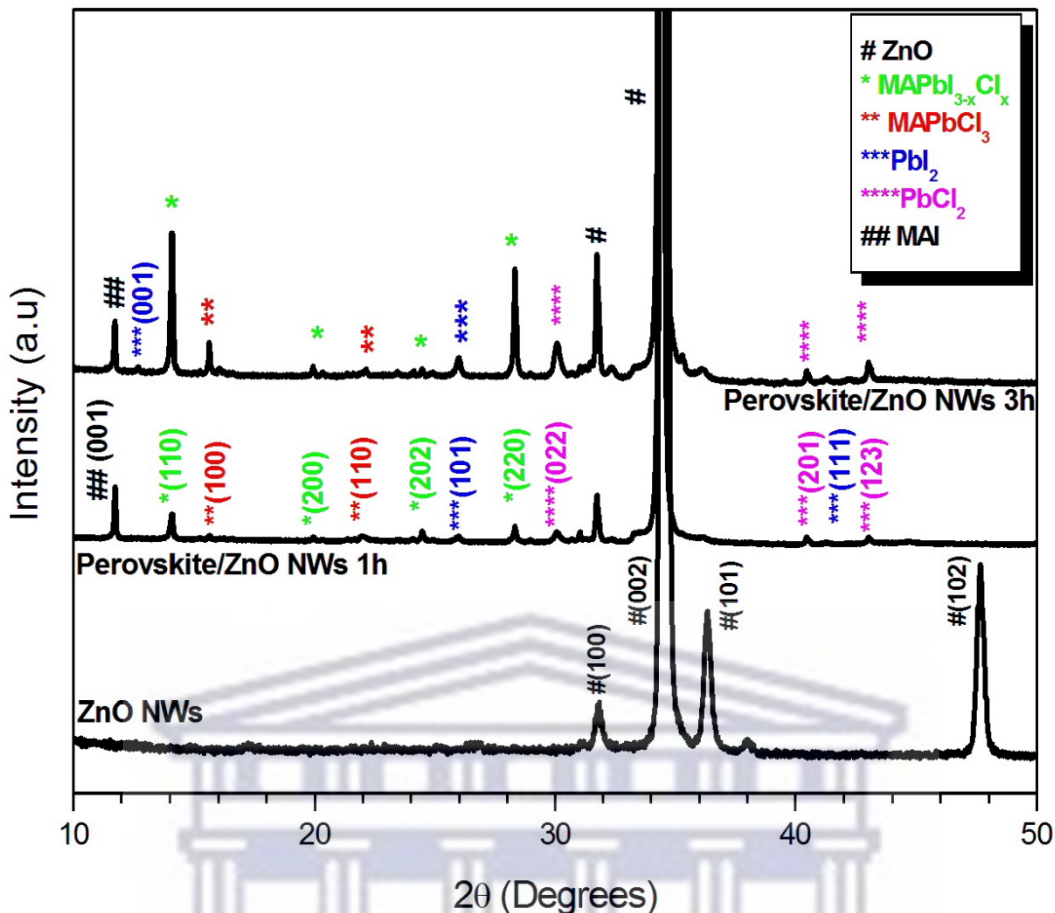


Fig. 5.19: XRD patterns ZnO NWs and MAPbI_{3-x}Cl_x thin films deposited on a ZnO NW array grown for 1hr and 3 hrs

From the 1hr sample, the MAPbI_{3-x}Cl_x diffraction peaks are observed at 2θ values of 14.11°, 19.94°, 24.52° and 28.33° corresponding to the (110), (200), (202) and (220) planes [5.21]. Also observed are diffraction from MAPbCl₃ (100) at 15.61° and (110) at 21.99°, unreacted PbI₂ at 30.10°, 40.47° and 43.03° corresponding to (022), (201) and (123) planes, respectively; as well as MAI (001) at 11.74°. Further diffraction from PbI₂ (101) is detected at 25.95° [5.20]. The PbCl₂ diffraction is explained by the presence of unconverted PbCl₂ precursor, whereas the MAPbCl₃ is due to chlorine and iodine phase segregation during annealing. As discussed in Chapter 3.7, the constituent chlorine and iodine ions choose the weakest bonding interactions and eventually configure in the least energetically favourable configuration. These result in the formation of heterogeneous chlorine and iodine rich nucleation sites instead of homogeneous nucleation. The

PbI₂ and MAI phases form at the higher annealing temperature of 120 °C according to equation (3.3) of Chapter 3. In comparison, the XRD pattern of the perovskite layer converted on a 3hr synthesised NW array shows much more intense diffraction peaks from all the phases identified in the 1hr sample. This shows that the underlying substrate morphology has a significant impact on the crystallisation kinetics of the perovskite layer. The SEM images of Fig. 5.7 clearly showed that the nanowire structure is better defined after 3hrs of synthesis, with high porosity and clear nanowire definition, which offers better intercalation of the perovskite layer during spin-coating deposition. At a fixed annealing temperature and time, the only influence in the crystallisation kinetics arise from the difference in thermal conductivity from the hot-plate surface, through the respective nanowire morphologies, to the wet perovskite layer.

There are four factors that affect the rate at which heat is conducted through a material ($\frac{dQ}{dt}$), namely the thermal conductivity of the material (k), the cross-sectional area of the material transferring heat (A), the difference in temperature between one side of the material and the other (dT) and the thickness of the material (l). These can be summarised as follows [5.22]:

$$\frac{dQ}{dt} = \frac{kAdT}{l} \quad (5.2)$$

From equation (5.2), it becomes obvious that the physical dimensions of the heat-conducting medium play a major role in the heat transfer rate. If one looks to the SEM micrographs of Fig. 5.7 (a) and (c), as well as the cross-sectional images of the blue-enclosed block of images of Fig. 5.16, the length of the nanowires increases after 3 hours, whereas the effective cross-sectional area (A^*) of the more porous 3hr synthesised nanowire array increases according to the schematic shown in Fig. 5.20 [5.23]. This implies that heat transfer increases as the nanowire array becomes more porous, but decreases with an increase in length. However, the higher porosity of the nanowire array synthesised after 3 hours implies better perovskite intercalation, which means that the wet perovskite layer is in closer contact with the underlying AZO seed layer, as shown by the blue enclosed block of images of Fig. 5.16. As a result, the l value of equation (5.2) also decreases, meaning greater $\frac{dQ}{dt}$ value. The greater heat transfer implies faster perovskite

conversion. The presence of the MAPbCl₃ phase is unwanted for photovoltaics, but is common for mixed halide perovskites deposited via one-step spin-coating [5.18]. During conversion to MAPbI_{3-x}Cl_x, the MAPbI₃ forms first but converts into to MAPbCl₃ after annealing above 100 °C during the first 10 mins [5.21] and then back to MAPbI₃ after 45 mins of annealing. Further annealing would result in the decomposition of MAPbI₃ to PbI₂, but occurs after conversion to the intermediate phase to MAPbI₃ [5.24]. From Fig. 5.19, it appears that the more porous, well-defined nanowire array allows for better nanowire crystallisation of the MAPbI_{3-x}Cl_x structure, but also formation of the MAPbCl₃ phase.

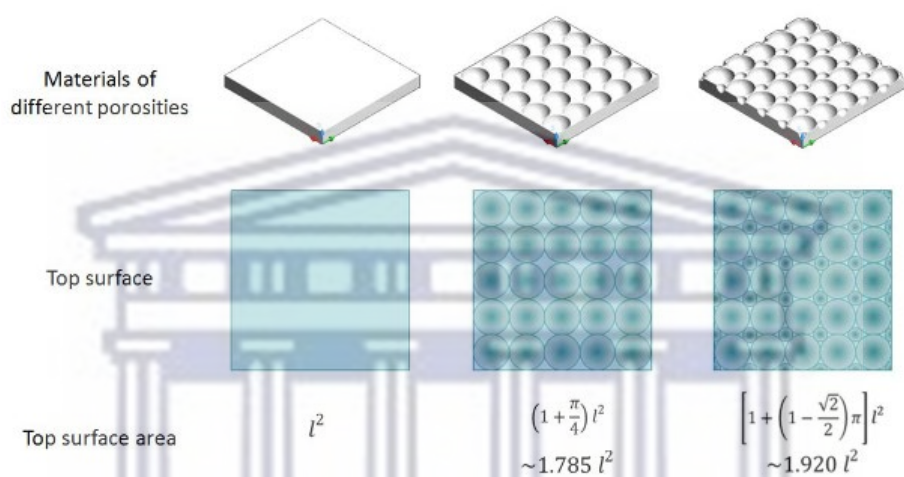


Fig. 5.20: Schematic showing the relation between porosity, surface area [5.23]

The XRD patterns of Fig. 5.21 compare the diffraction of the perovskite layer converted on an array fabricated using the chemical bath method at 90 and 110 °C. The respective SEM micrographs are shown in Fig. 5.8 (a) and (c), with the perovskite layer shown in the green enclosed block of images of Fig. 5.16. Unlike the case in Fig. 5.19, a clear decrease in intensity of the main MAPbI_{3-x}Cl_x phases can be observed for the layer converted on a 110 °C annealed NW array. What is more interesting, however, is the almost complete removal of the MAPbCl₃ phase at 15.61° at 21.99° as well as a decrease in the unconverted MAI and PbCl₂. This may suggest preferable Cl sublimation on this NW array, leading to homogenous nucleation during crystallisation, and subsequent lower unwanted MAPbCl₃ crystals.

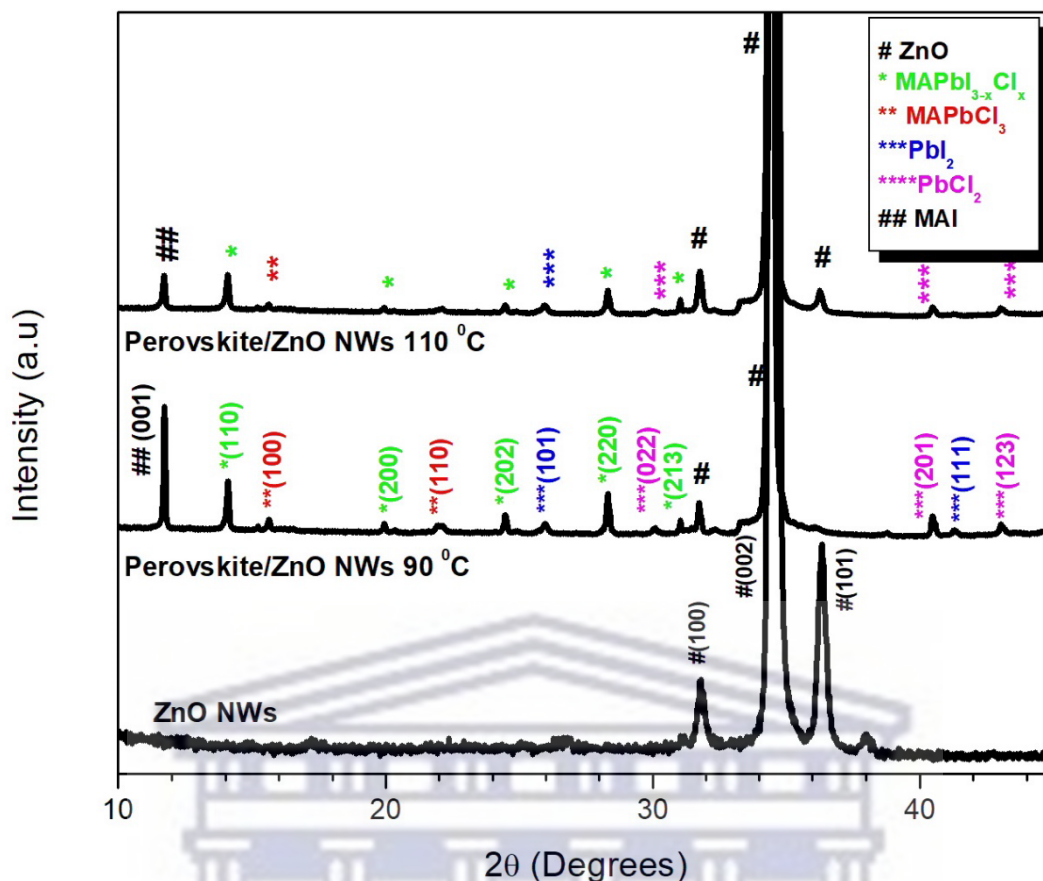


Fig. 5.21: XRD patterns ZnO NWs and $\text{MAPbI}_{3-x}\text{Cl}_x$ thin films deposited on a ZnO NW array synthesised with the chemical bath method at 90 and 110 °C

The XRD patterns of Fig. 5.22 compare the diffraction of the perovskite layer converted on an array fabricated using the chemical bath method at 25 and 70 mM concentration of zinc acetate + HMTA + PEI. The respective SEM micrographs are shown in Fig. 5.9 (a) and (c), with the perovskite layer shown in the blue enclosed block of images of Fig. 5.16. As shown, the crystallinity increases with on the NW array of 70 mM with the $\text{MAPbI}_{3-x}\text{Cl}_x$ much more intense, with a slight decrease in the unwanted chlorine rich phase, as well as the unreacted precursor MAI and PbCl_2 . Again, this can be explained by the faster growth kinetics provided by the more porous, well-defined nanowire architecture synthesised at 70 mM.

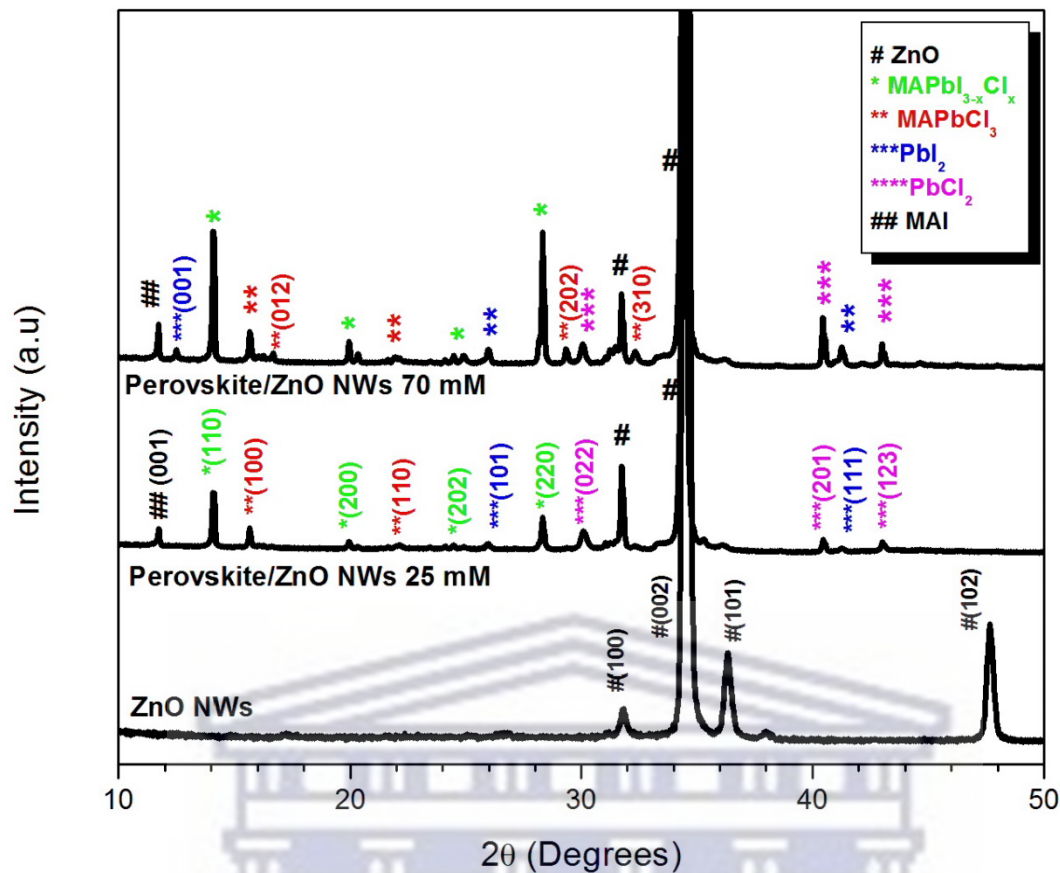


Fig. 5.22: XRD patterns ZnO NWs and MAPbI_{3-x}Cl_x thin films deposited on a ZnO NW array synthesised with the chemical bath method using an equimolar ratio of zinc acetate, HMTA and PEI of 25 mM and 70 mM

The results show that the underlying substrate plays an important role in the perovskite conversion kinetics. In particular, a well-defined, regular ZnO nanowire array allows for fast growth of tetragonal MAPbI_{3-x}Cl_x perovskites, which is uniform with minimal pinholes, compared to a layer grown on a highly dense assortment of nanowires. In addition, the study also showed that it is indeed possible to grow good quality layers of mixed halide perovskite on ZnO nanowire arrays using the one-step spin-coating method. This is in contrast to reports in literature, which often requires an additional deposition of MAI to achieve full conversion during annealing of the thin film.

References

- [5.1] J. Song and S. Lim, "Effect of Seed Layer on the Growth of ZnO Nanorods" J. Phys. Chem. C 111 (2007) 596 – 600; doi: <https://doi.org/10.1021/jp0655017>
- [5.2] Q. C. Bui, V. Consonni, S. Boubenia, et al., "High Figure-of-Merit in Al-doped ZnO Thin Films Grown by ALD through the Al Content Adjustment" Materialia 31 (2023) 101863, doi: <https://doi.org/10.1016/j.mtla.2023.101863>
- [5.3] V. Senay, "Some Physical Properties of Nanostructured Al doped ZnO Thin Films Synthesised by RF Magnetron Sputtering at Room Temperature" Journal of Materials Science: Materials in Electronics volume 30 (2019) 9910 – 9915; doi: <https://doi.org/10.1007/s10854-019-01329-6>
- [5.4] Th. Aeugle, H. Bialas, K. Heneka and W. Pleyer, "Large Area Piezoelectric ZnO Film Transducers Produced by RF. Diode Sputtering" Thin Solid Films 201 (1991) 293 – 304; doi: [https://doi.org/10.1016/0040-6090\(91\)90118-H](https://doi.org/10.1016/0040-6090(91)90118-H)
- [5.5] M.-C. Jun, S.-U. Park and J.-H. Koh, "Comparative Studies of Al-doped ZnO and Ga-doped ZnO Transparent Conducting Oxide Thin Films" Nanoscale Research Letters 7 (2012) 639; doi: <https://doi.org/10.1186/1556-276X-7-639>
- [5.6] D.-Y. Son, J.-H. Im, H.-S. Kim and N.-G. Park, "11% Efficient Perovskite Solar Cell Based on ZnO Nanorods: An Effective Charge Collection System" J. Phys. Chem. C 118 (2014) 16567 – 16573, doi: <https://doi.org/10.1021/jp412407j>
- [5.7] F. M. Mohammadi and N. Ghasemi, "Influence of Temperature and Concentration on Biosynthesis and Characterisation of Zinc Oxide Nanoparticles using Cherry Extract" Journal of Nanostructure in Chemistry 8 (2018) 93 – 102; doi: <https://doi.org/10.1007/s40097-018-0257-6>
- [5.8] Q. Zhou, J. Wen, P. Zhao and W. Anderson, "Synthesis of Vertically-Aligned Zinc Oxide Nanowires and Their Application as a Photocatalyst" Nanomaterials 7 (2017) 9; doi: <https://doi.org/10.3390/nano7010009>

- [5.9] M. C. Akgun, Y. E. Kalay and H. E. Unalan, "Hydrothermal Zinc Oxide Nanowire Growth using Zinc Acetate Dihydrate Salt" *Journal of Materials Research* 27 (2012) 1445 – 1451; doi: <https://doi.org/10.1557/jmr.2012.92>
- [5.10] T. Nakamura, K. Masuko, A. Ashida, T. Yoshimura, & N. Fujimura, "Surface Preparation of ZnO Single-Crystal Substrate for the Epitaxial Growth of ZnO Thin Films" *Journal of Crystal Growth* 318 (2011) 516–518; doi: <https://doi.org/10.1016/j.icrysgro.2010.10.044>
- [5.11] Y. F. Li, B. Yao, Y. M. Lu, *et al.*, "Characterisation of Biaxial Stress and its Effect on Optical Properties of ZnO Thin Films" *Applied Physics Letters* 91 (2007) 021915; doi: <https://doi.org/10.1063/1.2757149>
- [5.12] J. J. Cheng, S. M. Nicaise, K. K. Berggren, S. Gradečak, "Dimensional Tailoring of Hydrothermally Grown Zinc Oxide Nanowire Arrays." *Nano Lett.* 16 2016, 753– 759, doi: <https://doi.org/10.1021/acs.nanolett.5b04625>
- [5.13] M. B. Haider, "XPS Depth Profile Analysis of Zn₃N₂ Thin Films Grown at Different N₂/Ar Gas Flow Rates by RF Magnetron Sputtering" *Nanoscale Research Letters* 12 (2017) 5; doi: <https://doi.org/10.1186/s11671-016-1769-y>
- [5.14] M. C. Biesinger, L. W. M. Lau, A. R. Gerson and R.St.C. Smart, "Resolving Surface Chemical States in XPS Analysis of First Row Transition Metals, Oxides and Hydroxides: Sc, Ti, V, Cu and Zn" *Appl. Surf. Sci.* 257 (2010) 887-898; doi: <https://doi.org/10.1016/j.apsusc.2010.07.086>
- [5.15] N. K. Tailor, M. Abdi-Jalebi, V. Gupta, H. Lu, M. I. Dar, G. Li and S. Satapathi, "Recent Progress in Morphology Optimisation in Perovskite Solar Cells" *Journal of Materials Chemistry A* 8 (2020) 21356 – 21386; doi: <https://doi.org/10.1039/D0TA00143K>
- [5.16] W. Y. Nie, H. H. Tsai, R. Asadpour, *et al.*, "High-Efficiency Solution-Processed Perovskite Solar Cells with Millimetre-Scale Grains" *Science* 347 (2015) 522–525; doi: <https://doi.org/10.1126/science.aaa0472>
- [5.17] S. Ngqoloda, C. J. Arendse, S. Guha, *et al.*, "Mixed-Halide Perovskites Solar Cells Through PbI₂ and PbCl₂ Precursor Films by Sequential Chemical Vapour Deposition" *Solar Energy* 215 (2021) 179 – 188; doi: <https://doi.org/10.1016/j.solener.2020.12.042>

- [5.18] S. Colella, E. Mosconi, P. Fedeli, et al., “MAPbI_{3-x}Cl_x Mixed Halide Perovskite for Hybrid Solar Cells: The Role of Chloride as Dopant on the Transport and Structural Properties” Chem. Mater. 25 (2013) 4613 – 4618; doi: <https://doi.org/10.1021/cm402919x>
- [5.19] Y. Kawamura, H. Mashiyama and K. Hasebe, “Structural Study on Cubic-Tetragonal Transition of CH₃NH₃PbI₃” J. Phy. Soc. Jpn. 71 (2002) 1694 – 1697; doi: <https://doi.org/10.1143/JPSJ.71.1694>
- [5.20] Z. Chen, H. Li, Y. Tang, X. Huang, D. Ho and C.-S. Lee, “Shape-Controlled Synthesis of Organolead Halide Perovskite Nanocrystals and Their Tunable Optical Absorption” Mater. Res. Express 1 (2014) 015034; doi: <https://doi.org/10.1088/2053-1591/1/1/015034>
- [5.21] S. Luo and W. A. Daoud, “Crystal Structure Formation of CH₃NH₃PbI_{3-x}Cl_x Perovskite” Materials 9 (2016) 123; doi: <https://doi.org/10.3390/ma9030123>
- [5.22] K. Stowe, (2007) “An Introduction to Thermodynamics and Statistical Mechanics 2nd Ed.” Cambridge University Press, The Edinburgh Building, Cambridge CB2 8RU, UK
- [5.23] J. T .Y. Lee, K. L. Chow, K. Wang and W. H. Tsang, “Is Macroporosity Absolutely Required for Preliminary in Vitro Bone Biomaterial Study? A Comparison between Porous Materials and Flat Materials” J. Funct. Biomater. 2 (2011) 308 – 337; doi: <https://doi.org/10.3390/jfb2040308>
- [5.24] N. Yantara, F. Yanan, C. Shi, H. A. Dewi, P. P. Boix, S. G. Mhaisalkar and N. Mathews, “Unravelling the Effects of Cl Addition in Single Step CH₃NH₃PbI₃ Perovskite Solar Cells” Chem. Mater. 27 (2015) 2309 – 2314; doi: <https://doi.org/10.1021/cm502710r>

UNIVERSITY of the
WESTERN CAPE

CHAPTER SIX

Summary and Future Work

Synthesis of ZnO nanowires was successfully completed using the autoclave hydrothermal and non-pressurised chemical bath method. With the results provided it is evident that non-pressurised chemical bath method incorporated with PEI yielded more aligned and straight nanowires in the c-axis. The challenge with hydrothermal is the curing temperature. After a reaction the teflon liner and the solution took time to reach room temperature, which affected the reaction time and the morphology of the nanowires. The best results were obtained at a bath temperature of 90 °C, zinc acetate, hexamethylenetetramine and polyethylenimine concentration of 70 mM for 3hrs. The optical and structural properties were investigated by using SEM, TEM, XRD and UV-Vis spectroscopy. The transmission of ZnO nanowires was found above 80% in the visible to IR region, which is almost close to glass/AZO transmission of above 85%. XPS survey scan yielded Zn:O ratio of 1.55:1. It is shown that ZnO is a promising alternative to TiO₂ because of its excellent properties and its affordability.

The mixed-halide MAPbI_{3-x}Cl_x perovskite films were deposited under different spin-coating parameters to find the optimum conditions. Better coverage of the perovskite was obtained at 120 °C at an annealing time of 3hours, spin-coated at 2000 rpm for 60 seconds. The relative composition of MAPbI_{1.96}Cl_{1.04} with x =1.04. The excessive chlorine concentration was due to unreacted PbCl₂. This proved that the perovskite ink was not fully converted. The film crystallinity was studied with XRD. MAPbI_{3-x}Cl_x peaks were observed along with chlorine rich MAPbCl₃ and unreacted MAI and PbCl₂ peaks. While significant progress has been achieved in utilising ZnO as electron-selective contacts in perovskite solar cells (PSCs), the challenge of perovskite instability on ZnO remains a significant barrier to their real-world implementation.

Consequently, a thorough and essential comprehension of lead halide perovskite materials and their device structures are crucial for effectively utilising ZnO as electron transport layers in PSCs.

As such, more experimental work needs to be done to improve the perovskite coverage on ZnO nanowires, with future experiments including heating of the perovskite ink before being deposited on the AZO substrate. Additional research must also include testing of the perovskite/ZnO nanowires structures in an actual solar cell.

